

Constraining the Galaxy-Halo Connection Over The Last 13.3 Gyrs: Star Formation Histories, Galaxy Mergers and Structural Properties

Aldo Rodríguez-Puebla^{1,2*}, Joel R. Primack³, Vladimir Avila-Reese²,
and S. M. Faber⁴

¹ *Department of Astronomy & Astrophysics, University of California at Santa Cruz, Santa Cruz, CA 95064, USA*

² *Instituto de Astronomía, Universidad Nacional Autónoma de México, A. P. 70-264, 04510, México, D.F., México*

³ *Physics Department, University of California, Santa Cruz, CA 95064, USA*

⁴ *UCO/Lick Observatory, Department of Astronomy and Astrophysics, University of California, Santa Cruz, CA 95064, USA*

Released 20?? Xxxxx XX

ABSTRACT

We present new determinations of the stellar-to-halo mass relation (SHMR) at $z = 0 - 10$ that match the evolution of the galaxy stellar mass function, the SFR – M_* relation, and the cosmic star formation rate. We utilize a compilation of 40 observational studies from the literature and correct them for potential biases. Using our robust determinations of halo mass assembly and the SHMR, we infer star formation histories, merger rates, and structural properties for average galaxies, combining star-forming and quenched galaxies. Our main findings: (1) The halo mass M_{50} above which 50% of galaxies are quenched coincides with $\text{sSFR}/\text{sMAR} \sim 1$, where sMAR is the specific halo mass accretion rate. (2) M_{50} increases with redshift, presumably due to cold streams being more efficient at high redshift while virial shocks and AGN feedback become more relevant at lower redshifts. (3) The ratio sSFR/sMAR has a peak value, which occurs around $M_{\text{vir}} \sim 2 \times 10^{11} M_{\odot}$. (4) The stellar mass density within 1 kpc, Σ_1 , is a good indicator of the galactic global sSFR. (5) Galaxies are statistically quenched after they reach a maximum in Σ_1 , consistent with theoretical expectations of the gas compaction model; this maximum depends on redshift. (6) In-situ star formation is responsible for most galactic stellar mass growth, especially for lower-mass galaxies. (7) Galaxies grow inside out. The marked change in the slope of the size–mass relation when galaxies became quenched, from $d \log R_{\text{eff}}/d \log M_* \sim 0.35$ to ~ 2.5 , could be the result of dry minor mergers.

Key words: galaxies: evolution - galaxies: haloes - galaxies: luminosity function - galaxies: mass function - galaxies: star formation - cosmology: theory

1 INTRODUCTION

There has been remarkable recent progress in assembling large galaxy samples from multiwavelength sky surveys. Moreover, these advances are not just for observations of local galaxies but also for very distant galaxies, resulting in reliable samples which contain hundreds of thousands of galaxies at $z \sim 0.1$, tens of thousands between $z \sim 0.2 - 4$, hundreds of galaxies between $z \sim 6 - 8$ and a few tens of galaxies confirmed as distant as $z \sim 9 - 10$.¹ Thus, statistical

analyses of the properties of the galaxies are now possible with unprecedented detail including robust determinations of the luminosity functions (LF) over a very wide redshift range.

In parallel, substantial progress has been made on stellar population synthesis (SPS) modelling (for a recent review, see Conroy 2013), allowing the determination of physical parameters that are key to studying galaxy evolution, including galaxy stellar masses and star formation rates (SFRs).² Thus, we are in an era in which robust determi-

* rodriguez.puebla@gmail.com

¹ These achievements are all the more impressive when one realizes that the Universe was only ~ 500 Myrs old at $z = 10$.

² Also empirically motivated diagnostics of galaxy SFR have been improved in the last few years; for a recent review, see Kennicutt & Evans (2012).

nations of the galaxy stellar mass function (GSMF) and the correlation between stellar mass and SFRs can now be robustly explored.

It is important to have accurate and robust determinations of the GSMFs and SFRs because there is a fundamental link between them. While the GSMF is a time-integrated quantity (reflecting stellar mass growth by in-situ star formation and/or galaxy mergers, and also the mechanisms that have suppressed the formation of stars especially in massive galaxies), the SFR is an instantaneous quantity that measures the in-situ transformation of gas into stars, typically measured over times scales of $\sim 10 - 100$ Myrs. In other words, except for mergers, the galaxy SFRs are proportional to the time derivative of the GSMFs. Indeed, previous studies have combined these two statistical properties to explore the stellar mass growth of galaxies (e.g., Bell et al. 2007; Drory & Alvarez 2008; Peng et al. 2010; Papovich et al. 2011; Leja et al. 2015) and to understand the most relevant mechanisms that shape their present-day properties.

At the same time, one of the key open questions in modern astronomy is how galaxy properties relate to those of their host dark matter halos and subhalos. Since galaxies formed and evolved within dark matter halos, one expects that the masses and assembly histories of dark matter halos are linked to the stellar mass and SFRs of their host galaxies (for recent reviews see Mo, van den Bosch & White 2010; Somerville & Davé 2015). Indeed, a substantial effort has focused on establishing robust determinations of the galaxy-halo connection, commonly reported in the form of the stellar-to-halo mass relation, SHMR (Behroozi, Conroy & Wechsler 2010; Moster et al. 2010; Yang et al. 2012; Behroozi, Wechsler & Conroy 2013b; Moster, Naab & White 2013, and references therein). The galaxy-halo connection can be obtained by using three different methods, two of which are physically motivated, based on hydrodynamical simulations and semi-analytic models of galaxy formation (both discussed in Somerville & Davé 2015, and references therein). The third method, which we follow in this paper, relies on semi-empirical modelling of the galaxy-halo connection (see e.g. Mo, van den Bosch & White 2010). That is, we use abundance matching to relate galaxies to their host halos, assuming that the average galactic stellar mass growth follows the average halo mass accretion. Thus we infer the most likely trajectories of the galaxy progenitors as a function of mass and redshift. However, since we model average growth histories rather than the growth histories of individual galaxies (as is done in semi-analytic models or in hydrodynamic simulations), we do not know “case by case” how galaxies evolved.

We use a compilation of data from the literature on galaxy stellar mass functions and star-formation rates, recalibrated to consistent assumptions regarding the initial mass function, photometry, cosmology, etc. (see Tables 1 and 2). We fit all this data accurately using a galaxy model that consists of eighteen adjustable parameters, fifteen to model the redshift evolution of the SHMR and three to model the fraction of stellar mass growth due to in-situ star formation. Our approach also allows us to model average galaxy radial profiles including surface densities at 1kpc and at the effective radius.

1.1 Semi-empirical modelling

The idea behind semi-empirical modelling of the galaxy-halo connection is to use simple rules to populate dark matter halos and subhalos with mock galaxies that match the observed distribution of galaxy surveys. There are three main approaches to doing this. One of them is subhalo abundance matching, SHAM, which matches the cumulative GSMF to the cumulative halo mass function in order to obtain a correlation between galaxy stellar mass and (sub)halo mass (Kravtsov et al. 2004; Vale & Ostriker 2004; Conroy, Wechsler & Kravtsov 2006; Shankar et al. 2006; Behroozi, Conroy & Wechsler 2010; Moster et al. 2010; Guo et al. 2010; Rodríguez-Puebla, Drory & Avila-Reese 2012; Papastergis et al. 2012; Hearin et al. 2013b). The next two are the halo occupation distribution (HOD) model (Jing, Mo & Börner 1998; Seljak 2000; Scoccimarro et al. 2001; Berlind & Weinberg 2002; Cooray & Sheth 2002; Kravtsov et al. 2004; Zehavi et al. 2005; Zheng et al. 2005; Leauthaud et al. 2011; Rodríguez-Puebla, Avila-Reese & Drory 2013; Tinker et al. 2013; Contreras et al. 2017) and the closely related conditional stellar mass function model (Yang, Mo & van den Bosch 2003; Cooray 2006; Yang et al. 2012; Rodríguez-Puebla et al. 2015). Both approaches constrain the distribution of central and satellite galaxies by using the observed two-point correlation function, 2PCF, and/or galaxy group catalogs and galaxy number densities. In this paper we focus on the first approach, SHAM, described in detail in Section 2.

Semi-empirical modelling of the galaxy-halo connection has received much attention recently, in part because of its simplicity but also because of its power in projecting different observables in terms of the theoretical properties of the halos (for some applications of these ideas see, e.g., Shankar et al. 2006; Conroy & Wechsler 2009; Firmani & Avila-Reese 2010; Yang et al. 2013; Behroozi, Wechsler & Conroy 2013b; Rodríguez-Puebla, Avila-Reese & Drory 2013; Hearin et al. 2013a; Masaki, Lin & Yoshida 2013; Rodríguez-Puebla et al. 2015; Li et al. 2016; Micic, Martinović & Sinha 2016; Huang et al. 2017; Matthee et al. 2017). Moreover, improvements in building more accurate and consistent halo finders for determining halo properties and their progenitors from large N -body cosmological simulations (e.g., Behroozi et al. 2013, and references therein) not only make possible a more accurate modelling of the galaxy-halo connection but also allow consistent connections of observables from different redshifts. This is especially true when information on the evolution of the GSMF and the SFRs is available. Here, we will present a framework that follows the median evolution of halo masses linked to the corresponding stellar masses.

The importance of the galaxy-halo connection, however, not only relies on determining accurate models that match observations, i.e., having robust determinations of the stellar-to-halo mass relation (SHMR), but also on using it as a phenomenological tool to understand the average growth of galaxies by projecting several galaxy observables related to galaxy evolution. This does not imply that semi-empirical modelling of the galaxy-halo connection should replace more physically motivated studies such as those mentioned previously, but rather that a synergy between all these approaches is ideal to have a more complete and accurate picture of galaxy formation and evolution.

We would like to emphasize that the approach employed here presents a probabilistic description of galaxy evolution driven exclusively as a function of mass. That is, the galaxy assembly histories, which we also call trajectories, that we will study in this paper refer to *average* histories. From this point of view, at least, we argue that the results that will be presented on this paper are the typical assembly histories of galaxies as a function of their stellar or virial masses.

In this paper we are interested in constraining the galaxy-halo connection and in extending this connection to predictions of the evolution of individual (average) galaxies as a function of mass. Besides, for the first time, here we introduce the evolution of galaxy *radial* structural properties within this framework. There is evidence showing a tight correlation between the structural evolution of galaxies and their SFRs. For example, Kauffmann et al. (2003a) showed that above a critical effective stellar surface mass density galaxies typically are old and quenched. Similar conclusions have been found when using other surface mass density definitions (Cheung et al. 2012; Fang et al. 2013; Barro et al. 2013, 2015; Tacchella et al. 2015) or Sérsic index (see e.g. Bell et al. 2012). Nevertheless, it is not clear whether the galaxy structural transformation is the key driver of quenching, since it is also expected that dark matter halos may make SFRs less efficient above $M_{\text{vir}} \sim 10^{12} M_{\odot}$ (e.g., Dekel & Birnboim 2006). Using our framework, we are in a good position to investigate how all these quantities relate to each other.

In short, the present paper formulates a semi-empirical approach based on three key assumptions: (1) every halo hosts a galaxy; (2) the in-situ/ex-situ stellar mass growth of galaxies is associated to the mass growth of halos by accretion/mergers; (3) the average radial stellar mass distribution of galaxies at a given M_* is composed of a Sérsic disc and a de Vacouleurs spheroid, where the fractions of these components are associated with the fractions of star-forming and quenched galaxies at this mass. Under these assumptions and once the SHMRs at different redshifts are constrained from observations, the growth of dark matter halos can be used to determine the stellar in-situ and ex-situ (merger) mass growth of the associated galaxies, and thus their star formation histories. In addition, the observed galaxy size-mass relation at different redshifts can be used to project the size evolution of the disc and spheroid components of galaxies, and probe a possible relation between their structural and star formation histories.

Our model, under the assumptions mentioned above, provide a consistent picture of stellar and halo mass, SFR, merger rate, and structural evolution of galaxies as a function of mass across ~ 13.3 Gyrs of the cosmic time in the context of the Λ CDM cosmology. These results are ideal for constraining semi-analytic models and numerical simulations of galaxy formation and evolution, not only at the present day but at high redshifts. On the other hand, our model of galaxy mass assembly and SFR history based on halo mass accretion trajectories can be used to compare with those from other empirical approaches and in this way identify possible biases in various approaches. For example, by means of the “fossil record” method, the global and radial stellar mass assembly histories of galaxies of different masses have recently been inferred from spectroscopic surveys of local galaxies under the assumption of no radial displace-

ments of stars (Pérez et al. 2013; Ibarra-Medel et al. 2016). The structural and mass assembling histories of galaxies have also been partially inferred from direct empirical approaches, for instance, from observations of galaxy populations of similar masses and comoving number densities at different redshifts (e.g., van Dokkum et al. 2010, 2013; Leja et al. 2015).

This paper is organized as follows. In Section 2, we describe our galaxy-halo-connection model. In Section 3, we present the model ingredients, namely, the parametric redshift dependence of the SHMR and the fraction of in-situ and ex-situ stellar mass growth. In Section 4, we present the observations that we utilize to constrain the galaxy-halo connection. Here we describe in detail the potential systematic effects that could affect our derivations, and how we correct for them. In Section 5, we present our best fitting model. In Section 6.1 we discuss our resulting SHMR and compare to previous determinations from the literature. Section 6.2 describes the star formation histories and halo star formation efficiencies for the progenitors of today’s galaxies. Results from galaxy mergers are presented in Section 6.3. In Section 7 we discuss the implications of the structural evolution of galaxies. Finally, in Section 8 we discuss all the results presented in previous sections and in Section 9 we summarize and list our main conclusions.

In this paper we adopt cosmological parameter values from the Planck mission: $\Omega_{\Lambda} = 0.693$, $\Omega_{\text{M}} = 0.307$, $\Omega_{\text{B}} = 0.048$, $h = 0.678$. These are the same parameters used in the Bolshoi-Planck cosmological simulation (Rodríguez-Puebla et al. 2016a), which we use to determine dark matter halo properties and evolution (see the Appendices for details).

2 THEORETICAL FRAMEWORK

2.1 Galaxy-Halo Connection

Subhalo abundance matching, SHAM, is a simple and yet powerful statistical approach for connecting galaxies to halos. In its simplest form, given some halo property (usually halo mass or maximum circular velocity) the halo number density and the galaxy number density are matched in order to obtain the connection between halos and the galaxies that they host. As a result one obtains a unique relation between galaxy stellar mass and a halo property. In fact, it is expected that this relation has some scatter since the properties of the galaxies might be partly determined by different halo properties and/or some environmental factors. For example, in the case of halo mass, analysis of large galaxy group catalogs (Yang, Mo & van den Bosch 2009a; Reddick et al. 2013), the kinematics of satellite galaxies (More et al. 2011), as well as galaxy clustering (Shankar et al. 2014; Rodríguez-Puebla et al. 2015; Tinker et al. 2016) have found that this dispersion is of the order of $\sigma_{\text{h}} \sim 0.15$ dex. To take this into account, abundance matching should be slightly modified to include a physical scatter around the galaxy stellar-to-halo mass relation, hereafter SHMR.

Formally, if we assume that halo mass M_{halo} is the halo property that correlates best with stellar mass, we can model the GSMF of galaxies by defining $\mathcal{H}(M_*|M_{\text{halo}})$ as the probability distribution function that a halo of mass M_{halo} hosts a galaxy of stellar mass M_* . Then the *intrinsic* GSMF, ϕ_{g1} , as a function of stellar mass is given by

$$\phi_{g_1}(M_*) = \int \mathcal{H}(M_*|M_{\text{halo}})\phi_{\text{halo}}(M_{\text{halo}})d\log M_{\text{halo}}, \quad (1)$$

where ϕ_{halo} denotes the total number density of halos and subhalos within the mass range $\log M_{\text{halo}} \pm d\log M_{\text{halo}}/2$.³ Note that in the above equation the units for ϕ_{g_1} and ϕ_{halo} are in $\text{Mpc}^{-3}\text{dex}^{-1}$. Here M_{halo} is interpreted as the virial mass, M_{vir} , for distinct halos and M_{peak} , the peak value of virial mass at or before accretion, for subhalos, thus:

$$M_{\text{halo}} = \begin{cases} M_{\text{vir}} & \text{Distinct halos} \\ M_{\text{peak}} & \text{Subhalos} \end{cases} \quad (2)$$

and

$$\phi_{\text{halo}}(M_{\text{halo}}) = \phi_{\text{vir}}(M_{\text{vir}}) + \phi_{\text{sub}}(M_{\text{peak}}). \quad (3)$$

Subhalos can lose a significant fraction of their mass due to tidal stripping. Since tidal stripping affects the subhalo more than the stars of the galaxy deep inside it, this implies that the stellar mass of a satellite galaxy does not correlate in a simple way with its subhalo mass. Therefore, in connecting galaxies to dark matter (sub)halos, as in SHAM, it has been shown that the mass that the halo had when it was still in a distinct halo correlates better with the stellar mass of the satellite galaxy it hosts. This comes from the fact that the observed two-point correlation function is approximately reproduced when assuming identical stellar-to-halo mass relations for central and satellite galaxies until the satellites are accreted. In this paper we use the mass M_{peak} defined as the maximum mass reached along the main progenitor assembly mass. Indeed, Reddick et al. (2013) found that this is the quantity that correlates best with galaxy stellar mass and luminosity by reproducing most accurately the observed galaxy clustering (see also Moster et al. 2010).

We assume that the probability distribution function $\mathcal{H}(M_*|M_{\text{halo}})$ is a log-normal distribution with a scatter $\sigma_{\text{h}} = 0.15$ dex (Rodríguez-Puebla et al. 2015)⁴ independent of M_{halo} :

$$\mathcal{H}(M_*|M_{\text{halo}}) = \frac{1}{\sqrt{2\pi\sigma_{\text{h}}^2}} \times \exp\left[-\frac{(\log M_* - \langle \log \mathcal{M}_*(M_{\text{halo}}) \rangle)^2}{2\sigma_{\text{h}}^2}\right], \quad (4)$$

where the mean SHMR is denoted by $\langle \log \mathcal{M}_*(M_{\text{halo}}) \rangle$. In the absence of scatter around the mean SHMR, Equation (1) reduces to

$$\phi_{g_1}(M_*) = \phi_{\text{halo}}(M_{\text{halo}}) \frac{d\log M_{\text{halo}}}{d\log M_*}. \quad (5)$$

The above equation is just simply the traditional SHAM.

Individual galaxy stellar mass estimates are also subject to random errors (Conroy 2013). Indeed, the GSMF that is inferred from observations through the estimation of individual stellar masses of galaxies (we will denote this as $\phi_{g_{\text{obs}}}$) is the result of the random errors over the intrinsic

GSMF (Behroozi, Conroy & Wechsler 2010). Formally, we can represent the observed $\phi_{g_{\text{obs}}}$ as the convolution of ϕ_{g_1} :

$$\phi_{g_{\text{obs}}}(M_*) = \int \mathcal{G}(\log M_*/x)\phi_{g_1}(x)d\log x, \quad (6)$$

where we again assume that random errors follow a log-normal distribution

$$\mathcal{G}(\log \frac{M_*}{x}) = \frac{1}{\sqrt{2\pi\sigma_*^2}} \exp\left[-\frac{1}{2\sigma_*^2} \log^2\left(\frac{M_*}{x}\right)\right]. \quad (7)$$

Here σ_* will encode all the uncertainties affecting the GSMF. We use a slightly modified version for σ_* as a function of redshift from Behroozi, Conroy & Wechsler (2010), given by

$$\sigma_* = 0.1 + 0.05z, \quad (8)$$

which is more consistent with what is observed in new determinations of M_* at $z \sim 0.1$ (e.g., Mendel et al. 2014).

Finally, when combining Equations (1) and (6) the relation between the observed GSMF, $\phi_{g_{\text{obs}}}$, and the mass function of dark matter halos ϕ_{halo} is given by

$$\phi_{g_{\text{obs}}}(M_*) = \int P(M_*|M_{\text{halo}})\phi_{\text{halo}}(M_{\text{halo}})d\log M_{\text{halo}}, \quad (9)$$

where P is again assumed to be a log-normal distribution with a scatter σ_{T} independent of M_{halo}

$$P(M_*|M_{\text{halo}}) = \frac{1}{\sqrt{2\pi\sigma_{\text{T}}^2}} \times \exp\left[-\frac{(\log M_* - \langle \log \mathcal{M}_*(M_{\text{halo}}) \rangle)^2}{2\sigma_{\text{T}}^2}\right], \quad (10)$$

and $\sigma_{\text{T}}^2 = \sigma_{\text{h}}^2 + \sigma_*^2$.

2.2 Star Formation Histories

Once we have established the galaxy-halo connection, we can use the growth of dark matter halos, as measured from high resolution N -body cosmological simulations, to predict the M_* of the galaxy that they host as a function of z , and thus the corresponding galaxy star formation histories.

Imagine that we want to derive the amount of stars that the galaxies produce between the redshifts $z + \Delta z$ and z . Now, let us assume that we know the trajectories for the main progenitors of halos at z_0

$$M_{\text{vir}}(z|z_0) = M_{\text{vir}}(z|M_{\text{vir},0}, z_0), \quad (11)$$

where $M_{\text{vir},0}$ is the final mass of the halo at the redshift of observation z_0 . According to Equation (11), this implies that the mass of the progenitor at $z + \Delta z$ is $M_{\text{vir}}(z + \Delta z|M_{\text{vir},0}, z_0)$ while at z it is $M_{\text{vir}}(z|M_{\text{vir},0}, z_0)$. Using the redshift evolution of the SHMR described above we can thus infer the amount of stellar mass the galaxy will grow between $z + \Delta z$ and z :

$$\Delta M_*(z|M_{\text{vir},0}, z_0) = M_* [M_{\text{vir}}(z|M_{\text{vir},0}, z_0), z] - M_* [M_{\text{vir}}(z + \Delta z|M_{\text{vir},0}, z_0), z + \Delta z].$$

Galaxies build their masses via in-situ star formation and/or through ex-situ process such as galaxy mergers. Following Behroozi, Wechsler & Conroy (2013b), we apply corrections for mergers by assuming that ΔM_* can be separated by the amount of mass that galaxies grow by mergers and

³ Note that observations of the GSMF are made over redshift slices. In order to be consistent with observations, we average ϕ_{halo} over the observed volumes. For simplicity we do not show this explicitly in the remainder of this paper.

⁴ Note that Tinker et al. (2016) concluded that the upper limit to the intrinsic scatter is 0.16 dex based on galaxy clustering of massive galaxies. This is consistent with the value assumed above.

the amount of mass built up by in-situ star formation during the timescale $\Delta t = t(z) - t(z + \Delta z)$:

$$\Delta M_*(z|M_{\text{vir},0}, z_0) = \Delta M_{\text{merger}}(z|M_{\text{vir},0}, z_0) + \Delta M_{\text{SFR}}(z|M_{\text{vir},0}, z_0),$$

or equivalently

$$\frac{\Delta M_{\text{SFR}}}{\Delta t} = \frac{\Delta M_*}{\Delta t} f_{\text{in situ}}, \quad (12)$$

where we have omitted the terms in the parentheses for simplicity and we have defined

$$f_{\text{in situ}} = 1 - f_{\text{ex situ}} = 1 - \frac{\Delta M_{\text{merger}}}{\Delta M_*}. \quad (13)$$

Here, $f_{\text{ex situ}}$ is the fraction of mass acquired through galaxy mergers. The fraction $f_{\text{in situ}}$ is a function that depends on M_{vir} and z . The parametrization that we will use for $f_{\text{in situ}}$ will be described in Section 3.3. Finally, we calculate the SFR, taking into account gas recycling, as:

$$\text{SFR}(z|M_{\text{vir},0}, z_0) = \frac{f_{\text{in situ}}}{1-R} \left[\frac{\Delta M_*(z|M_{\text{vir},0}, z_0)}{t(z) - t(z + \Delta z)} \right]. \quad (14)$$

Here R is the fraction of mass that is returned as gaseous material into the interstellar medium, ISM, from stellar winds and short lived stars. In other words, $1 - R$ is the fraction of the change in stellar mass that is kept as long-lived. In this paper we make the instantaneous recycling approximation, we use the fitting form for $R(t)$ given in Behroozi et al. (2013, section 2.3), and we assume for simplicity that t in $R(t)$ is the cosmic time since the big bang.

The timescale $\Delta t = t(z) - t(z + \Delta z)$ is a free parameter in our model. Star formation indicators are sensitive to probe different time scales. The most common estimators based on UV and IR probe star formation rates on timescales around ~ 100 Myr, while $\text{H}\alpha$ probes the SFR for times less than about 10 Myr (Kennicutt & Evans 2012). In this paper we will use observations homogenized to timescales of 100 Myrs as described in Speagle et al. (2014) and we compute SFRs averaged over a timescale of 100 Myr. That is to say, we fixed $\Delta t = 100$ Myrs in Equation (12).

Before describing our modelling of the observed distribution of galaxy SFRs, it is worth mentioning that Equation (14) is only valid for central galaxies. To account for the evolution of satellite galaxies, we will assume, for simplicity, that they evolve as central galaxies, i.e.,

$$\text{SFR}(z|M_{\text{DM},0}, z_0) = \text{SFR}_{\text{cen}}(z|M_{\text{vir},0}, z_0) = \text{SFR}_{\text{sat}}(z|M_{\text{peak},0}, z_0). \quad (15)$$

The impact of satellite galaxies has been discussed in detail in previous studies (see e.g., Yang, Mo & van den Bosch 2009b; Neistein et al. 2011; Rodríguez-Puebla, Drory & Avila-Reese 2012; Yang et al. 2012; Wetzel, Tinker & Conroy 2012; Zavala et al. 2012; Rodríguez-Puebla, Avila-Reese & Drory 2013). These studies have shown that assuming similar relations for centrals and satellites could lead to potential inconsistencies. This problem has been already faced in previous works (e.g., Yang et al. 2012; Zavala et al. 2012) by modelling the evolution of satellite galaxies after infall. On the other hand, Rodríguez-Puebla, Drory & Avila-Reese (2012) argued that it is still possible to develop a self-consistent model in the light of SHAM by relaxing the assumption that the SHMR of central and satellite galaxies are identical. In that paper, it was shown that assuming

identical SHMR of central and satellite galaxies could lead to underestimate of the spatial clustering of galaxies from SHAM, see also Guo et al. (2016) for similar conclusions. A more detailed modelling of central and satellite galaxies separately would be required to introduce more observational constraints such as the two point correlation function and/or galaxy groups, which is beyond the scope of this paper (see e.g. Rodríguez-Puebla, Avila-Reese & Drory (2013) for details⁵).

2.3 The Distribution of Star Formation Rates

In the previous subsection we described the theoretical framework to derive the star formation histories in halos of different masses. In this subsection we describe how to compare the above star formation histories to the observed SFRs from the galaxy population.

Suppose that we want to measure the mean SFRs for a volume-complete sample of galaxies with M_* at some redshift z . Then, the *intrinsic* probability distribution of having galaxies with SFRs in the range $\log \text{SFR} \pm d \log \text{SFR}/2$ is given by

$$\mathcal{S}_{*,I}(\text{SFR}|M_*, z) = \int \mathcal{S}_{\text{h},I}(\text{SFR}|M_{\text{halo}}, z) \times \mathcal{H}(M_{\text{halo}}|M_*) d \log M_{\text{halo}}, \quad (16)$$

with $\mathcal{S}_{\text{h},I}(\text{SFR}|M_*, z)$ as the *intrinsic* probability distribution of SFR in the range $\log \text{SFR} \pm d \log \text{SFR}/2$ in (sub)halos of mass M_{halo} . Note that $\mathcal{H}(M_{\text{halo}}|M_*)$ is not the same function as $\mathcal{H}(M_*|M_{\text{halo}})$, but the functions are related to each other through Bayes' theorem. Similarly to stellar mass, derivation of the SFRs is also subject to random errors. Moreover, one expects that the observed distribution of SFRs $\mathcal{S}_{*,\text{obs}}$, for a given stellar mass, includes random errors affecting the intrinsic distribution $\mathcal{S}_{*,I}$. In other words, the observed distribution $\mathcal{S}_{*,\text{obs}}$ is the convolution of the distribution of random errors, denoted by \mathcal{F} , with the intrinsic distribution $\mathcal{S}_{*,I}$: $\mathcal{S}_{*,\text{obs}} = \mathcal{F} \circ \mathcal{S}_{*,I}$, with the symbol \circ denoting the convolution operator. Note, however, that under the assumption that random errors have a lognormal distribution with 1σ statistical fluctuation, in either directions and independent on both halo and stellar mass, their effect will only increase the dispersion over the relationship SFR– M_* while the mean $\langle \log \text{SFR} \rangle$ is the same. As we will show later in this subsection, our framework does not require any other moment over the distribution $\mathcal{S}_{*,I}$ (and therefore over $\mathcal{S}_{*,\text{obs}}$) than its mean.

For local galaxies, $z \sim 0.1$, the distribution $\mathcal{S}_{*,\text{obs}}$, and consequently $\mathcal{S}_{*,I}$, is composed, at a very good approximation, of two lognormal distributions. One mode is dominated by star-forming galaxies (often referred as the galaxy star-formation main sequence) while the second mode is dominated by quiescent galaxies (e.g., Salim et al. 2007). This bimodality has also been observed to high redshifts (e.g.,

⁵ Rodríguez-Puebla, Drory & Avila-Reese (2012) and Rodríguez-Puebla, Avila-Reese & Drory (2013) found that the SHMR of central and satellite galaxies are different, an effect that can be explained due to environment effects. This would imply, that the SFRs of centrals will be on average higher than those of satellite galaxies, specially at low redshifts.

Noeske et al. 2007b; Karim et al. 2011). In this paper, however, we are more interested in the mean of the above distribution $\langle \log \text{SFR}(M_*, z) \rangle$ rather than in the full distribution.

Applying Bayes' theorem to $\mathcal{H}(M_{\text{halo}}|M_*)$ and substituting this in Equation (16) we get

$$\mathcal{S}_{*,\text{I}}(\text{SFR}|M_*, z) = \frac{1}{\phi_{g_{\text{I}}}(M_*, z)} \int \mathcal{S}_{\text{h}}(\text{SFR}|M_{\text{halo}}, z) \times \mathcal{H}(M_*|M_{\text{halo}}, z) \times \phi_{\text{halo}}(M_{\text{halo}}, z) d \log M_{\text{halo}}, \quad (17)$$

where $\phi_{g_{\text{I}}}(M_*, z)$ is given by Equation (1). By noting that

$$\langle \log \text{SFR}(M_{\text{halo}}, z) \rangle = \int \mathcal{S}_{\text{h}}(\text{SFR}|M_{\text{halo}}, z) \log \text{SFR} d \log \text{SFR},$$

and using the definition

$$\langle \log \text{SFR}(M_*, z) \rangle = \int \mathcal{S}_{*,\text{I}}(\text{SFR}|M_*, z) \log \text{SFR} d \log \text{SFR}, \quad (18)$$

we can conclude that

$$\langle \log \text{SFR}(M_*, z) \rangle = \phi_{g_{\text{I}}}^{-1}(M_*, z) \int \langle \log \text{SFR}(M_{\text{halo}}, z) \rangle \times \mathcal{H}(M_*|M_{\text{halo}}, z) \times \phi_{\text{halo}}(M_{\text{halo}}, z) d \log M_{\text{halo}}. \quad (19)$$

We use the above equation to derive SFRs in our model and compare to observations. Note that this equation does not require any other moment than the mean of the distribution $\mathcal{S}_{*,\text{I}}(\text{SFR}|M_*, z)$. The same argument applies when using $\mathcal{S}_{*,\text{obs}}(\text{SFR}|M_*, z)$ instead.

2.4 The Cosmic Star Formation Rate

In this subsection we describe how the Cosmic Star Formation Rate (CSFR) is calculated in the framework described above. Formally, the CSFR is given by

$$\dot{\rho}_{\text{obs}}(z) = \int \text{SFR} \times \phi_{\text{SFR,obs}}(\text{SFR}, z) \times d \log \text{SFR}, \quad (20)$$

with $\phi_{\text{SFR,obs}}(\text{SFR})$ as the *observed* comoving number density of galaxies with observed SFRs between $\log \text{SFR} \pm d \log \text{SFR}/2$.

In order to derive a model for the CSFR, we begin by noting that the relation between the SFRs, denoted by $\phi_{\text{SFR,obs}}$, and the observed GSMF is given by

$$\phi_{\text{SFR,obs}}(\text{SFR}) = \int \mathcal{S}_{*,\text{obs}}(\text{SFR}|M_*) \phi_{g_{\text{obs}}}(M_*) d \log M_*,$$

where we omit the dependence on z for simplicity. The next step is to substitute Equation (17) to obtain:

$$\phi_{\text{SFR,obs}}(\text{SFR}) = \int \mathcal{S}_{\text{h,obs}}(\text{SFR}|M_{\text{halo}}) \Theta(M_{\text{halo}}) \phi_{\text{halo}}(M_{\text{halo}}) d \log M_{\text{halo}},$$

with

$$\Theta(M_{\text{halo}}) = \int \frac{\phi_{g_{\text{obs}}}(M_*)}{\phi_{g_{\text{I}}}(M_*)} \times \mathcal{H}(M_*|M_{\text{halo}}) d \log M_*, \quad (21)$$

and we define $\mathcal{S}_{\text{h,obs}} = \mathcal{F} \circ \mathcal{S}_{\text{h,I}}$. Recall that the probability distribution function $\mathcal{S}_{\text{h,I}}$ and the function \mathcal{F} were described in Section 2.3. Before moving further into the description of our model, we briefly discuss the function $\Theta(M_{\text{halo}})$. Clearly, the function Θ depends strongly on the ratio $\phi_{g_{\text{obs}}}/\phi_{g_{\text{I}}}$, and in the case that $\phi_{g_{\text{obs}}}/\phi_{g_{\text{I}}} \sim 1$ then $\Theta \sim 1$. Actually, the effect of the ratio on the function Θ is expected to be small

for low-mass halos and larger at the high-mass end. This is because the effect of the convolution in Equation (6) depends on the logarithmic slope of $\phi_{g_{\text{I}}}$ (Cattaneo et al. 2008; Behroozi, Conroy & Wechsler 2010; Wetzel & White 2010). Figure A1 in Appendix A illustrates the redshift evolution of the function $\Theta(M_{\text{halo}})$ for our best fitting model (see Section 5 below). Note that at high redshifts this correction becomes very important and it should be taken into account in order to have a consistent model and a more accurate calculation of the CSFR.

When calculating the CSFR, the details behind the distribution function $\mathcal{S}_{\text{h,obs}}(\text{SFR}|M_{\text{halo}})$ are relevant. We assume that this distribution is lognormal with $\sigma_{\text{h,obs}} = 0.3$ dex and independent of mass. This assumption may sound crude as the observed distribution of SFRs, $\mathcal{S}_{*,\text{obs}}$, is actually bimodal, something that it is also expected for dark matter halos. Note, however, that in this paper we are more interested on the average evolution of galaxies rather than modelling different populations and therefore a lognormal distribution is an adequate approximation for our purposes. Once we have specified the shape of $\mathcal{S}_{\text{h,obs}}$ we can analytically calculate the following integral:

$$\langle \text{SFR}(M_{\text{halo}}) \rangle = \int \text{SFR} \times \mathcal{S}_{\text{h,obs}}(\text{SFR}|M_{\text{halo}}) \times d \log \text{SFR}, \quad (22)$$

which is given by

$$\log \langle \text{SFR}(M_{\text{halo}}) \rangle = \langle \log \text{SFR}(M_{\text{halo}}) \rangle + \frac{\sigma_{\text{h,obs}}^2}{2} \ln 10. \quad (23)$$

Finally, the CSFR can be calculated as:

$$\dot{\rho}_{\text{obs}}(z) = \int \langle \text{SFR}(M_{\text{halo}}) \rangle \Theta(M_{\text{halo}}) \phi_{\text{halo}}(M_{\text{halo}}) d \log M_{\text{halo}}, \quad (24)$$

which is the equation we utilize to calculate the CSFRs and that we will compare with observation. Note that the value of the scatter $\sigma_{\text{h,obs}}$ is relevant only for the calculation of the CSFR but not for the modelling of $\langle \log \text{SFR}(M_*) \rangle$, see Eq. (19).

Finally, Appendix A discusses the impact of assuming $\Theta(M_{\text{halo}}) = 1$ and that the probability distribution function $\mathcal{S}_{\text{h,obs}}$ is a Dirac- δ distribution function. In short, we find that the combined effect will result in an underestimation of the CSFR of around $\sim 30\%$ at low- z , but by an order of magnitude at high redshifts. Therefore, *taking into account all the above factors is critical when constraining our model*. We note that most previous authors have failed to recognize the above effects.

3 MODEL INGREDIENTS

Here we describe the model ingredients, namely, the parametric redshift dependence of the SHMR and the fraction of in-situ and ex-situ stellar mass growth.

3.1 Dark Matter Halos

In Appendix B, we present the theoretical ingredients to fully characterize the distribution of dark matter halos, namely, the halo and subhalo mass function and halo mass assembly. Briefly, we use the updated parameters from Rodríguez-Puebla et al. (2016a) from a set of high resolution N -body simulations for the Tinker et al. (2008) halo

mass function and the Behroozi, Wechsler & Conroy (2013b) fitting model to the subhalo population. We also use the fitting parameters from Rodríguez-Puebla et al. (2016a) for the median halo assembly histories from N -body simulations.

3.2 Parameterization of the SHMR

In order to describe the mean SHMR, we adopt the parametrization proposed in Behroozi, Wechsler & Conroy (2013b),

$$\langle \log \mathcal{M}_* \rangle = \log(\epsilon \times M_0) + g(x) - g(0), \quad (25)$$

where

$$g(x) = \delta \frac{(\log(1 + e^x))^\gamma}{1 + \exp(10^{-x})} - \log(10^{-\alpha x} + 1). \quad (26)$$

and $x = \log(M_{\text{vir}}/M_0)$. Previous studies have used simpler functions with fewer parameters (e.g., Yang, Mo & van den Bosch 2008; Moster, Naab & White 2013); however, as shown in Behroozi, Wechsler & Conroy (2013b), the function as given by Eq. (26) is necessary in order to map accurately the halo mass function into the observed GSMFs, which are more complex than a single Schechter function. Recall that at $z \sim 0.1$ we are using a mass function that is steeper at low masses after correcting for surface brightness incompleteness.

We assume that the above parameters change with redshift z as follows:

$$\log(\epsilon(z)) = \epsilon_0 + \mathcal{P}(\epsilon_1, \epsilon_2, z) \times \mathcal{Q}(z) + \mathcal{P}(\epsilon_3, 0, z), \quad (27)$$

$$\log(M_0(z)) = M_{0,0} + \mathcal{P}(M_{0,1}, M_{0,2}, z) \times \mathcal{Q}(z), \quad (28)$$

$$\alpha(z) = \alpha + \mathcal{P}(\alpha_1, \alpha_2, z) \times \mathcal{Q}(z), \quad (29)$$

$$\delta(z) = \delta_0 + \mathcal{P}(\delta_1, \delta_2, z) \times \mathcal{Q}(z), \quad (30)$$

$$\gamma(z) = \gamma_0 + \mathcal{P}(\gamma_1, 0, z) \times \mathcal{Q}(z). \quad (31)$$

Here, the functions $\mathcal{P}(x, y, z)$ and $\mathcal{Q}(z)$ are:

$$\mathcal{P}(x, y, z) = y \times z - \frac{x \times z}{1 + z}, \quad (32)$$

and

$$\mathcal{Q}(z) = e^{-4/(1+z)^2}. \quad (33)$$

Similar parameterizations were employed in Behroozi, Wechsler & Conroy (2013b).

3.3 Parameterization of the Fraction of In Situ Stellar Mass Growth

We assume that the function $f_{\text{in situ}}(M_{\text{vir}}, z)$, defined in Equation (13), which describes the fraction of mass assembled via in situ star formation in a period of 100 Myrs at redshift z , is given by:

$$f_{\text{in situ}}(z) = \frac{1}{1 + x^\beta(z)}, \quad (34)$$

with $x(z) = M_{\text{vir}}/M_{\text{in situ}}(z)$,

$$\log(M_{\text{in situ}}(z)) = M_{\text{in situ},0} + \mathcal{P}(M_{\text{in situ},1}, 0, z), \quad (35)$$

and

$$\beta(z) = \beta + \log(1 + z). \quad (36)$$

Recall that the complement to $f_{\text{in situ}}$ is $f_{\text{ex situ}}$, the fraction of mass acquired through galaxy mergers. At low redshifts, we expect that at low masses the function described by Equation (34) asymptotes to $f_{\text{in situ}}(z) \sim 1$ given that observations show that low-mass galaxies grow mostly by in-situ SFR, while at very large masses $f_{\text{in situ}}(z) < 1$ consistent with the fact that big elliptical galaxies build part of their mass by galaxy mergers.

4 OBSERVATIONAL INPUT: COMPILATION AND HOMOGENIZATION

This section describes the observational data that we utilize to constrain our semi-empirical model, namely, the GSMF, the SFRs and the CSFR. The main goal of this section is to present a compilation from the literature and to calibrate all the observations to the same basis in order to minimize potential systematical effects that can bias our conclusions.

In our compilation, we do not include observations from dusty submillimeter galaxies, which are the most extreme star formers in the Universe (for a recent review, see Casey, Narayanan & Cooray 2014). Submillimeter galaxies are galaxies that emit in the FIR and with high luminosities implying SFRs $\geq 300 M_\odot \text{yr}^{-1}$ at $z \sim 1 - 4$, that is, a factor of ~ 5 compared to normal star-forming galaxies (see e.g., Casey, Narayanan & Cooray 2014). This means that the population of submillimeter galaxies is a class of star formers that it is very particular and rare. We do not actually need to consider individual populations such as this one, given that we assume that the full population of galaxies is described by the probability distribution function of SFRs (Section 2.3) and thus submillimeter galaxies will automatically be included as the extreme values of the distribution.

4.1 The Galaxy Stellar Mass Function up to $z \sim 10$

In this Section, we use a compilation of various studies from the literature to characterize the redshift evolution of the GSMF from $z \sim 0.1$ to $z \sim 10$. Table 1 lists the references we utilize for this section. The reader interested in the details is referred to the original sources.

The various GSMFs used in this paper were obtained based on different observational campaigns and techniques. In order to directly compare the various published results of the GSMFs, and therefore to obtain a consistent evolution of the GSMF from $z \sim 0.1$ to $z \sim 10$, we apply some calibrations to observations. Among the most important, these calibrations include the initial mass function (IMF), Stellar Population Synthesis models (SPS), photometry corrections, cosmology, and variations between different search areas in surveys. Note, however, that in this paper we do not carry out an exhaustive analysis for these calibrations. Instead, we apply standard corrections according to the literature. Additionally, we derive the GSMF from $z = 4$ to $z = 10$ based on the observed evolution of UV luminosity functions and stellar mass-UV luminosity ratios. Next, we briefly describe the corrections that we include in our set of GSMFs.

Table 1. Observational data on the galaxy stellar mass function

Author	Redshift ^a	Ω [deg ²]	Corrections
Bell et al. (2003)	$z \sim 0.1$	462	I+SP+C
Yang, Mo & van den Bosch (2009a)	$z \sim 0.1$	4681	I+SP+C
Li & White (2009)	$z \sim 0.1$	6437	I+P+C
Bernardi et al. (2010)	$z \sim 0.1$	4681	I+SP+C
Baldry et al. (2012)	$0 < z < 0.06$	143	C
Bernardi et al. (2013)	$z \sim 0.1$	4681	I+SP+C
Rodríguez-Puebla et al. in prep	$z \sim 0.1$	7748	S
Drory et al. (2009)	$0 < z < 1$	1.73	SP+C
Moustakas et al. (2013)	$0 < z < 1$	9	SP+D+C
Pérez-González et al. (2008)	$0.2 < z < 2.5$	0.184	I+SP+D+C
Tomczak et al. (2014)	$0.2 < z < 3$	0.0878	C
Ilbert et al. (2013)	$0.2 < z < 4$	2	C
Muzzin et al. (2013)	$0.2 < z < 4$	1.62	I+C
Santini et al. (2012)	$0.6 < z < 4.5$	0.0319	I+C
Mortlock et al. (2011)	$1 < z < 3.5$	0.0125	I+C
Marchesini et al. (2009)	$1.3 < z < 4$	0.142	I+C
Stark et al. (2009)	$z \sim 6$	0.089	I
Lee et al. (2012)	$3 < z < 7$	0.089	I+SP+C
González et al. (2011)	$4 < z < 7$	0.0778	I+C
Duncan et al. (2014)	$4 < z < 7$	0.0778	C
Song et al. (2015)	$4 < z < 8$	0.0778	I
This paper, Appendix D	$4 < z < 10$	0.0778	–

Notes: ^aIndicates the redshifts used in this paper. I=IMF; P= photometry corrections; S=Surface Brightness correction; D=Dust model; NE= Nebular Emissions; SP = SPS Model; C = Cosmology.

4.1.1 Systematic Effects on the GSMF

One of the most important sources of calibration is the IMF since it determines the overall normalization of the stellar mass-to-light ratios. In this paper we will assume that the IMF is universal, i.e., it is independent of time, galaxy type, and environment. Note, however, that there is not a consensus on this, since there exist arguments in favour (e.g. Bastian, Covey & Meyer 2010) and against (e.g. Conroy et al. 2013) the universality of the IMF. For the case of a universal IMF, the choice of one or another IMF is a source of a systematic change in stellar mass, i.e., between two universal IMFs there is a constant offset. The most popular choices for the IMFs are Salpeter (1955), diet Salpeter, Chabrier (2003), and Kroupa (2001). For determining the redshift evolution of the GSMF, we correct observations to the IMF of Chabrier (2003). We apply the following offsets:

$$M_{C03} = M_{S55} - 0.25 = M_{DS} - 0.1 = M_{K01} - 0.05, \quad (37)$$

The subscripts refer to Salpeter (1955), diet Salpeter, and Kroupa (2001) respectively. Note that the above offsets are in dex with M referring to the log of the stellar mass derived using their corresponding IMF. We use Table 2 in Bernardi et al. (2010) for these corrections.

The second most important source of calibration is the choice of SPS model due to uncertain stellar evolutionary phases. The treatment of the thermally pulsating asymptotic horizontal branch stars (TP-AGB) has received, particularly, much attention in recent years. Including the TP-AGB can lower the stellar mass of a single stellar population by $\gtrsim 50\%$ for an age of ~ 1 Gyr (Chabrier IMF), but as the population gets older, the mass difference between the models that include or not the TP-AGB tends to disappear (Bruzual 2007). Nonetheless, the SF histories of galaxies are

much more complex than the one of a single stellar population. Muzzin et al. (2013, see also, Maraston 2005; Maraston et al. 2006; Muzzin et al. 2009; Marchesini et al. 2009) have compared the stellar masses of galaxies at different redshifts by using the SPS models of Maraston (2005), which include TP-AGB, with those of Bruzual & Charlot (2003), which do not include the TP-AGB. The authors show that there is a systematic effect on the stellar masses of galaxies between the results from Maraston (2005) and Bruzual & Charlot (2003) at all redshifts, though the effect may change with redshift depending on the galaxy populations. Here we apply only conservative corrections.

In this paper we calibrate all observations to a Bruzual & Charlot (2003) SPS model by applying the following systematic offsets:

$$\begin{aligned} M_{BC03} &= M_{BC07} + 0.13 = M_{P,0.1} - 0.05 = \\ &= M_{P,z} + 0.03 = M_{M05} + 0.2 = M_{FSPS} - 0.05. \end{aligned} \quad (38)$$

The subscript BC07 refers to the Bruzual (2007) SPS model, P,0.1 for PEGASE SPS model (Fioc & Rocca-Volmerange 1997) at $z \sim 0.1$ while P,z for PEGASE SPS model at high z . The subscript M05 refers to the Maraston (2005) SPS model and FSPS to the Conroy, Gunn & White (2009) SPS model. For the offset between BC03 and BC07 as well as for the offset between BC03 and M05 we used the analysis from Muzzin et al. (2009). For the PEGASE SPS model at $z \sim 0.1$ we use the offset noted by Bell & de Jong (2001) in their stellar mass-to-light ratios. For the PEGASE SPS model at high z we use the 0.03 dex offset reported in Pérez-González et al. (2008). Note that the latter offset is only applied to the GSMFs reported in Pérez-González et al. (2008). For the offset between BC03 and FSPS SPS models at $z \sim 0.1$ we use the offset estimated in Moustakas et al. (2013) based

on fitting the SDSS and GALAXES photometry using their ISEDFIT code for galaxies at $z \sim 0.1$, see their figure 19 and Figure 6 in Conroy (2013).

The choice of the dust attenuation model, star formation history, and metallicity are other sources of systematics when deriving stellar masses. For the dust attenuation model we calibrate all observations to a Calzetti et al. (2000) law. Based on the analysis carried out in Pérez-González et al. (2008), these authors found that a Charlot & Fall (2000) dust attenuation model gives, on average, galaxy stellar masses that are 0.1 dex larger compared to a Calzetti et al. (2000) law. In this paper we use this offset. Additionally, Muzzin et al. (2009) found that the median offsets for the Small and Large Magellanic Clouds and Milky-Way dust attenuation models are respectively -0.061, +0.036 and +0.05 dex. Finally, we assume that the choice of star formation histories and metallicity do not have any notable effect on the GSMF beyond the random uncertainties as demonstrated in Muzzin et al. (2013). Random uncertainties were discussed in Section 2.

To account for differences in cosmologies, To account for differences in cosmologies, we scale the GSMFs to our Planck Λ CDM cosmology with $\Omega_\Lambda = 0.693$, $\Omega_M = 0.307$, $h = 0.678$, and $h = 0.678$ using the relation we scale the GSMFs as:

$$\phi_{g,us} = \phi_{g,lit} \times \frac{V_{lit}}{V_{us}}, \quad (39)$$

where V is the comoving volume observed for each galaxy redshift survey

$$V = \int_{\Omega} \int_{z_i}^{z_f} \frac{d^2 V_c}{dz d\Omega} dz d\Omega. \quad (40)$$

Here, z_f and z_i are the maximum and minimum redshift where each GSMF has been observed, Ω is the solid angle of the survey, see Table 1, and V is the comoving volume in a Λ CDM universe (Hogg 1999). As for stellar masses we correct cosmology by simply $M_{*,us} = M_{*,lit} \times h_{lit}^2 / h_{us}^2$, where h is the Hubble parameter. Note, however, that the impact of accounting for different cosmologies is very small.

Finally, we do not account for any systematic effect due to cosmic variance.

4.1.2 Other Effects on the GSMF

Here we discuss more specific calibrations that are known to affect some observations of the GSMF.

We do not include aperture corrections. Previous studies (Bernardi et al. 2010, 2013, 2016) have found that the measurements of the light profiles based on the standard SDSS pipeline photometry could be underestimated due to sky subtraction issues. This could result in an underestimation of the abundance of massive galaxies up to a factor of five. While new algorithms have been developed for obtaining more precise measurements of the sky subtraction and thus to improve the photometry (Blanton et al. 2011; Simard et al. 2011; Meert, Vikram & Bernardi 2015) there is not yet a consensus. For this paper, we decided to ignore this correction that we may study in more detail in future works. Nevertheless, we apply photometric corrections to the GSMF reported in Li & White (2009). These authors used stellar masses estimations based on the SDSS r -band Petrosian

magnitudes. It is well known that using Petrosian magnitudes could result in an underestimation of the total light by an amount that could depend on the surface brightness profile of the galaxy and thus results in the underestimation of the total stellar mass. This will result in an artificial shift of the GSMF towards lower masses. In order to account for this shift for the Li & White (2009) GSMF, we apply a constant correction of 0.04 dex to all masses. As reported by Guo et al. (2010), this correction gives an accurate representation of the GSMF when the total light is considered, instead.

At $z \sim 0.1$ we use the GSMF derived in Rodríguez-Puebla et al. (in prep.) that has been corrected for the fraction of missing galaxies due to surface brightness limits by combining the SDSS NYU-VAGC low-redshift sample and the SDSS DR7 based on the methodology described in Blanton et al. (2005b). Following Baldry et al. (2012), we correct the GSMF for the distances based on Tonry et al. (2000). We found that including missing galaxies due to surface brightness incompleteness could increase the number of galaxies up to a factor of $\sim 2-3$ at the lowest masses, see Figure C1, and therefore have a direct impact on the SHMR. As for the new discoveries of the population of ultra-diffuse galaxies (UDGs van Dokkum et al. 2015a), their impact on the GSMF is not yet clear, nor is how to incorporate corrections due to surface brightness incompleteness. Note, however, that most of the UDGs have been discovered in massive clusters (particularly in the Coma Cluster van Dokkum et al. 2015a; Yagi et al. 2016), with very few examples in the field (e.g., Martínez-Delgado et al. 2016). If the UDG population is only common in Coma-like clusters, then we could conclude that the impact of UDGs on the GSMF would be minimum given the low frequency of such massive objects.

Finally, unlike for the local SDSS survey, at higher redshifts we do not expect significant surface brightness incompleteness at the low-mass end because (1) most of the high-redshift surveys employed by us are deep (e.g., COSMOS, UltraVISTA, CANDELS; these surveys have been shown to be complete in surface brightness down to their magnitude (mass) limits); and (2) at higher redshifts the galaxies tend to be more compact in the UV-optical bands than the local ones (see e.g. van der Wel et al. 2014), in such a way that they are expected to have higher surface brightnesses.

4.1.3 The Evolution of the local GSMF

Appendix D describes our inference of the GSMF from $z \sim 4$ to $z \sim 10$. In short, we use several UV LFs reported in the literature together with stellar mass-UV luminosity relations from Duncan et al. (2014); Song et al. (2015); Dayal et al. (2014) to derive the evolution of the GSMF from $z \sim 4$ to $z \sim 10$. We assume a survey area of 0.0778 deg^2 s as in the CANDELS survey (e.g., Song et al. 2015).

Figure 1 shows the evolution of the GSMF from $z \sim 0.1$ to $z \sim 10$. The filled circles show the mean of the observed GSMFs that we use through this paper in various redshift bins, while the error bars represent the propagation of the individual errors from the GSMF. Alternatively, we also compute standard deviations from the set of GSMF. We calculated the mean and the standard deviation of the observed GSMFs by using the bootstrapping approach of resampling with replacement. We use the bootstrapping ap-

Table 2. Observational data on the star formation rates

Author	Redshift ^a	SFR Estimator	Corrections	Type
Chen et al. (2009)	$z \sim 0.1$	H_α/H_β	S	All
Salim et al. (2007)	$z \sim 0.1$	UV SED	S	All
Noeske et al. (2007b)	$0.2 < z < 1.1$	UV+IR	S	All
Karim et al. (2011)	$0.2 < z < 3$	1.4 GHz	I+S+E	All
Dunne et al. (2009)	$0.45 < z < 2$	1.4 GHz	I+S+E	All
Kajisawa et al. (2010)	$0.5 < z < 3.5$	UV+IR	I	All
Whitaker et al. (2014)	$0.5 < z < 3$	UV+IR	I+S	All
Sobral et al. (2014)	$z \sim 2.23$	H_α	I+S+SP	SF
Reddy et al. (2012)	$2.3 < z < 3.7$	UV+IR	I+S+SP	SF
Magdis et al. (2010)	$z \sim 3$	FUV	I+S+SP	SF
Lee et al. (2011)	$3.3 < z < 4.3$	FUV	I+SP	SF
Lee et al. (2012)	$3.9 < z < 5$	FUV	I+SP	SF
González et al. (2012)	$4 < z < 6$	UV+IR	I+NE	SF
Salmon et al. (2015)	$4 < z < 6$	UV SED	I+NE+E	SF
Bouwens et al. (2011)	$4 < z < 7.2$	FUV	I+S	SF
Duncan et al. (2014)	$4 < z < 7$	UV SED	I+NE	SF
Shim et al. (2011)	$z \sim 4.4$	H_α	I+S+SP	SF
Steinhardt et al. (2014)	$z \sim 5$	UV SED	I+S	SF
González et al. (2010)	$z = 7.2$	UV+IR	I+NE	SF
This paper, Appendix D	$4 < z < 8$	FUV	I+E+NE	SF

Notes ^aIndicates the redshift used in this paper. I=IMF; S=Star formation calibration; E=Extinction; NE= Nebular Emissions; SP=SPS Model

proach since it allows us to empirically derive the distribution of current observations of the GSMFs and thus robustly infer the mean evolution of the GSMFs. Methodologically, we start by choosing various intervals in redshift as indicated in the labels in Figure 1. For each redshift bin, we create 30,000 bootstrap samples based on the observed distribution of all the GSMFs for that redshift bin, $\phi_{g_{\text{obs}}}(M_*, z)$, and then compute the median and its corresponding standard deviation from the distribution for a given stellar mass interval.

A few features of the mean evolution of the observed GSMF are worth mentioning at this point. At high redshifts the GSMF is described by a Schechter function, as has been pointed out in previous papers (see e.g., Grazian et al. 2015; Song et al. 2015; Duncan et al. 2014). At high redshifts, the faint-end slope becomes steeper (see e.g., Song et al. 2015; Duncan et al. 2014). As the galaxy population evolves, massive galaxies tend to pile up around $M_* \sim 3 \times 10^{10} M_\odot$ due to the increasing number of massive quenched galaxies at lower redshifts (see e.g., Bundy et al. 2006; Faber et al. 2007; Peng et al. 2010; Pozzetti et al. 2010; Muzzin et al. 2013). These represent a second component that is well described by a Schechter function, and thus the resulting GSMF at low redshifts is better described by a double Schechter function.

4.2 Star Formation Rates

In this paper, we use a compilation of 19 studies from the literature for the observed SFRs as a function of stellar mass at different redshifts. Table 2 lists the references that we utilize.

As for the GSMFs, in order to directly compare the different SFR samples we applied some calibrations. To do so, we follow Speagle et al. (2014) who used a compilation to study star formation from $z \sim 0$ to $z \sim 6$ by correcting

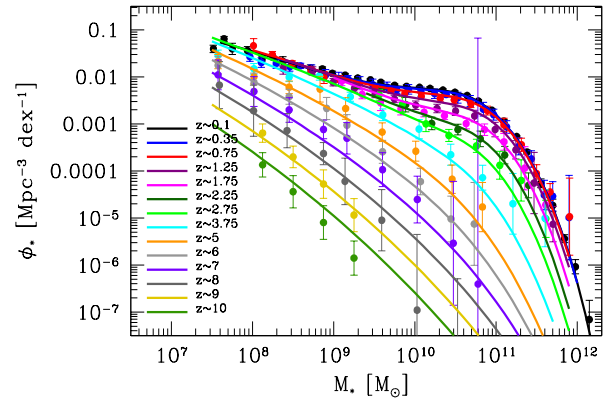


Figure 1. Redshift evolution from $z \sim 0.1$ to $z \sim 10$ of the galaxy stellar mass function (GSMF) derived by using 20 observational samples from the literature and represented with the filled circles with error bars. The various GSMFs have been homogenized and corrected for potential systematics that could affect our results, see the text for details. Solid lines are the best fit model from a set of 3×10^5 MCMC trials, see Section 5. These fits take into account uncertainties affecting the GSMF as discussed in the text. Note that at lower redshifts ($z \lesssim 3$) galaxies tend to pile up at $M_* \sim 3 \times 10^{10} M_\odot$ due to the increase in the number of massive quenched galaxies at lower redshifts.

for different assumptions regarding the IMF, SFR indicators, SPS models, dust extinction, emission lines and cosmology. The reader is referred to that paper for details on their calibrations. In Table 2 we indicate the specific calibrations applied to the data. Note that in order to constrain our model we use observations of the SFRs for *all* galaxies.

Complete samples, however, for all galaxies are only available at $z < 3$. Therefore, here we decided to include SFRs samples from star-forming galaxies, especially at high $z > 3$. Using only star-forming galaxies at high redshift is not a big source of uncertainty since most of the galaxies at $z > 3$ are actually star forming, see e.g. Figure 2. The last column of Table 2 indicates the type of the data, namely, if the sample is for all galaxies or for star-forming galaxies, and the redshift range.

In addition to the compiled sample for $z > 3$, here we calculate average SFRs using again the UV LFs described in Appendix D. We begin by correcting the UV rest-frame absolute magnitudes for extinction using the Meurer, Heckman & Calzetti (1999) average relation

$$\langle A_{UV} \rangle = 4.43 + 1.99\langle\beta\rangle, \quad (41)$$

where $\langle\beta\rangle$ is the average slope of the observed UV continuum. We use the following relationship independent of redshift: $\langle\beta\rangle = -0.11 \times (M_{UV} + 19.5) - 2$, which is consistent with previous determination of the β slope (see e.g., Bouwens et al. 2014). Then we calculate UV SFRs using the Kennicutt (1998) relationship

$$\frac{\text{SFR}}{M_{\odot} \text{ yr}^{-1}} (L_{UV}) = \frac{L_{UV}/\text{erg s}^{-1} \text{ Hz}^{-1}}{13.9 \times 10^{27}}. \quad (42)$$

We subtract -0.24 dex to be consistent with a Chabrier (2003) IMF. Finally, we calculate the average SFR as a function of stellar mass as

$$\langle \log \text{SFR} (M_*, z) \rangle = \phi_*^{-1}(M_*, z) \int P(M_* | M_{UV}, z) \times \log \text{SFR}(M_{UV}) \phi_{UV}(M_{UV}, z) dM_{UV}. \quad (43)$$

Both the probability distribution function $P(M_* | M_{UV}, z)$ and the function $\phi_*(M_*, z)$ are described in detail in Appendix D. We use the following intervals of integration: $M_{UV} \in [-17, -22.6]$ at $z = 4$; $M_{UV} \in [-16.4, -23]$ at $z = 5$; $M_{UV} \in [-16.75, -22.5]$ at $z = 6$; $M_{UV} \in [-17, -22.75]$ at $z = 7$ and $M_{UV} \in [-17.25, -22]$ at $z = 8$.

4.3 Cosmic Star Formation Rate

We use the CSFR data compilation from Madau & Dickinson (2014). This data was derived from FUV and IR rest frame luminosities by deriving empirical dust corrections to the FUV data in order to estimate robust CSFRs. We adjusted their data to a Chabrier (2003) IMF by subtracting 0.24 dex from their CSFRs. Finally, for $z > 3$ we calculate the CSFR using again the UV dust-corrected LFs and SFRs described above and using the same integration limit as in Madau & Dickinson (2014). We find that our CSFR is consistent with the compilation derived in Madau & Dickinson (2014) over the same redshift range.

4.4 The Fraction of Star-Forming and Quiescent Galaxies

In this paper we interchangeably refer to star-forming galaxies as blue galaxies and quiescent galaxies as red galaxies. We utilize the fraction of blue/star-forming and red/quenched galaxies as a reference to compare with our model and thus gain more insights on how galaxies evolve from active to passive as well as on their structural evolution (discussed in

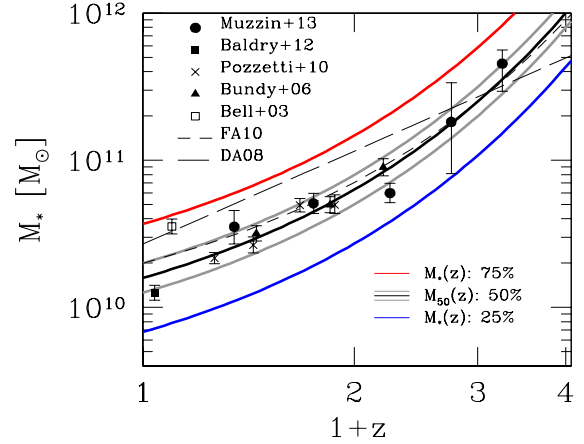


Figure 2. The stellar mass $M_{50}(z)$ at which the fractions of blue star-forming and red quenched galaxies are both 50%. The open square with error bars shows the transition mass for local galaxies as derived in Bell et al. (2003) based on the SDSS DR2, while the filled triangles show the transition mass derived in Bundy et al. (2006) based on the DEEP2 survey. Drory & Alvarez (2008) based on the FORS Deep Field survey is indicated with the long dashed line; observations from Pozzetti et al. (2010) based on the COSMOS survey are indicated with the x symbols; observations from Baldry et al. (2012) based on the GAMA survey are shown with a filled square; and observations from Muzzin et al. (2013) based on the COSMOS/ULTRAVISTA survey are shown as filled circles. The empirical results based on abundance matching by Firmani & Avila-Reese (2010) are shown with the short dashed lines. The solid black line shows the relation $\log(M_{50}(z)/M_{\odot}) = 10.2 + 0.6z$ employed in this paper, which is consistent with most of the above studies. The gray solid lines show the results when shifting $(M_{50}(z)/M_{\odot})$ 0.1 dex higher and lower. The red (blue) curves show the stellar mass vs. z where 75% (25%) of the galaxies are quenched.

Section 7). For the fraction of quiescent galaxies f_Q we use the following relation:

$$f_Q(M_*, z) = \frac{1}{1 + (M_*/M_{50}(z))^{\alpha}}, \quad (44)$$

where M_{50} is the transition stellar mass at which the fractions of blue star-forming and red quenched galaxies are both 50%. Figure 2 shows M_{50} as a function of redshift from observations and previous constraints. The solid black line shows the relation $\log(M_{50}(z)/M_{\odot}) = 10.2 + 0.6z$ that we will employ in this paper, and the gray solid lines show the results when shifting $(M_{50}(z)/M_{\odot})$ by 0.1 dex above and below. We will use this shift as our uncertainty in the definition for $\log(M_{50}(z)/M_{\odot})$. The red (blue) curves in the figure show the stellar mass vs. redshift where 75% (25%) of the galaxies are quenched. Finally, we will assume that $\alpha = -1.3$. The transition stellar mass is such that at $z = 0$ $\log(M_{50}(z)/M_{\odot}) = 10.2$ and at $z = 2$ $\log(M_{50}(z)/M_{\odot}) = 11.4$.

We note that our statistical treatment of quenched vs. star-forming galaxies is rather different from a common approach in the literature, in which a given galaxy is considered to be quenched based on its specific star formation rate and redshift. For example, Pandya et al. (2016) defines transi-

tion galaxies to have sSFR between 0.6 dex (1.5σ) and 1.4 dex (3.5σ) below the star-forming main sequence, with fully quenched galaxies having sSFR even farther below the main sequence. But our statistical approach does not permit this.

5 CONSTRAINING THE MODEL

The galaxy population in our model is described by four properties: halo mass M_{vir} , halo mass accretion rates, stellar mass M_* , and star formation rate SFR. In order to constrain the model we combine several observational data sets, including the GSMFs, the SFRs and the CSFR for all galaxies. In this Section we describe our adopted methodology as well as the best resulting fit parameters in our model.

In order to sample the best-fit parameters that maximize the likelihood function $L \propto e^{-\chi^2/2}$ we use the MCMC approach, described in detail in Rodríguez-Puebla, Avila-Reese & Drory (2013).

We compute the total χ^2 as,

$$\chi^2 = \chi_{\text{GSMF}}^2 + \chi_{\text{SFR}}^2 + \chi_{\text{CSFR}}^2 \quad (45)$$

where for the GSMFs we define

$$\chi_{\text{GSMF}}^2 = \sum_{j,i} \chi_{\phi_{j,i}}^2, \quad (46)$$

for the SFRs

$$\chi_{\text{SFR}}^2 = \sum_{j,i} \chi_{\text{SFR}_{j,i}}^2, \quad (47)$$

and for the CSFRs

$$\chi_{\text{CSFR}}^2 = \sum_i \chi_{\rho_i}^2. \quad (48)$$

In all the equations the sum over j refers to different stellar mass bins while i refers to summation over different redshifts. The fittings are made to the data points with their error bars of each GSMF, SFR and CSFR.

In total our galaxy model consists of eighteen adjustable parameters. Fifteen are to model the redshift evolution of the SHMR, Equations (27)–(31): $\vec{p}_{\text{SHMR}} = \{\epsilon_0, \epsilon_1, \epsilon_2, \epsilon_3, M_{C0}, M_{C1}, M_{C2}, \alpha, \alpha_1, \alpha_2, \delta_0, \delta_1, \delta_2, \gamma_0, \gamma_1\}$; and three more to model the fraction of stellar mass growth due to in-situ star formation: $\vec{p}_{\text{in situ}} = \{M_{\text{in situ},0}, M_{\text{in situ},1}, \beta\}$. To sample the best fit parameters in our model we run a set of 3×10^5 MCMC models. The resulting best-fit parameters are given in Equations (49) – (55).

Figure 1 shows the best-fit model GSMFs from $z \sim 0.1$ to $z \sim 10$ with the solid lines as indicated by the labels. This figure shows the evolution of the observed GSMF based in our compiled data described in Section 4.1.

Figure 3 shows the SFRs as a function of redshift z in five stellar mass bins. The observed SFRs from the literature are plotted with filled circles with error bars while the best fit model is plotted with the solid black lines. We also present our best fitting models by plotting the specific SFRs as a function of stellar mass in Figure 4. Note that our model fits describe rather well the observations at all mass bins and all redshifts.

We present the best-fit model to the CSFR in the upper Panel of Figure 5. The observed CSFRs employed for constraining the model are shown with the solid circles and

error bars. The lower Panel of Figure 5 compares the cosmic stellar mass density predicted by our model fit with the data compiled in the review by Madau & Dickinson (2014); the agreement is impressive.

In Appendix A we discuss the impact of the different assumptions employed in the modelling. The best fitting parameters to our model are as follows:

$$\begin{aligned} \log(\epsilon(z)) &= -1.758 \pm 0.040 + \\ &\mathcal{P}(0.110 \pm 0.166, -0.061 \pm 0.029, z) \times \mathcal{Q}(z) + \\ &\mathcal{P}(-0.023 \pm 0.009, 0, z), \end{aligned} \quad (49)$$

$$\begin{aligned} \log(M_0(z)) &= 11.548 \pm 0.049 + \\ &\mathcal{P}(-1.297 \pm 0.225, -0.026 \pm 0.043, z) \times \mathcal{Q}(z), \end{aligned} \quad (50)$$

$$\begin{aligned} \alpha(z) &= 1.975 \pm 0.074 + \\ &\mathcal{P}(0.714 \pm 0.165, 0.042 \pm 0.017, z) \times \mathcal{Q}(z), \end{aligned} \quad (51)$$

$$\begin{aligned} \delta(z) &= 3.390 \pm 0.281 + \\ &\mathcal{P}(-0.472 \pm 0.899, -0.931 \pm 0.147, z) \times \mathcal{Q}(z), \end{aligned} \quad (52)$$

$$\gamma(z) = 0.498 \pm 0.044 + \mathcal{P}(-0.157 \pm 0.122, 0, z) \times \mathcal{Q}(z), \quad (53)$$

$$\begin{aligned} \log(M_{\text{in situ}}(z)) &= 12.728 \pm 0.163 + \\ &\mathcal{P}(2.790 \pm 0.163, 0, z), \end{aligned} \quad (54)$$

$$\beta(z) = 0.760 \pm 0.032 + \log(1 + z). \quad (55)$$

For our best fitting model we find that $\chi^2 = 522.8$ from a number of $N_d = 488$ observational data points. Since our model consist of $N_p = 18$ free parameters the resulting reduced χ^2 is $\chi^2/\text{d.o.f.} = 1.11$.

6 THE GALAXY-HALO CONNECTION

6.1 The Stellar-to-Halo Mass Relation from

$z \sim 0.1$ to $z \sim 10$

The upper panel of Figure 6 shows the constrained evolution of the SHMR while the lower panel shows the stellar-to-halo mass ratio from $z \sim 0.1$ to $z \sim 10$. Recall that in the case of central galaxies we refer to M_{halo} as the virial mass M_{vir} of the host halo, while for satellites M_{halo} refers to the maximum mass M_{peak} reached along the main progenitor assembly history. Consistent with previous results the SHMR appears to evolve only very slowly below $z \sim 1$. This situation is quite different between $z \sim 1$ and $z \sim 7$, where at a fixed halo mass the mean stellar mass is lower at higher redshifts. The middle panel of the same figure shows the 1σ confidence intervals of our constrained SHMRs from the 3×10^5 MCMC models. Finally, we estimate at each redshift the largest halo mass that will be observed using the solid angles and redshift bins of the surveys from Table 1. We use these halo masses as the upper bounds to the virial halo masses shown in Figure 6. Finally, Table 3 lists the range over which our mass relations can be trust.

The maximum of the stellar-to-halo mass ratio is around $M_{\text{vir}} \sim 10^{12} M_{\odot}$ at $z \sim 0.1$ with a value of ~ 0.03 . The maximum moves to higher mass halos at higher redshifts up to $z \sim 3$, consistent with previous studies (see e.g., Conroy & Wechsler 2009; Firmani & Avila-Reese 2010; Behroozi, Conroy & Wechsler 2010; Leauthaud et al. 2012; Yang et al. 2012; Behroozi, Wechsler & Conroy 2013b; Moster, Naab & White 2013; Skibba et al. 2015). The value of the maximum of the stellar-to-halo mass ratio moves to

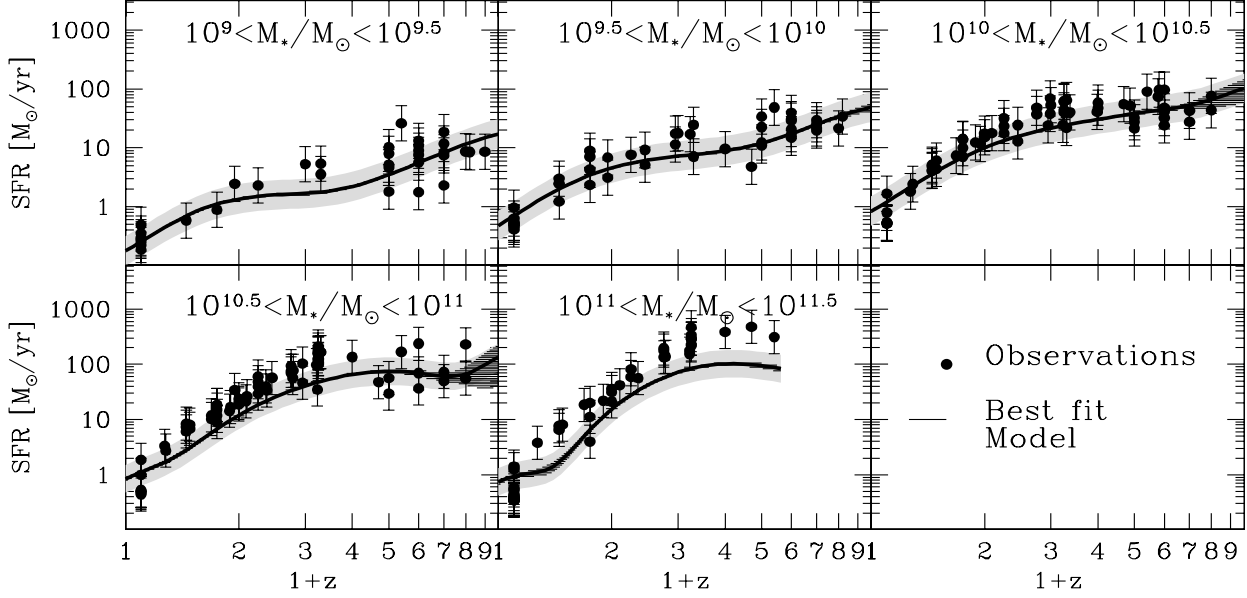


Figure 3. Star formation rates as a function of redshift z in five stellar mass bins. Black solid lines shows the resulting best fit model to the SFRs implied by our approach. The filled circles with error bars show the observed data as described in the text, see Section 2.

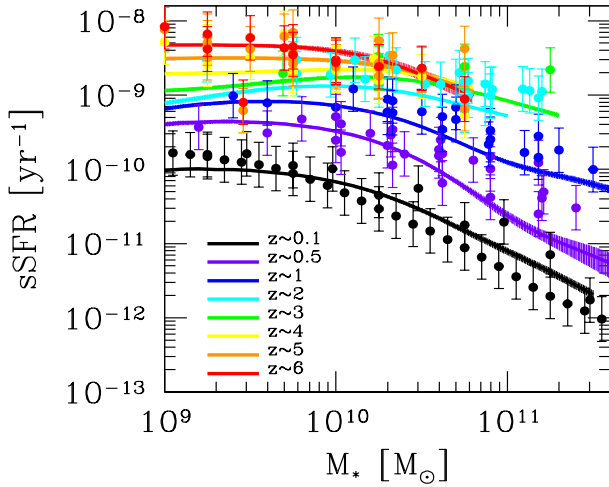


Figure 4. Specific SFRs as a function of stellar mass from $z \sim 0.1$ to $z \sim 6$. The solid lines show our best fitting model while the shaded areas show the 1σ confidence intervals using our set of MCMC trials. The filled circles show the observations we utilize to constrain our model.

lower values with increasing redshift, decreasing by approximately a factor of 3 between $z \sim 0.1$ and $z \sim 4$. At redshift $z \sim 7$ the stellar-to-halo mass ratio has decreased by an order of magnitude. Nonetheless, given the uncertainties when deriving the GSMFs at high redshifts $z > 4$, this result should be taken with caution. For comparison, the dashed lines in both panels show the cosmic baryon fraction im-

Table 3. Minimum and maximum halo masses over which our mass relations can be trusted.

z	$\log M_{\text{vir,min}} [M_{\odot}]$	$\log M_{\text{vir,max}} [M_{\odot}]$
0.1	10.3	15.0
0.5	10.8	14.3
1	11.0	14.1
2	11.5	13.7
3	10.6	13.3
4	10.2	12.3
5	10.2	12.0
6	10.2	11.7
7	10.2	11.4
8	10.2	11.1
9	10.3	11.1
10	10.3	11.1

plied by the Planck Collaboration et al. (2016) cosmology, $f_b = \Omega_B / \Omega_M \approx 0.16$.

Next we study the integral stellar conversion efficiency, defined as $\eta = f_*/f_b$. This is shown in the left panel of Figure 7 for progenitors of dark matter halos with masses between $M_{\text{vir}} = 10^{11} M_{\odot}$ and $M_{\text{vir}} = 10^{15} M_{\odot}$ at $z = 0$. Dark matter halos are most efficient when their progenitors reached masses between $M_{\text{vir}} \sim 5 \times 10^{11} M_{\odot} - 2 \times 10^{12} M_{\odot}$ at $z < 1$, and the stellar conversion efficiency is never larger than $\eta \sim 0.2$. Note that Zehavi et al. (2011) reached a similar conclusion when estimating the HOD model of the SDSS survey utilizing the observed galaxy clustering. Theoretically, the characteristic halo mass of $\sim 10^{12} h^{-1} M_{\odot}$ is expected to mark a transition above which the stellar conversion becomes increasingly inefficient. The reason is that at halo masses above $10^{12} h^{-1} M_{\odot}$ the efficiency at which

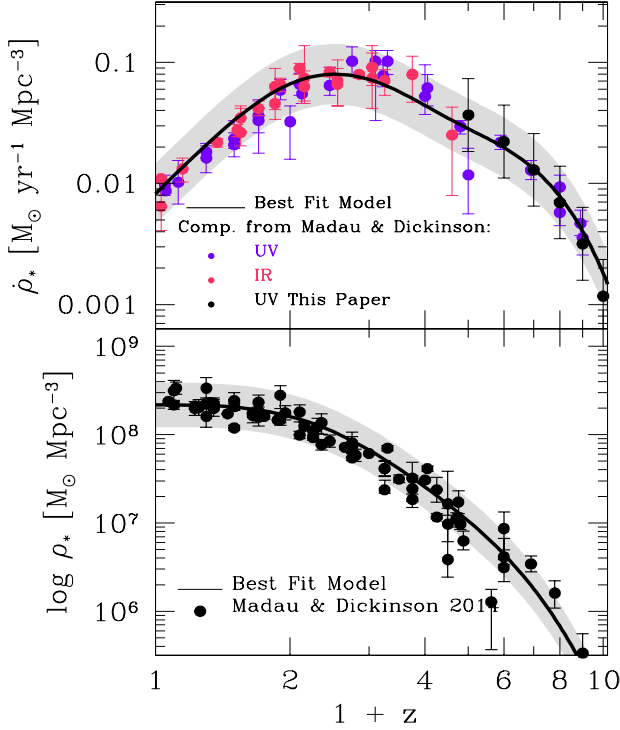


Figure 5. Upper Panel: Cosmic star formation rate, CSFR. The solid black line shows the resulting best fit model to the CSFR as described in Section 2.4. Filled red and violet circles show a set of compiled observations by Madau & Dickinson (2014) from FUV+IR rest frame luminosities. UV luminosities are dust-corrected. Black solid circles show the results from the UV dust-corrected luminosity functions described in Appendix D. **Lower Panel:** Cosmic stellar mass density. The solid black line shows the predictions for our best fit model. Filled black circles show the data points compiled in Madau & Dickinson (2014). All data was adjusted to the IMF of Chabrier (2003). In both panels, the light grey shaded area shows the systematic assumed to be of 0.25 dex.

the virial shocks form and heat the incoming gas increases (e.g., Dekel & Birnboim 2006). Additionally, in such massive galaxies the gas can be kept from cooling by the feedback from active galactic nuclei (Croton et al. 2006; Cattaneo et al. 2008; Henriques et al. 2015; Somerville & Davé 2015, and references therein). Central galaxies in massive halos are therefore expected, in a first approximation, to become passive systems roughly at the epoch when the halo reaches the mass of $10^{12} h^{-1} M_\odot$, thus the term halo mass quenching. On the other hand, the less massive the halos, the less efficient their growth in stellar mass is expected to be due to supernova-driven gas loss in their lower gravitational potentials.

The right panel of Figure 7 shows the stellar conversion efficiency for the corresponding stellar mass growth histories of the halo progenitors discussed above. The range of the transition stellar mass $M_{50}(z)$, defined as the stellar mass at which the fraction of star forming is equal to the fraction of quenched galaxies (see Figure 2 and Section 7), is shown by the dashed lines. Below these lines galaxies are more likely to be star forming. Note that the right panel of Figure 7 shows

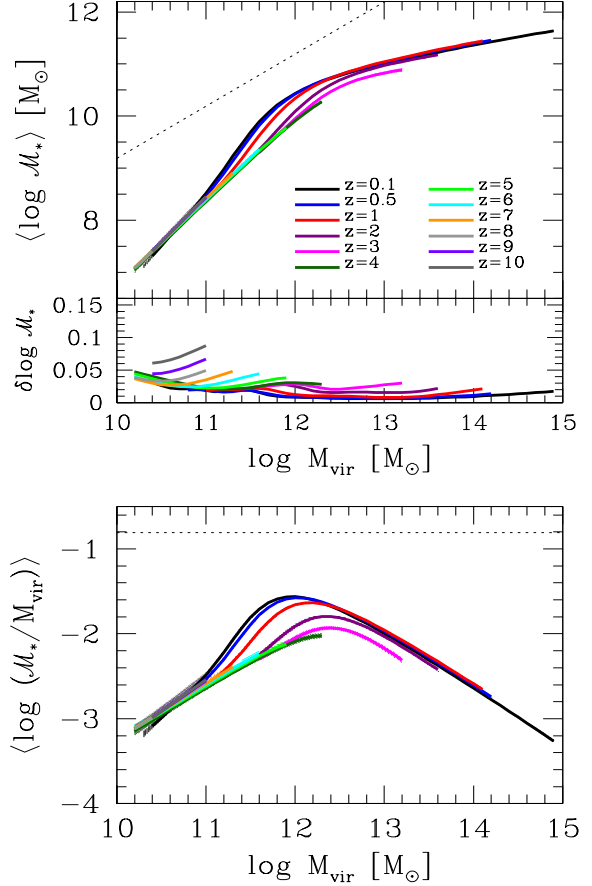


Figure 6. Upper panel: Evolution of the mean stellar-to-halo mass relation from $z = 0.1$ to $z = 10$ as indicated in the legends. In our model we assume that these relations are valid both for central and satellite galaxies as explained in the text. The relations are shown only up to the largest halo mass that will be observed using the solid angles and redshift bins of the surveys from Table 1. Table 3 lists the range over which our mass relations can be trusted. **Middle panel:** 1σ confidence intervals from the 3×10^5 MCMC trials. **Bottom panel:** Evolution of the stellar-to-halo mass ratios M_*/M_{vir} for the same redshifts as above. The dotted lines in both panels show the limits corresponding to the cosmic baryon fraction $\Omega_B/\Omega_M \approx 0.16$.

that $M_{50}(z)$ roughly coincides with where η is maximum, especially at low z . This reflects the fact that halo mass quenching is part of the physical mechanisms that quench galaxies in massive halos. We will come back to this point in Section 8.2.

Finally, Figure 8 shows the trajectories for the M_*/M_{vir} ratios of progenitors of dark matter halos with masses between $M_{\text{vir}} = 10^{11} M_\odot$ and $M_{\text{vir}} = 10^{15} M_\odot$ at $z = 0$. Note that galaxies in halos above $M_{\text{vir}} = 10^{12} M_\odot$ had a maximum followed by a decline of their M_*/M_{vir} ratio, while this ratio for galaxies in less massive halos continues increasing today.

6.2 Galaxy Growth and Star-Formation Histories

Figure 9 shows the predicted star formation histories for progenitors of average dark matter halos at $z = 0$ with

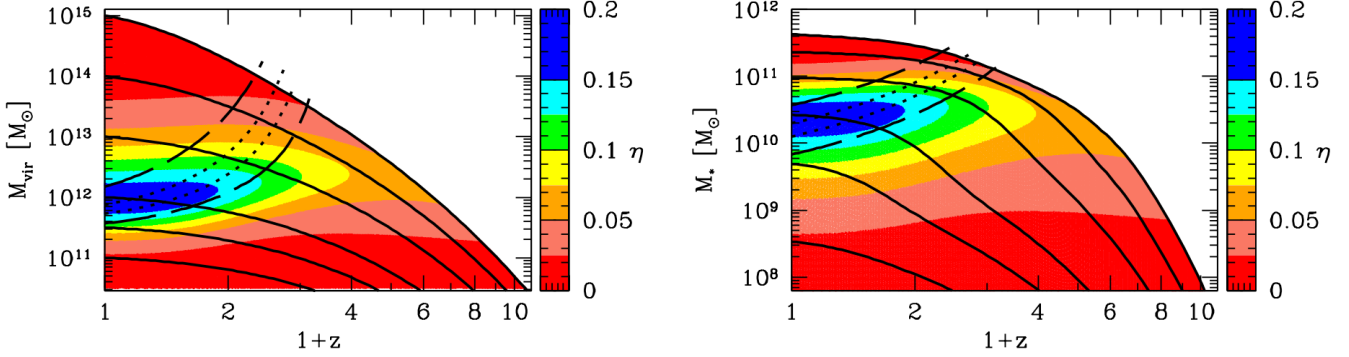


Figure 7. **Left Panel:** Integral stellar conversion efficiency, defined as $\eta = f_*/f_b$, as a function of halo mass for progenitors at $z = 0$. The black solid lines show the trajectories for progenitors with $M_{\text{vir}} = 10^{11}, 10^{11.5}, 10^{12}, 10^{13}, 10^{14}$ and $10^{15} M_{\odot}$. **Right Panel:** Integral stellar conversion efficiency η but now as a function of stellar mass for the corresponding halo progenitors. The stellar conversion efficiency is higher at low redshifts, $z \sim 0$, and highest for halo progenitors at $z = 0.1$ between $M_{\text{vir}} \sim 5 \times 10^{11} M_{\odot} - 2 \times 10^{12} M_{\odot}$ corresponding to galaxies between $M_* \sim 10^{10} M_{\odot} - 4 \times 10^{10} M_{\odot}$. In both panels, the dotted lines show $M_{50}(z)$ above which 50% of the galaxies are statistically quenched, and the upper (lower) long-dash curves show the mass vs. z where 75% (25%) of the galaxies are quenched.

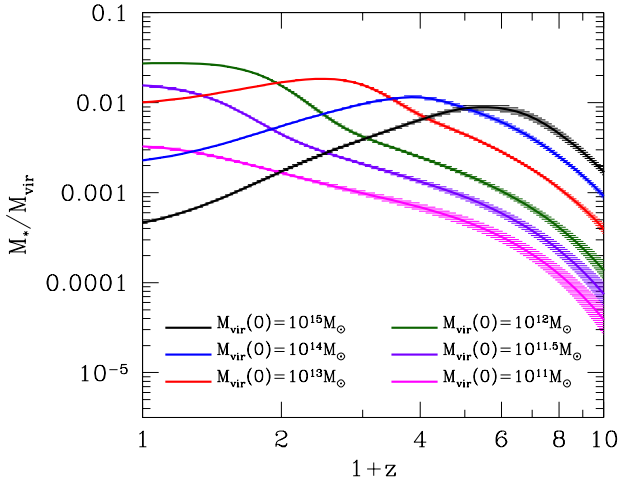


Figure 8. Evolution of the stellar-to-halo mass ratio for progenitors with $M_{\text{vir}} = 10^{11}, 10^{11.5}, 10^{12}, 10^{13}, 10^{14}$ and $10^{15} M_{\odot}$ at $z = 0$.

masses between $M_{\text{vir}} = 10^{11} M_{\odot}$ and $M_{\text{vir}} = 10^{15} M_{\odot}$. Panel a) shows the resulting 3D surface for the redshift evolution of the stellar-to-halo mass relation for progenitors of dark matter halos at $z = 0$. We color code the star formation rates as indicated by the vertical label. For reference, the solid black lines show the average trajectories for progenitors with $M_{\text{vir}} = 10^{11}, 10^{11.5}, 10^{12}, 10^{13}, 10^{14}$ and $10^{15} M_{\odot}$. Panel b) shows the evolution of the SHMRs for the same progenitors while panels c) and d) show, respectively, the projections of star formation histories as a function of halo mass and their corresponding stellar masses. Previous studies have shown related figures to the panels in Figure 9 (see e.g., Firmani & Avila-Reese 2010; Krumholz & Dekel 2012; Behroozi, Wechsler & Conroy 2013b; Yang et al. 2013). We note that our results are qualitatively similar to these pre-

vious studies, updated by using more recent observational data for the GSMFs, SFRs and the CSFR.

Figure 9 shows that the star formation histories in the most massive halos, $M_{\text{vir}} \gtrsim 10^{13} M_{\odot}$, increased with redshift reaching a maximum value between $z \sim 1 - 4$. On average, the most massive halos could reach SFRs as high as $\text{SFR} \sim 200 M_{\odot}/\text{yr}$ in this redshift interval. Following this very intense period of star formation their SFR decreases, and by $z \sim 0.1$ they are already quenched. This implies that in the most massive halos the stellar mass of their galaxy was already in place since $z \sim 1$. In contrast, galaxies in low mass halos ($M_{\text{vir}} \sim 10^{11} M_{\odot}$) on average form stars late and approximately at a constant rate, with very low rates typically below $\text{SFR} \sim 0.1 M_{\odot}/\text{yr}$. As for MW-sized halos ($M_{\text{vir}} \sim 10^{12} M_{\odot}$), it seems that their galaxies went through various phases. The first phase is a moderate rate of growth up to ~ 1.5 . They reach an intense period of star formation around $z \sim 1$, with values around $\sim 10 M_{\odot}/\text{yr}$, and then decline. According to our model this period of intense star formation is not associated with galaxy mergers as we will discuss in next subsection.

It is interesting that panel b) shows that the spread of trajectories of the galaxies in the SHMR plane is very narrow, giving the impression that the SHMR is time independent. Recall that Figure 9 shows the backwards trajectories for halos at $z = 0$ (i.e., their progenitors) reflecting the fact that halo mass (and consequently galaxy mass) is, on average, increasing at all redshifts. As discussed in previous studies, a roughly time independent SHMR for $0 \lesssim z \lesssim 4$ is consistent with observed evolution of the SFRs, especially for star-forming main sequence galaxies (Behroozi, Wechsler & Conroy 2013a; Rodríguez-Puebla et al. 2016b).

Theoretically, it is expected that dark matter halos control the growth of their host galaxies (see e.g. Bouché et al. 2010; Dekel et al. 2009; Davé, Finlator & Oppenheimer 2012; Krumholz & Dekel 2012; Dekel et al. 2013; Dekel & Mandelker 2014; Mitra, Davé & Finlator 2015; Feldmann 2015; Feldmann & Mayer 2015; Rodríguez-Puebla et al. 2016b). We investigate this in the left panel of Figure 10 where

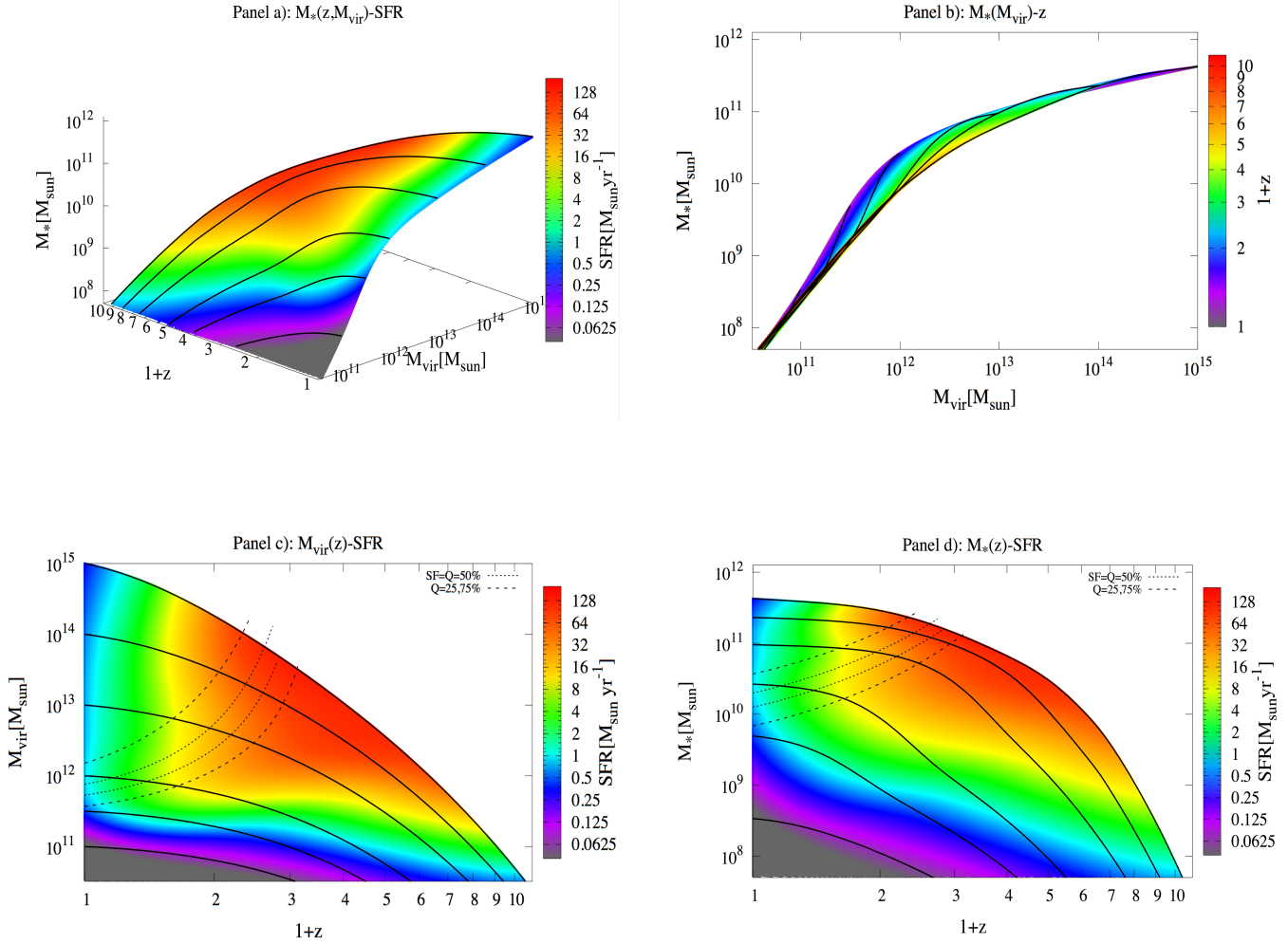


Figure 9. Panel a): Galaxy SFRs as a function of redshift, halo mass, and stellar mass. The solid lines indicate the average trajectories corresponding to progenitors at $z = 0$ with $M_{\text{vir}} = 10^{11}, 10^{11.5}, 10^{12}, 10^{13}, 10^{14}$ and $10^{15} M_{\odot}$. The color code shows the SFRs. Panel b): Galaxy growth trajectories in the stellar-to-halo mass plane (this is a projection of Panel a) when collapsing over the redshift axis). Panel c): Galaxy SFRs along the halo mass trajectories (this is a projection of the Panel a) when collapsing over the M_* axis). Panel d): Galaxy SFRs along the stellar mass trajectories (this is a projection of the Panel a) when collapsing over the M_{vir} axis). The dotted lines show $M_{50}(z)$ above which 50% of the galaxies are statistically quenched, and the upper (lower) long-dash curves show the mass vs. z where 75% (25%) of the galaxies are quenched.

we plot the ratio between the specific star formation rate (sSFR = SFR/M_*) and the specific halo mass accretion rate (sMAR = $(dM_{\text{vir}}/dt)/M_{\text{vir}}$), i.e., sSFR/sMAR, as a function of halo mass.⁶ Hereafter, we refer to the ratio sSFR/sMAR as the instantaneous halo star formation efficiency.⁷ Similarly to our definition of SFRs, halo MARs were measured

⁶ Observe that the sSFR and the sMAR have units of the inverse of time. One can interpret them as the characteristic time that it will take galaxies and halos to double their mass at a constant assembly rate. Therefore the ratio $\text{sSFR}/\text{sMAR} = t_h/t_g$ measures how fast galaxies are gaining stellar mass compared to their halos gaining total mass.

⁷ Do not confuse the instantaneous halo star formation efficiency with the halo stellar conversion efficiency $\eta = f_*/f_b$. The for-

mer is an instantaneous quantity while the latter is an integral (cumulative) quantity.

mer is an instantaneous quantity while the latter is an integral (cumulative) quantity.

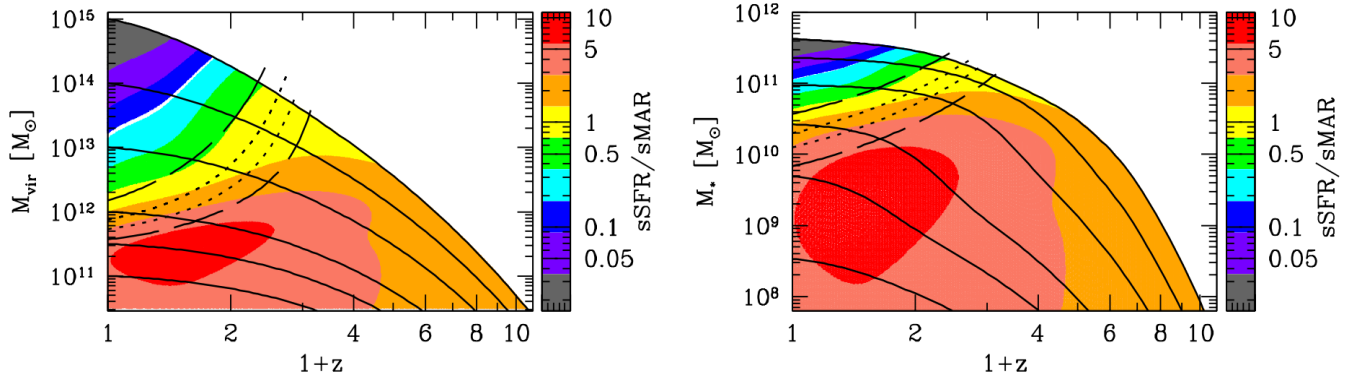


Figure 10. Halo star formation efficiencies, defined as sSFR/sMAR , as a function of halo mass (left panel) and stellar mass (right panel) for halo progenitors at $z = 0$. The black solid lines show the trajectories for progenitors with $M_{\text{vir}} = 10^{11}, 10^{11.5}, 10^{12}, 10^{13}, 10^{14}$ and $10^{15} M_{\odot}$. The short dashed lines show the stellar mass and halo mass at which the observed fraction of star-forming galaxies is equal to the quenched fraction of galaxies, and the upper (lower) long-dash curves show the stellar mass vs. z where 75% (25%) of the galaxies are quenched.

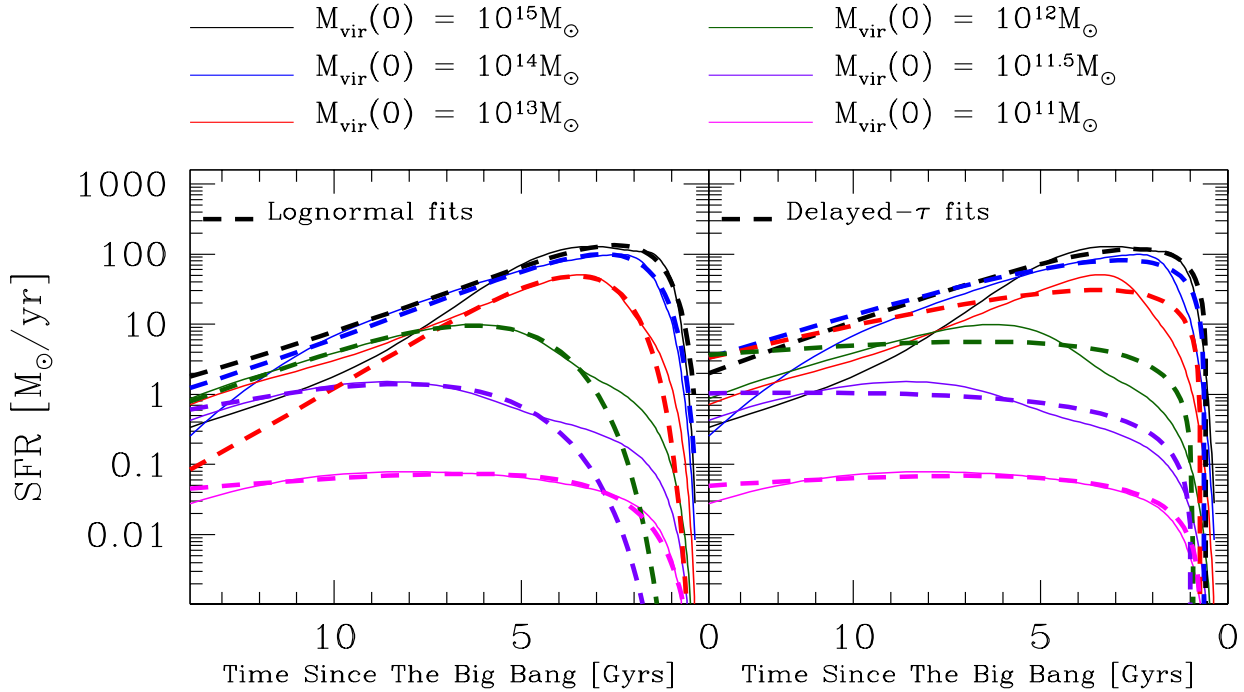


Figure 11. Analytic fits to the star formation histories as indicated by the labels. **Left Panel:** Lognormal fits. **Right Panel:** Delayed- τ fits. Note that lognormal fits describe rather well the average star formation histories of galaxies in halos with masses around and below about $M_{\text{vir}} = 10^{12} M_{\odot}$ after the first few Gyr. Delayed- τ fits are poor at all but the lowest masses.

universal halo mass (in the sense of it being time independent) at which the halo star formation efficiency transits above and below unity, rather this transition mass depends on redshift. The transition occurs around $M_{\text{vir}} \sim 10^{12} M_{\odot}$ at $z \sim 0$ and $M_{\text{vir}} \sim 10^{13} M_{\odot}$ at $z \sim 3$. Additionally, Figure 10 shows that halo star formation efficiencies of $\sim 2 - 5$ are typical of low mass halos. However, we find that halo star formation efficiencies as high as ~ 10 are reached in halos with $M_{\text{vir}} \sim 2 \times 10^{11} M_{\odot}$ between $z \sim 0.1 - 1.5$. This im-

plies a total disconnection between galaxies and halos. We will come back to this point below. The right panel of the same figure shows the corresponding star formation efficiencies as a function of stellar mass. The 50% stellar mass at which the numbers of star-forming and quenched galaxies are equal is shown as the short dashed lines in both panels (see also Figure 2). In Figure 10 we observe that galaxies are more likely to be star-forming when their halo star formation efficiencies are above $\text{sSFR}/\text{sMAR} \sim 1$. That is, low-mass

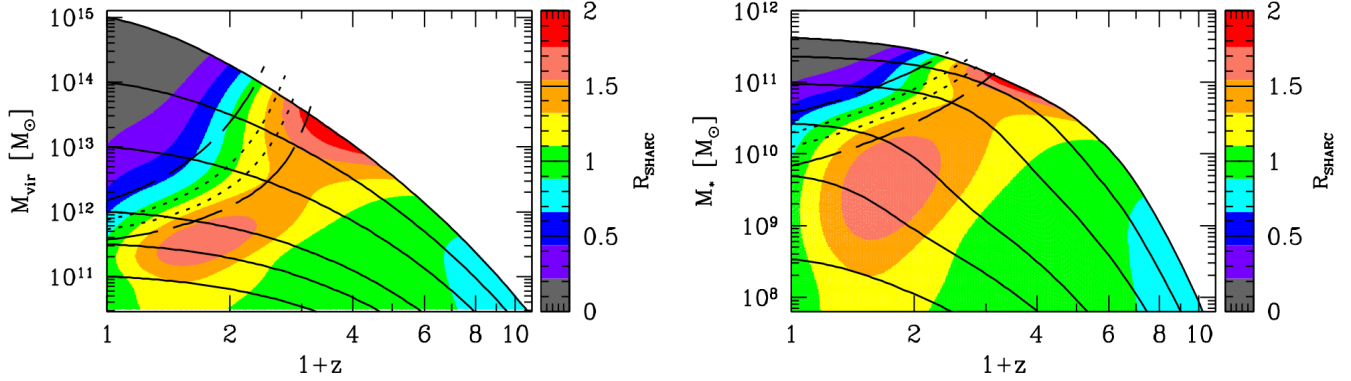


Figure 12. Left Panel: Stellar-halo accretion rate coevolution (SHARC) assumption as a function of halo mass for progenitors at $z = 0$. The black solid lines show the trajectories for progenitors with $M_{\text{vir}} = 10^{11}, 10^{11.5}, 10^{12}, 10^{13}, 10^{14}$ and $10^{15} M_{\odot}$. **Right Panel:** Like the left panel, but as a function of stellar mass for their corresponding halo progenitors. These figures show that the SHARC assumption is a good approximation within a factor of ~ 2 for star-forming galaxies, which are a majority of those below the quenching curves. Recall that in both panels, the dashed lines denote $M_{50}(z)$ below/above which 50% of the galaxies are star-forming/quenched, and the upper (lower) long-dash curves show the stellar mass vs. z where 75% (25%) of the galaxies are quenched.

galaxies form stars much faster than low mass halos gain mass. In contrast, galaxies with star-formation efficiencies below $\text{sSFR}/\text{sMAR} \sim 1$ are more likely to be quenched as a result of high mass halos growing faster compared to their host galaxies. The above behaviours are commonly referred in the literature as downsizing in SFR and archeological or mass downsizing respectively (e.g., Conroy & Wechsler 2009; Firmani & Avila-Reese 2010, and references therein). The former implies that low-mass galaxies delayed the stellar mass assembly with respect to their halos, while the latter implies that the more massive the galaxies, the earlier their mass growth was quenched while their halos continued growing. It is interesting to note that all galaxies that are quenched today went through a phase in which they co-evolved with their host halos, i.e., $\text{sSFR}/\text{sMAR} \sim 1$.

We note that the halo star formation efficiency peaks around progenitors with $M_{\text{vir}} \sim 2 \times 10^{11} M_{\odot}$, which corresponds to galaxies with masses $M_* \sim (0.8 - 3) \times 10^9 M_{\odot}$. Those galaxies have very high values of $\text{sSFR}/\text{sMAR} \sim 6 - 10$. Moreover, these galaxies spent a considerable amount of time having large values of sSFR/sMAR – of the order of few Gyrs. Then, the halo star formation efficiency decreases again for progenitors at $z \sim 0$ with masses below $M_{\text{vir}} \sim 2 \times 10^{11} M_{\odot}$, implying that, at least at $z \sim 0$, the halo mass $M_{\text{vir}} \sim 2 \times 10^{11} M_{\odot}$ is “special”. The fact that in more massive halos the ratio sSFR/sMAR decreases is not surprising, this is supported by both theoretical and observational studies which show that they are more likely to host quenched galaxies, as we discussed above. Note, however, that the ratio sSFR/sMAR is *not* always increasing as the halo mass decreases, contrary to what one might expect by extrapolating the trends below $M_{\text{vir}} \sim 2 \times 10^{11} M_{\odot}$. This may be an indication that galaxy formation in halos with $M_{\text{vir}} \lesssim 2 \times 10^{11} M_{\odot}$ is somewhat different.

Our best fitting models can provide constraints on the functional form for the average star formation histories (SFH) of galaxies. In observational studies, the SFHs are typically assumed to decline exponentially with time, but we find that our results do not support this assump-

tion. Figure 11 shows the SFH for progenitors with $M_{\text{vir}} = 10^{11}, 10^{11.5}, 10^{12}, 10^{13}, 10^{14}$ and $10^{15} M_{\odot}$. Note that the galaxy SFHs are more complex than just a declining exponential model. Note, however, that our results cannot rule out that the SFHs of individual galaxies may be exponentially declining and we emphasise that in this paper we are constraining average SFHs. Here we opted to fit the SFHs to an alternative model. In the left panel of Figure 11 we present the best fitting models when SFHs are based on a lognormal function:

$$\text{SFR}(t) = \frac{A_{\text{SFR}}}{\sqrt{2\pi\tau^2}t} \exp\left[-\frac{(\ln t/t_0)^2}{2\tau^2}\right], \quad (56)$$

where t_0 represents a formation epoch and τ is the width of the function, while the right panel shows the same but when using a delayed- τ model:

$$\text{SFR}(t) = A_{\text{SFR}} \left(\frac{t-t_0}{\tau}\right) \exp\left[-\frac{t-t_0}{\tau}\right], \quad (57)$$

where the parameters t_0 and τ have similar interpretations as above. A motivation for the lognormal model is that Gladders et al. (2013); Abramson et al. (2016); Diemer et al. (2017) noted that the CSFR is well fitted by a lognormal model, suggesting that it could also describe the SFHs of galaxies. The exponentially declining τ model was introduced in pioneer works of galaxy evolution (e.g. Tinsley 1972), who assumed a fixed reservoir of gas that would be gradually exhausted due to in-situ star formation. Finally, the delayed- τ models were considered in more recent observational studies of SFR vs. M_* at different redshifts (e.g., Noeske et al. 2007a). We find the best fit parameters of the above functions by using Powell’s direction set method in multi dimensions (Press et al. 1992) for minimization, using as constraint the values of the SFRs of the progenitors described above. Tables 4 and 5 list respectively the best fitting parameters for a lognormal and delayed- τ SFHs models. Our results show that the delayed- τ model describes reasonably well the SFHs of galaxies in low-mass halos, $M_{\text{vir}} < 10^{12} M_{\odot}$. For halos with masses of $10^{12} M_{\odot}$

Table 4. Best fit parameters for SFHs based on a lognormal model, see Equation (56).

$M_{\text{vir}}(z=0)$	$A_{\text{SFR}} [10^9 M_{\odot}]$	τ	t_0 [Gyrs]
$M_{\text{vir}} = 10^{11} M_{\odot}$	1.247	0.771	11.793
$M_{\text{vir}} = 10^{11.5} M_{\odot}$	12.643	0.404	9.632
$M_{\text{vir}} = 10^{12} M_{\odot}$	56.639	0.354	7.120
$M_{\text{vir}} = 10^{13} M_{\odot}$	177.245	0.383	4.101
$M_{\text{vir}} = 10^{14} M_{\odot}$	435.354	0.538	3.755
$M_{\text{vir}} = 10^{15} M_{\odot}$	577.258	0.584	3.504

Table 5. Best fit parameters for SFHs based on a Delayed- τ model, see Equation (57).

$M_{\text{vir}}(z=0)$	$A_{\text{SFR}} [10^9 M_{\odot}]$	τ [Gyrs]	t_0 [Gyrs]
$M_{\text{vir}} = 10^{11} M_{\odot}$	1.211	6.476	0.708
$M_{\text{vir}} = 10^{11.5} M_{\odot}$	29.978	10.452	0.956
$M_{\text{vir}} = 10^{12} M_{\odot}$	87.837	5.734	0.932
$M_{\text{vir}} = 10^{13} M_{\odot}$	228.725	2.737	0.723
$M_{\text{vir}} = 10^{14} M_{\odot}$	490.11	2.207	0.624
$M_{\text{vir}} = 10^{15} M_{\odot}$	604.758	1.891	0.562

and larger, this model cannot capture the strong decay in SFR after the maximum seen in our results, especially in the most massive halos. The lognormal model describes better the SFRs of galaxies in these halos at intermediate redshifts, but for the most massive halos it is unable to describe the strong SFR decay.

Finally, in Figure 12 we color-code the ratio $R_{\text{SHARC}} \equiv (\frac{\dot{M}_*}{M_{\text{vir}}}) / (\frac{\partial \dot{M}_*}{\partial M_{\text{vir}}})$. In Rodríguez-Puebla et al. (2016b) we showed that, on average, star-forming galaxies must have star-formation rates satisfying $\text{SFR} = \dot{M}_* / (1 - R) = (\frac{\partial \dot{M}_*}{\partial M_{\text{vir}}}) \times \dot{M}_{\text{vir}} / (1 - R)$, which we called stellar-halo accretion rate co-evolution (SHARC), in order to be consistent with the SHMR being nearly redshift independent up to $z \sim 4$. We showed that if this is true galaxy-by-galaxy for most star-forming galaxies, the dispersion of the MAR in the Bolshoi-Planck simulation predicts the observed dispersion in the SFR on the Main Sequence of galaxies. The SHARC assumption is equivalent to $R_{\text{SHARC}} = 1$, and Figure 12 shows that this is a good approximation ($R_{\text{SHARC}} \approx 1$ to 2) for star-forming galaxies (a majority of those below the quenching transition marked by the dashed lines, and a decreasing fraction of those above it).

6.3 Galaxy Mergers

As discussed previously, galaxies can build their masses via in-situ star formation and/or through the accretion of ex-situ stars from other galaxies in mergers. As described in Section 2.2, our model parameterizes the amount of stellar

mass that galaxies formed via in-situ star formation as a function of z , denoted by $f_{\text{in situ}}$. The complement to this function, $f_{\text{ex situ}} = 1 - f_{\text{in situ}}$, is simply the fraction of mass in stars that were accreted via galaxy mergers. The percentage of ex-situ accreted stellar mass is presented in the left Panel of Figure 13 as a function of halo mass and redshift. The instantaneous merger contribution to the stellar mass growth increases with mass at all epochs. For example, at $z \sim 0.1$ the growth of the stellar mass in halos above $M_{\text{vir}} \sim 2 \times 10^{13} M_{\odot}$ is dominated by galaxy mergers. Observe that at $z \sim 0.1$ around $\sim 15\%$ of the stellar mass growth in a Milky-Way sized halo is via mergers, while for smaller halos with $M_{\text{vir}} \sim 10^{11} M_{\odot}$ this fraction is $\sim 2.5\%$. The contribution of galaxy mergers declines strongly with redshift, and at $z \sim 1$ halos around $M_{\text{vir}} \sim 10^{14} M_{\odot}$ are assembling around $\sim 40\%$ of their mass through mergers.

The right Panel of Figure 13 shows the average cumulative fraction of the stellar mass that was formed ex-situ. At $z \sim 0$ the fraction of mass from galaxy mergers is $\sim 36\%$, $\sim 14\%$, $\sim 4\%$, $\sim 2.4\%$ and $\sim 1.8\%$ for halos with $M_{\text{vir}} = 10^{15} M_{\odot}$, $10^{14} M_{\odot}$, $10^{13} M_{\odot}$, $10^{12} M_{\odot}$ and $10^{11} M_{\odot}$, respectively. Note that at $z \sim 1$ the cumulative fraction of stellar mass that was accreted by mergers is $\sim 13\%$ for the progenitor of a $M_{\text{vir}} = 10^{15} M_{\odot}$ halo at $z = 0$, while this is $\sim 3\%$ for the progenitor of a $M_{\text{vir}} = 10^{14} M_{\odot}$ halo. In other words, most of the mass gained via galaxy mergers in high mass halos was from $z \leq 1$. Interesting enough, below $z \sim 1$ high mass halos have little or no star formation. Also, mergers do not appear to be responsible for the increase in the SFR of Milky-Way sized halos that suddenly happened around $z \sim 1$ as we noted in Figure 10. According to Figure 13 most of the mass assembly through mergers happened only very recently; the cumulative fraction was never higher than $\sim 3\%$. Moreover, typical Milky-Way sized halos never experienced a major merger since $z \sim 1$. Thus we conclude that mostly internal process to the galaxy are responsible for this sudden enhanced in SFR.

A relevant question is which type of mergers, either major or minor, are responsible for the ex-situ mass fractions presented above. This question has been studied in a number of previous works (Zheng, Coil & Zehavi 2007; Stewart et al. 2009; Hopkins et al. 2010a,b; Zavala et al. 2012; Avila-Reese, Zavala & Lacerna 2014; Rodríguez-Gomez et al. 2015, 2016). Here, we introduce a simple model to study the impact of galaxy mergers as a function of mass and time. For this model, we use the results of halo merger rates as measured from N -body high resolution simulations convolved through the evolution of the SHMR. Before continuing the description of our model, it is important to realize that not all the merged satellite's stars may necessarily end up in the central galaxy. This is because 1) some fraction of stars can be ejected from the halo if their escape velocities are large enough and, 2) due to the disruption of satellite galaxies, i.e., those that do not merge with the central galaxy but are instead tidally destroyed inside the halo. As a result, some central galaxies, especially the most massive ones, will be surrounded by a diffuse stellar structure. In the literature this is typically referred as intra cluster light (ICL). Note that even with the most modern instruments in telescopes, this diffuse stellar structure is very challenging to observe and typically this is not counted as part of the mass of the central galaxy. In our model, we use the subhalo destruction

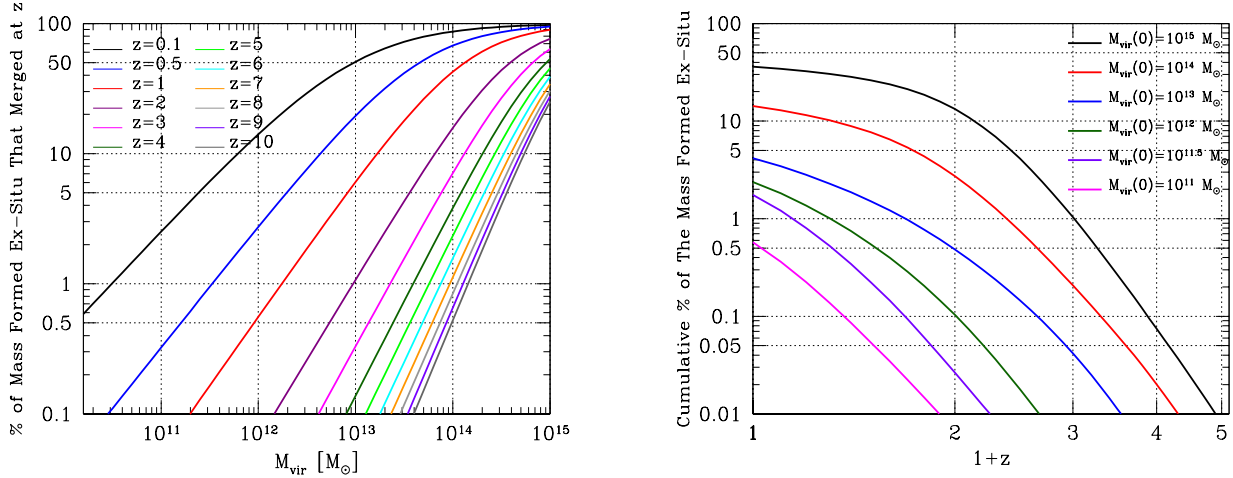


Figure 13. Left Panel: Instantaneous fraction of mass that formed ex-situ and was accreted by galaxy mergers as a function of the halo mass at redshift $z = 0$. **Right Panel:** Cumulative fraction of mass that formed ex-situ and accreted through galaxy mergers. Note that $\sim 40\%$ of the final mass in host galaxies of halos with $M_{\text{vir}}(0) = 1 \times 10^{15}$ was accreted by galaxy mergers.

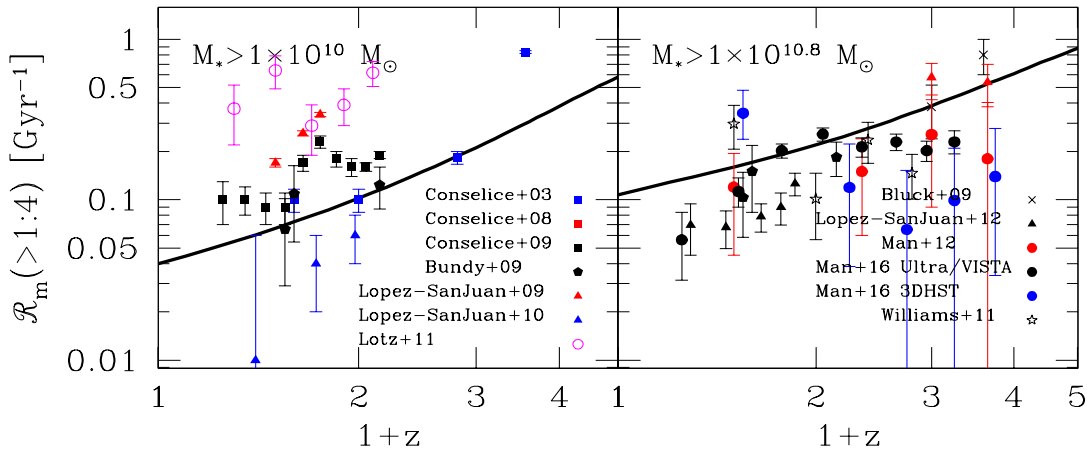


Figure 14. Left Panel: Galaxy major merger rate for galaxies with masses above $1 \times 10^{10} M_{\odot}$. Solid lines show the predictions based on our new SHMR while the different symbols show observational estimates from Conselice et al. (2003); Conselice, Rajgor & Myers (2008); Conselice, Yang & Bluck (2009); López-Sanjuan et al. (2009) and López-Sanjuan et al. (2010) based on galaxy asymmetries while Bundy et al. (2009) gives the merger rate fraction from galaxy pairs. **Right Panel:** Similarly above but for galaxies with masses above $1 \times 10^{10.8} M_{\odot}$. Symbols show data from Bluck et al. (2009) using galaxy asymmetries, López-Sanjuan et al. (2012); Man et al. (2012); Man, Zirm & Toft (2016), Williams, Quadri & Franx (2011) based on galaxy pairs and Lotz et al. (2011) using the data from Lotz et al. (2008) based on the $G - M_{20}$ identification technique.

rate to define the galaxy merger rate. Measuring the disruption rate in simulations is not trivial as the measurements will depend on the definition and on subhalo completeness. Normally, disruption is defined when subhalos lose a significant amount of their original mass at the infall.⁸ Thus there are two scenarios in which subhalos are counted as disruptions, either by being destroyed into the halo at some radii or merged with the central galaxy of the halo. This could

⁸ For example Stewart et al. (2009), define a merger when a subhalo loses 90% of its mass at accretion.

lead to a potential conflict when interpreting galaxy mergers through the subhalo destruction rate. The reason is that in cases in which the subhalo destruction happens at large radius it would lead to an overestimation of the galaxy merger rate since it will take some time for the host satellite to merge with the central galaxy; indeed, for some cases this time could be larger than the Hubble time. Note, however, that we are not taking into account the “true” time that it would take the host satellite to merge with the central galaxy. Therefore, when comparing our predicted merger rate with observations one should keep in mind that these

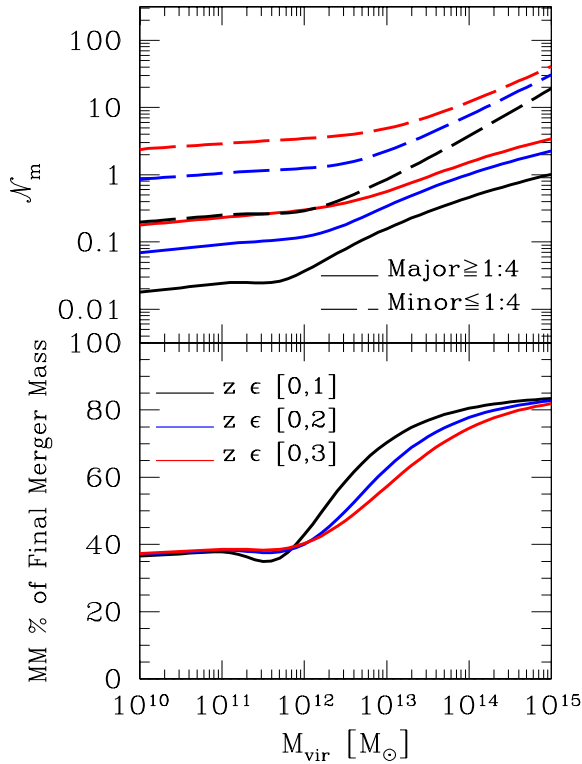


Figure 15. Upper Panel: Number of major ($\mu_* \geq 1/4$, solid lines) and minor ($\mu_* \leq 1/4$, dashed lines) mergers as a function of halo mass since $z = 1, 2$ and 3 as indicated by the labels. **Bottom Panel:** Fraction of final mass acquired through galaxy major mergers since $z = 1, 2$ and 3 . While minor mergers are more frequent in massive galaxies, most of their accreted mass was acquired by major mergers.

results could represent an upper limit to the true merger rates of galaxies. Nevertheless, as shown by Wetzel & White (2010) the disruption of subhalos occurs mainly in the inner regions of the halo where the tidal forces are strongest, while only a small fraction are disrupted at larger radii.

We calculate galaxy mergers by convolving subhalo disruption rates with the evolution of the SHMRs:

$$\frac{d\mathcal{R}_m}{d\log \mu_*}(\mu_*|M_{\text{vir}}, z) = \int P(\mu_*|M_{\text{peak}}, z) \times \frac{d\mathcal{R}_m}{d\log \mu_{\text{peak}}}(\mu_{\text{peak}}|M_{\text{vir}}, z) \times d\log \mu_{\text{peak}}, \quad (58)$$

where $d\mathcal{R}_m/d\log \mu_{\text{peak}}$ is the disruption rate per host halo per logarithmic interval in subhalo peak mass to primary halo mass and per unit of redshift. We use the fitted relation from Behroozi, Wechsler & Conroy (2013b). The distribution $P(\mu_*|M_{\text{peak}}, z)$ is given by Equation 10 where μ_* is the observed satellite-to-central galaxy stellar mass ratio in a halo of mass M_{vir} . Note that the above distribution includes uncertainties due to random errors from stellar masses in addition to the intrinsic scatter of the SHMR.

Figure 14 shows the galaxy major merger rates calculated using our SHMRs and compared to observations. In order to compare directly to our model predictions, we compiled estimations of galaxy major merger from the literature

based on stellar mass thresholds samples. The mass thresholds indicated in the upper part of both panels reflect the fact that we adjusted stellar masses to a Chabrier IMF. Observational reports from close pairs as well as from measurements using asymmetric features in galaxies are plotted in Figure 14. We also adjusted galaxy merger rates by using the cosmologically averaged observability timescales from Lotz et al. (2011). All samples were selected to have major mergers defined as $\mu_* \geq 1/4$.

In general, observations are consistent with our results especially for lower mass galaxies. This is encouraging given the uncertainties both in observations and for our model predictions. Thus, we can conclude that *our SHMR constrained by our semi-empirical modelling in combination with subhalo merger rates is roughly able to account for observed galaxy merger rates*. The possible disagreement at large masses might just be reflecting the fact that our definition of galaxy mergers is related to the disruption rate of subhalos rather than the “true” central mergers. Recall that we did not take into account the dynamical friction time for galaxies in subhalos that were destroyed at larger radius inside of the host halo. Since this time is directly proportional to the virial circular velocity of the host halo, one expects that the overestimation in the merger rate will be larger for the more massive halos. This leaves a window for decreasing the merger rate from abundance matching but still being consistent with the data, and thus leaves some room to improve the study of mergers using our empirical model.

The number of mergers experienced by the progenitors described above from $z = 0$ to $z = 1, 2$ and 3 are presented in the upper panel of Figure 15. The solid lines indicate the major mergers, $\mu_* \geq 1/4$, while dashed lines are for the minor mergers, $\mu_* \leq 1/4$. The black, blue and red colors are for all the mergers that happened since $z = 1, z = 2$ and $z = 3$, respectively. The number of mergers is given by integrating the merger rate over the assembly history of the progenitor

$$\mathcal{N}_m(> \mu_*|M_{\text{vir},0}, z_0) = \int_{\mu_*}^1 \int_{z_0}^z \frac{d\mathcal{R}_m}{d\log \mu_*}(\mu_*|M_{\text{vir}}(z|z_0), z) dz d\log \mu_*. \quad (59)$$

Figure 15 shows that minor mergers happened at least an order of magnitude more frequently than major mergers. Galaxies in halos with present day masses $M_{\text{vir}} = 10^{15}M_{\odot}$ experienced, on average, ~ 5 , ~ 3 , and ~ 1.5 major mergers since $z = 3, z = 2$ and $z = 1$. Galaxies in halos with present day masses $M_{\text{vir}} = 10^{14}M_{\odot}$ experienced, on average, ~ 2 , ~ 1.5 and ~ 0.5 major merger since $z = 3, z = 2$ and $z = 1$ while galaxies in halos below $M_{\text{vir}} = 10^{13}M_{\odot}$ probably never had a major merger since $z = 1$ and $z = 2$ but only one major merger since $z = 3$. In contrast, most of the galaxies have suffered at least a minor merger since $z = 2$ and at least a few since $z = 3$, while central galaxies in massive halos had tens of minor mergers.

The fact that minor mergers dominate over major ones is perhaps not surprising given 1) the hierarchical nature of the LCDM cosmological scenario and 2) the fact that the number density of low-mass galaxies is much higher than that of high-mass galaxies means that the chance of having minor mergers is larger. Note, however, that minor mergers do not always contribute significantly to the total stellar

mass assembled by mergers. The bottom panel of Figure 15 demonstrates this. In Milky-Way sized halos the contribution of major mergers is $\sim 35\%$ of the total stellar mass acquired by mergers, while for halos with $M_{\text{vir}} \geq 10^{14} M_{\odot}$ the fraction asymptotes to $\sim 75\%$. There is no doubt that major mergers are an important part of the formation history of the galaxies, and for that reason we will discuss further the above results in a more general context in Section 8.

7 THE AVERAGE STRUCTURAL EVOLUTION OF GALAXIES

The average stellar mass trajectories and star formation histories obtained in the previous sections allow us to explore several implications that can be naturally studied in our framework. Our goal for this section is to study the structural evolution of the galaxies and its relation to the properties derived above, namely, SFRs and galaxy mergers.

Constraining observations that relate galaxy stellar mass to its structural properties are the Sèrsic index n and the effective radius R_{eff} ,⁹ both at $z = 0$ and at higher redshifts (see e.g., Bell et al. 2012; Patel et al. 2013; van der Wel et al. 2012). For a Sèrsic law $r^{1/n}$, the Sèrsic index n is a parameter that controls the slope of the curvature for the radial distribution of light/mass. Observational results based on the SDSS have shown that when fitting the global light distribution to a Sèrsic law $r^{1/n}$ most of the galaxies have indices n between 0.5 and 8 (see e.g., Simard et al. 2011; Meert, Vikram & Bernardi 2015). However, when dividing galaxies into two main classes – e.g., as early- and late-types – the radial distribution of the light/mass is fairly well described with $n = 4$ (de Vaucouleurs 1948) and $n = 1$ (exponential disc) respectively. In this section, we will assume for simplicity that all late-type galaxies are blue/star-forming systems with a Sèrsic index $n = 1$ while all early-type morphologies correspond to red/quiescent galaxies with Sèrsic index $n = 4$. Hereafter, we will use these galaxy classifications interchangeably. While this is an oversimplification of a more complex reality, for our purpose it is accurate enough since the relatively small fraction of galaxies that do not follow the above assumptions is not critical for our conclusions.

We begin by writing the explicit form of the Sèrsic (1963) law $r^{1/n}$:

$$\Sigma(r) = \Sigma_0 \exp \left[-b_n \left(\left(\frac{r}{R_{\text{eff}}} \right)^{1/n} - 1 \right) \right], \quad (60)$$

where Σ_0 is the surface mass density at the effective radius R_{eff} and b_n has a value of $b_1 \approx 1.678$ and $b_4 \approx 7.669$ for $n = 1$ and $n = 4$ respectively. Therefore once n is defined, in order to fully characterize the surface density profile we need to specify the two free parameters Σ_0 and R_{eff} . The mass profile is given by

$$M_*(< r) = 2\pi \Sigma_0 \int_0^r \exp \left[-b_n \left(\left(\frac{r}{R_{\text{eff}}} \right)^{1/n} - 1 \right) \right] r dr. \quad (61)$$

Notice that when $r \rightarrow \infty$ the total stellar mass M_* becomes a function of Σ_0 and of R_{eff} , $M_* = 2\pi \Sigma_0 F_n(R_{\text{eff}})$.

⁹ The effective radius is defined as the radius that encloses half the luminosity or stellar mass of the galaxy.

The sizes of the galaxies are known to correlate with their total stellar masses. This correlation has been observed to be shallower for late-type morphologies than for more early-type ones, not only at $z \sim 0.1$ (see e.g. Shen et al. 2003) but also at higher redshifts (see e.g. van der Wel et al. 2014). Technically, if we introduce a relation between R_{eff} and M_* , $R_{\text{eff}} = R_{\text{eff}}(M_*, z)$, then Equation (60) is completely determined and the surface mass density at the effective radius is given by Σ_0 : $\Sigma_0 = M_*/2\pi F_n(R_{\text{eff}}(M_*))$. Note that the same line of reasoning can be applied at any redshift.

As mentioned earlier, our main goal is to study the structural evolution of the galaxies and its relation to the galaxy properties derived in the previous sections, that is, SFRs and galaxy mergers. Moreover, we will use the average stellar mass trajectories constrained above to predict the average trajectories for structural evolution of galaxies. Recall that our results are based on the whole galaxy population and there is not an explicit distinction between different populations, i.e., they only depend on mass. The structure of galaxies at a fixed mass can be different as discussed already in the previous paragraph. But we note that there is a remarkable similarity in the surface density profiles of both early- and late-type galaxies when their profiles are rescaled to a fixed fraction of their virial radii, at least at low redshifts (Kravtsov 2013; Somerville et al. 2017). Here we adopt a more probabilistic description by considering the contribution of these two populations to the average, that is, we will compute the stellar mass surface density by averaging over the two main populations—i.e. the early- and late-types, or equivalently quenched and star-forming galaxies—and thus obtain average density profiles that depend only on M_* and z . This procedure can be imagined as stacking all the density profiles of galaxies in a given mass bin, no matter whether they are spheroids or disks or a combination of both (for a recent and similar idea see (Hill et al. 2017)). The average radial distribution of galaxies with total stellar mass M_* is then given by

$$\Sigma(r, M_*) = f_{\text{SF}}(M_*) \Sigma_{\text{SF}}(r, M_*) + f_{\text{Q}}(M_*) \Sigma_{\text{Q}}(r, M_*), \quad (62)$$

where for simplicity we have omitted the dependence on z . The fraction of blue/star-forming and red/quenched galaxies was discussed in Section 4.4. Additionally, recall that for blue/star-forming galaxies we assume $n = 1$ and for red/quenched galaxies $n = 4$. For galaxy sizes we adopt the $R_{\text{eff}} - M_*$ relations derived in Mosleh, Williams & Franx (2013) for nearby, $z \sim 0.015$, blue and red galaxies. They constructed a sample based on the MPA-JHU SDSS DR7 by selecting spectroscopic galaxies with a surface brightness limit of $\mu_{50,r} \leq 23 \text{ mag arcsec}^{-2}$. These authors computed the half-light radius of galaxies by measuring directly the radius at which the flux reaches half of its total value. Their reported effective radii are circularized. In order to use a model to higher redshifts, we use the following redshift dependence for blue/star-forming galaxies:

$$R_{\text{eff,SF}}(z, M_*) = R_{\text{eff,SF}}(0, M_*) \left(\frac{H(z)}{H(0)} \right)^{-0.5}, \quad (63)$$

while for red/quenched galaxies we use

$$R_{\text{eff,Q}}(z, M_*) = R_{\text{eff,Q}}(0, M_*) \left(\frac{H(z)}{H(0)} \right)^{-0.85}. \quad (64)$$

Here $R_{\text{eff,SF}}(0, M_*)$ and $R_{\text{eff,Q}}(0, M_*)$ are the local relations

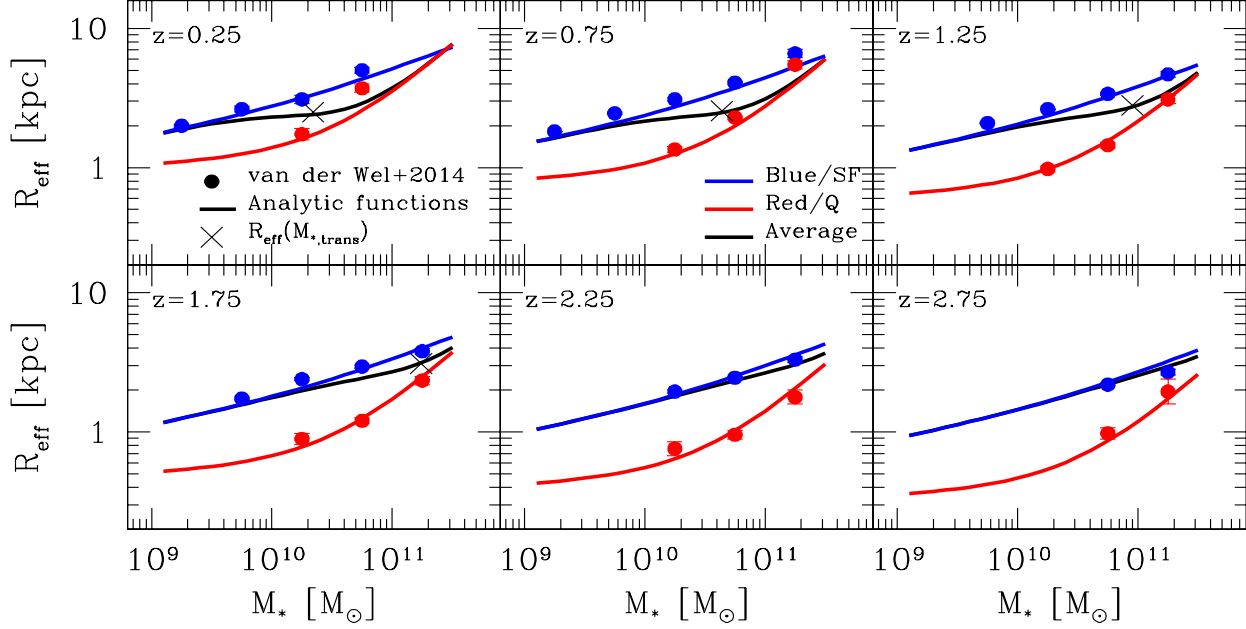


Figure 16. Circularized effective radius for blue star-forming galaxies and red quiescent galaxies for six different redshift bins. The filled circles show the circularized effective radius as a function of stellar mass and redshift from van der Wel et al. (2014) based on multiwavelength photometry from the 3D-HST survey and HST/WFC3 imaging from CANDELS. Solid lines show the redshift dependence for blue and red galaxies of the local relation by Moseleh, Williams & Franx (2013) based on the MPA-JHU SDSS DR7. The black solid lines show the average circularized effective radius as a function of stellar mass. The crosses show the effective radius at M_{50} , i.e., the stellar mass at which the observed star-forming fraction of galaxies is equal to the quenched fraction of galaxies. Note that the effective radius at M_{50} evolves very little with redshift and is ~ 3 kpc. We utilize the plotted redshift dependences as an input to derive the average galaxy’s radial mass distribution as a function of stellar mass by assuming that blue/star-forming galaxies have a Sersic index $n = 1$ while red/quenched galaxies have a Sersic index $n = 4$ (see text for details).

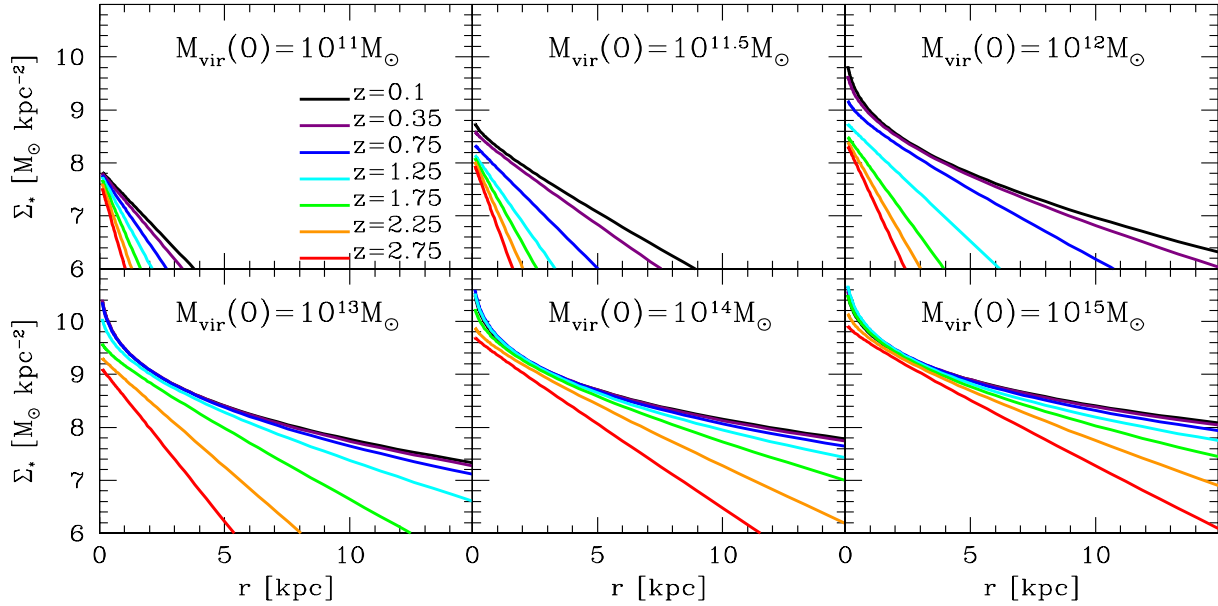


Figure 17. Average evolution of the radial distribution of stellar mass for galaxies in halo progenitors with $M_{\text{vir}} = 10^{11}, 10^{11.5}, 10^{12}, 10^{13}, 10^{14}$ and $10^{15} M_{\odot}$ at $z = 0$. These radial distributions can be imagined as stacking all the density profiles of galaxies at a given virial mass and z , no matter whether galaxies are spheroids or disks or a combination of both.

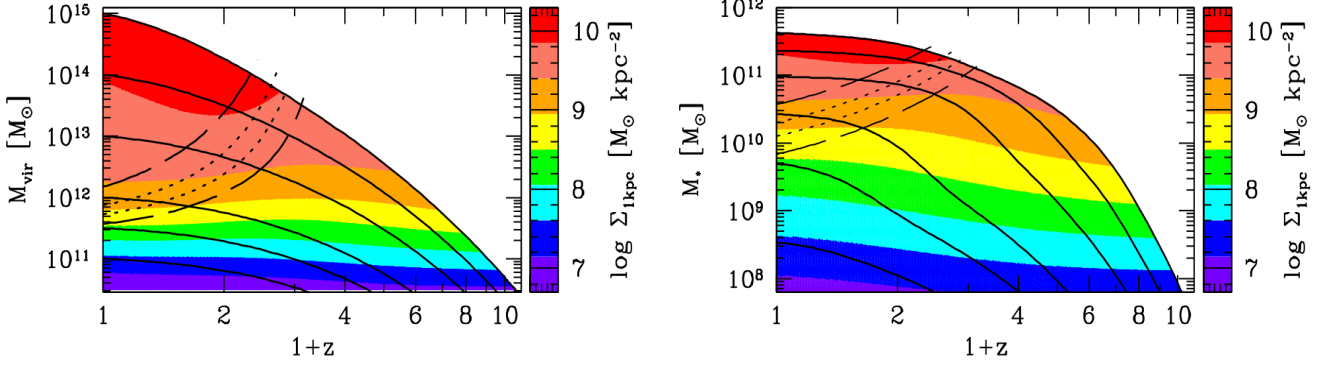


Figure 18. Integrated mass density at 1 kpc, as a function of halo mass (left panel) and stellar mass (right panel) for halo progenitors. The black solid lines show the trajectories for progenitors with $M_{\text{vir}} = 10^{11}, 10^{11.5}, 10^{12}, 10^{13}, 10^{14}$ and $10^{15} M_{\odot}$ at $z = 0$. The short-dashed curves show the stellar mass and halo mass at which the observed fraction of star-forming galaxies is equal to the quenched fraction of galaxies, and the upper (lower) long-dash curves show the stellar mass vs. z where 75% (25%) of the galaxies are quenched.

derived in Mosleh, Williams & Franx (2013) and $H(z)$ is the redshift dependence of the Hubble parameter. We choose these redshift dependencies since, as can be seen in Figure 16, they are consistent with the size-mass evolution observed by van der Wel et al. (2014), which constrained the redshift evolution of galaxy sizes up to redshift $z = 3$ by using multiwavelength photometry from the 3D-HST survey (Brammer et al. 2012) and HST/WFC3 imaging from CANDELS (Grogin et al. 2011; Koekemoer et al. 2011). Figure 16 compares our adopted redshift dependencies with the circularized half-light radius from van der Wel et al. (2014). More recently, Allen et al. (2016) determined the $R_{\text{eff}} - M_{*}$ relation of star-forming galaxies from $z \sim 1$ to $z \sim 7$ by using the ZFOURGE survey cross-matched with CANDELS and the HST/F160W imaging. Their results agree with those of van der Wel et al. (2014), and for $z > 3$ we note that their size-mass relation is consistent with our implied relation.

Our goal is to empirically study the impact of the structural properties in the evolution of galaxies. We will do so by inferring the average trajectories for the density profiles of galaxies in halos of a given mass. Consider the trajectory of a halo with final mass $M_{\text{vir},0}$ hosting a galaxy with final total stellar mass $M_{*,0}$ at the redshift of observation z_0 : $M_{*}(z|M_{*,0}, z_0) = M_{*}(z|M_{\text{vir},0}, z_0)$. Next, we use this relation to describe the mean structural evolution of galaxies as

$$\Sigma(r, z|z_0) = \Sigma(r, M_{*}(z|M_{*,0}, z_0)). \quad (65)$$

7.1 Surface Mass Density and Size Evolution

Figure 17 shows the evolution of the radial stellar mass density for galaxies in different halo progenitors at $z = 0$: $M_{\text{vir}} = 10^{11}, 10^{11.5}, 10^{12}, 10^{13}, 10^{14}$ and $10^{15} M_{\odot}$. This figure shows that, in general, galaxies form from the *inside out*. At high redshifts, most of the galaxies have Sèrsic index $n = 1$, as expected, and most of the low mass galaxies at $z \sim 0$ are still $n = 1$, while for more massive galaxies, the contribution of the $n = 4$ component increases as z decreases. In the most massive halos, the stellar mass within ~ 4 kpc was already in place since $z \sim 1.25$ for the $M_{\text{vir}} = 10^{13} M_{\odot}$

trajectory, and since $z \sim 2.5$ for the $M_{\text{vir}} = 10^{15} M_{\odot}$ trajectory. Notice that Figure 10 shows that the star formation efficiency in a progenitor with $M_{\text{vir}} = 10^{13} M_{\odot}$ at $z = 0$ is $\text{sSFR}/\text{sSMAR} \sim 1$ at $z \sim 1$. Recall that galaxies with star formation efficiencies below ~ 1 are predominately quenched systems, see Section 6.2. Similarly, for halo progenitors with $M_{\text{vir}} = 10^{15} M_{\odot}$ we find that $\text{sSFR}/\text{sSMAR} \sim 1$ at $z \sim 2.5$, suggesting that the structural evolution of galaxies is playing a role in quenching the galaxies (Kauffmann et al. 2003b; van Dokkum et al. 2010; Bell et al. 2012; Cheung et al. 2012; Patel et al. 2013; van Dokkum et al. 2014; Barro et al. 2013, 2015; van Dokkum et al. 2015b). The qualitative behaviour described above is consistent with previous studies of the structural evolution for progenitors of massive galaxies at $z \sim 0$ by selecting galaxies at a constant number density (see e.g., van Dokkum et al. 2010, 2013; Patel et al. 2013).

An alternative way to study the role of the structural properties of the galaxies is the integrated mass density at some inner radius. Based on a sample from the DEEP2/AEGIS survey at $z \sim 0.65$, Cheung et al. (2012) showed that the integrated stellar mass density within 1 kpc, Σ_1 , shows a tight correlation with color, more than any other structural parameter, e.g., Sèrsic index, effective surface brightness, etc. This was later confirmed in Fang et al. (2013, see also Bell et al. 2012) based on a much larger sample using the SDSS DR7.

The left panel of Figure 18 shows the trajectories for halos with $M_{\text{vir}} = 10^{11}, 10^{11.5}, 10^{12}, 10^{13}, 10^{14}$ and $10^{15} M_{\odot}$ at $z = 0$ and the color code shows the corresponding integrated mass density at 1 kpc: $\Sigma_1 = M_{*}(< r_1)/\pi r_1^2$ with $r_1 = 1$ kpc. The right panel of Figure 18 shows the same but as a function of stellar mass. The short dashed lines show the empirical $M_{50}(z)$ above which most galaxies are quiescent. An interesting feature is revealed in this figure. Note that the values of Σ_1 are nearly constant as a function of both halo and stellar mass. Since, on average, galaxies and their host halos are growing at all times, this implies that the values of Σ_1 significantly increase with time as galaxies evolve. This directly implies that there is not a universal threshold value for Σ_1 at which galaxies are more likely to be quiescent, instead this threshold increases with z . As seen

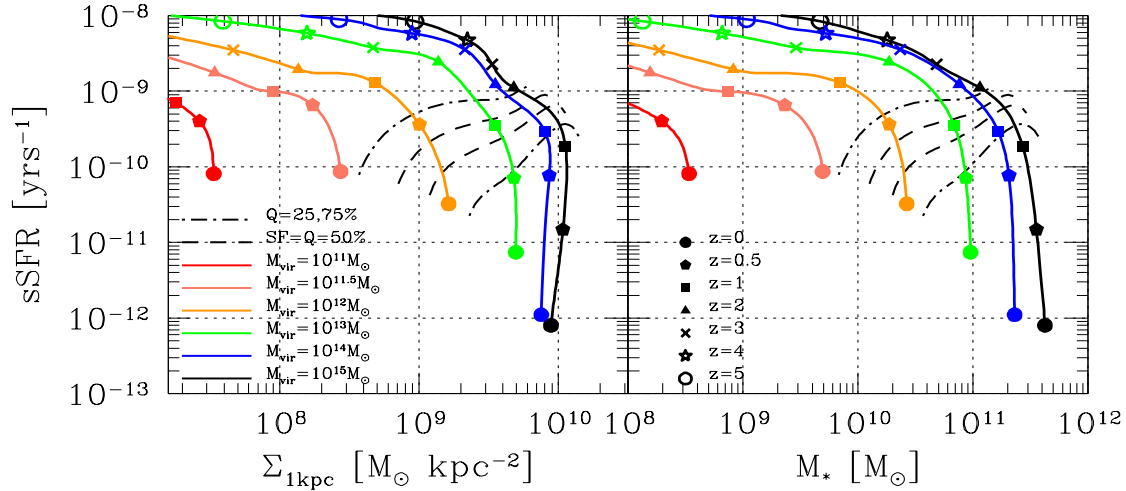


Figure 19. Left Panel: Trajectories for progenitors of halos with $M_{\text{vir}} = 10^{11}, 10^{11.5}, 10^{12}, 10^{13}, 10^{14}$ and $10^{15} M_{\odot}$ at $z = 0$ in the Σ_1 -sSFR plane. **Right Panel:** Same progenitors but in the M_* -sSFR plane. The symbols show different redshifts as indicated by the labels. The dashed curves show $M_{50}(z)$ below which half the galaxies are quiescent, and the upper (lower) dot-dashed curves show where 25% (75%) of the galaxies are quenched.

in Figure 18, at $z \sim 0$ the threshold is around $\Sigma_1 \approx 10^9 M_{\odot} \text{kpc}^{-2}$ while at $z \sim 2$ it is an order of magnitude higher, i.e., $\Sigma_1 \approx 10^{10} M_{\odot} \text{kpc}^{-2}$. This is consistent with Figure 2 in Barro et al. (2015) where the value of Σ_1 above which the galaxy population becomes dominated by quiescent galaxies also increases with redshift.

It is instructive to analyze what would be the consequences of a constant threshold value for Σ_1 . Figure 4 from Fang et al. (2013, see also van Dokkum et al. 2014) shows that the value of $\Sigma_1 \sim 10^{9.5} M_{\odot} \text{kpc}^2$ marks the transition above which the majority of the galaxies are quiescent at $z \sim 0$. Adopting this value, we would conclude that the halo mass transition above which the star formation becomes more inefficient is around $M_{\text{vir}} \sim 10^{12} M_{\odot}$ at all redshifts. As discussed earlier in this paper, this is the expected mass above which virial shocks become more efficient. Therefore, our finding that the threshold value for Σ_1 (and for M_{vir}) increases with z suggests that at high redshifts other mechanisms should be in play for keeping the SFR high in halos above $M_{\text{vir}} \sim 10^{12} M_{\odot}$. Moreover, according to our results these mechanisms were so efficient in the centres of the galaxies that they had a chance to increase their central stellar densities significantly before being quenched compared to their low redshift counterparts. If those mechanisms are not as relevant today as they were at higher redshifts, then one possibility is that virial shocks are the main mechanism to quench galaxies today. We will come back to this in Section 8.

The left panel of Figure 19 shows the trajectories in the Σ_1 -sSFR plane for progenitors with $M_{\text{vir}} = 10^{11}, 10^{11.5}, 10^{12}, 10^{13}, 10^{14}$, and $10^{15} M_{\odot}$ at $z = 0$ while the right panel shows the same but in the M_* -sSFR plane. The different symbols in the figure indicate the redshifts and the dashed lines show $M_{50}(z)$ below which galaxies are quiescent. Interesting conclusions can be obtained from this figure: *i*) There is a tight correlation between the sSFR and Σ_1 , in

other words, Σ_1 is an indicator of the global SFR of the galaxy. Similarly to Figure 18, *ii*) this figure shows that once a galaxy reaches a maximum mass density at 1 kpc, Σ_1 , the SFR is suppressed. This confirms previous studies that the evolution of the structural properties of the galaxies played a key role in the quenching of galaxies (Kauffmann et al. 2003a; van Dokkum et al. 2010; Bell et al. 2012; Cheung et al. 2012; Patel et al. 2013; van Dokkum et al. 2014; Barro et al. 2013, 2015; van Dokkum et al. 2015b).

The left panel of Figure 19 shows some hints of negative stellar mass evolution within 1 kpc: for halos $M_{\text{vir}} = 10^{15} M_{\odot}$ we see Σ_1 evolution of ~ -0.13 dex from $z = 0$ to $z \sim 1$, while for halos $M_{\text{vir}} = 10^{14} M_{\odot}$ we see Σ_1 evolution of ~ -0.06 dex at the same redshift range. van Dokkum et al. (2014) reported similar trends based on the analysis of galaxy sizes from the SDSS, Ultra VISTA and 3D-HST surveys. The authors considered three different scenarios: *i*) central mass loss due to core-core mergers, *ii*) central mass loss due to stellar evolution, and *iii*) adiabatic expansion due to stellar winds (also considered in Damjanov et al. 2009, and referred as the less likely scenario for the mass-size relation). Unfortunately, our analysis is not detailed enough to decide for one over the others. Nonetheless, given the subtlety of this effect we suspect that mass loss due to stellar evolution (and the associated stellar winds) is the most likely explanation, although more work is needed on this.

The upper left panel in Figure 20 shows the trajectories for the halo progenitors discussed above in the size-mass relation. Note first that star-forming galaxies evolved in parallel tracks in the size-mass relation. The second thing to note is that the progenitors at $z = 0$ of quenched galaxies evolved along two very different trajectories. When star formation was the dominant mode of evolution for progenitors of quenched galaxies at $z = 0$, they evolved in a trajectories with a slope of ~ 0.35 . This situation changed dramatically when star formation was suppressed: the slope of the

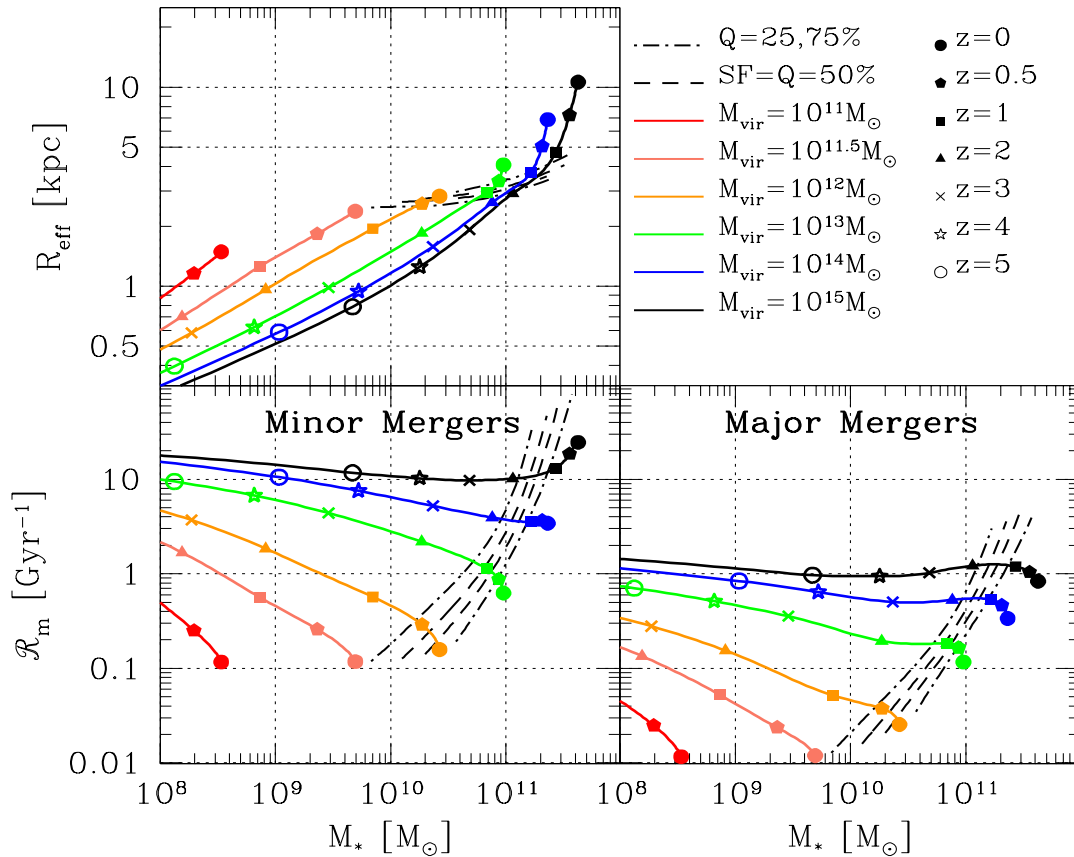


Figure 20. Trajectories for progenitors of halos with $M_{\text{vir}} = 10^{11}, 10^{11.5}, 10^{12}, 10^{13}, 10^{14}$ and $10^{15} M_{\odot}$ at $z = 0$ in the size-mass relation (upper left panel) and for the minor (bottom left) and major (bottom right) merger rates. As in Figure 19, the symbols show different redshifts as indicated by the labels. The dashed lines show $M_{50}(z)$ below which most galaxies are quenched, and the upper (lower) dot-dashed curves show where 25% (75%) of the galaxies are quenched. Progenitors of quenched galaxies went through two phases, initially they grew in parallel trajectories as star formers in the size-mass relation, but after quenching they evolved much faster in size than in mass, resulting in a steeper relation at low z . Presumably the high rate of minor mergers is responsible for this rapid size growth.

trajectory in the size-mass relation now became ~ 2.5 , implying that the most massive galaxies increased their size by a factor of ~ 3 after they quenched. One of the most popular explanations for this upturn in the size-mass relation is dry minor mergers. Indeed, Hilz, Naab & Ostriker (2013) showed that dry minor mergers of diffuse satellites embedded in dark matter halos produced slopes ~ 2 consistent with our findings. In order to investigate this further, we present the merger rate history for the progenitors discussed above in the bottom panels of Figure 20. The left panel plots the merger rate histories from minor mergers, $\mu_* \leq 1/4$, while the right panel is the same but from major mergers, $\mu_* \geq 1/4$.

Similarly to Figures 13 and 14, Figure 20 shows that the merger rate history is dominated by minor mergers. Moreover, in the case of the most massive halos we do observe an upturn in the merger rate approximately at the same epoch when the upturn in the size-mass relation happened due to quenching. Therefore, we conclude that our semi-empirical results are not in conflict with the minor merger hypothesis.

The next thing to note, and perhaps the most surprising, is the fact that galaxies with sizes above $R_{\text{eff}} \sim 3$ kpc are more likely to be quenched, as can be seen by the dashed lines in the upper panel of Figure 20 (and also in Panel f) of Figure 23). Recall that the dashed lines mark the M vs. z above/below which galaxies are likely to be quenched/star-forming. *We believe that the above result does not indicate something fundamental about how galaxies quench, but is just a coincidence.* As we will discuss in Section 8.3, similar trajectories in the size-mass relation have been reported in previous studies (e.g., Patel et al. 2013; van Dokkum et al. 2013). Our findings are not in conflict with those previous empirical results. Figure 16 also shows that galaxies with M_{50} have, on average, effective radius of ~ 3 kpc. This figure shows that at all redshifts and masses, blue/star-forming galaxies have larger R_{eff} than red/quenched galaxies. But note that the black curves in Figure 16, which represent the average effective radii at each stellar mass and redshift, coincide with the red curves for large M_* at low redshifts, where the vast majority of these massive galaxies are quenched.

8 DISCUSSION

The semi-empirical inferences of galaxy mass and structural evolution presented here refer to the average behaviour of the whole galaxy population as a function of halo or stellar mass. While this is clearly a simplification, our results provide relevant clues to constrain the main processes of galaxy evolution and their dependence on galaxy mass. In this Section we will discuss some implications and interpretations of our results. We start by comparing them with some previous works.

8.1 Comparison with Previous Studies

In this Section we compare our SHMR at different redshifts to previous works. We divide our discussion into two main comparisons: those studies that reported stellar mass as function of halo mass, SHMR, and those that have estimated the inverse of this relation, $M_{\text{vir}} - M_*$. The former is typically reported in studies based on statistical approaches, namely indirect methods, as in our case, while the latter is more natural for studies based on direct determinations (e.g., weak gravitational lensing, galaxy clustering). All results were adjusted to a Hubble parameter of $h = 0.678$ and to virial halo masses. When required, we adjusted stellar masses to a Chabrier IMF.

8.1.1 Stellar-to-halo mass relationship

We begin by comparing the mean logarithm of stellar mass ($\langle \log M_* \rangle$) plotted in each $\log M_{\text{vir}}$, (i.e., the SHMR) and shown for seven different redshift bins in Figure 21. Our resulting SHMRs are shown with the solid black lines. The grey areas in all the panels show the ~ 0.3 dex systematic errors.

In Figure 21 we compare our SHMR with Guo et al. (2010, constrained only at $z \sim 0.1$, violet solid line), Behroozi, Wechsler & Conroy (2013b, purple solid lines), and Moster, Naab & White (2013, red solid lines). These authors used subhalo abundance matching to derive the SHMRs. Guo et al. (2010) and Moster, Naab & White (2013) constrained the SHMR using only the GSMF, while Behroozi, Wechsler & Conroy (2013b) included the observed specific SFRs and the CSFR. The dark gray dashed lines with error bars show the SHMR at $z \sim 0.1$ reported in Rodríguez-Puebla, Avila-Reese & Drory (2013) who used the GSMFs for centrals and satellite galaxies as well as the two-point correlation function to constrain their best fit model, their set labeled as C. We also compared the SHMR from Yang et al. (2012) who used the redshift evolution of the GSMF up to $z \sim 4$, the conditional stellar mass function at $z \sim 0.1$ in various halo mass bins, and the galaxy clustering at $z \sim 0.1$ in different mass bins. The cyan and blue shaded areas represent the 1σ confidence level of their results when they used the GSMF reported in Pérez-González et al. (2008) and from Drory et al. (2005), their SMF1 and SMF2 sets respectively. Additionally, we compared the SHMR at $z \sim 0.6$ and at $z \sim 0.9$ from Leauthaud et al. (2012) who combined stacked galaxy-galaxy weak lensing data and galaxy clustering at various mass thresholds from the COSMOS data. Finally, we compared with the SHMR at $z \sim 0.8$ from Coupon et al. (2015) who combined galaxy clustering,

galaxy-galaxy lensing and the stellar mass function from observations in the Canada-France-Hawaii Telescope Lensing Survey (CFHTLenS) and VIPERS field.

We begin our discussion by noting the broad agreement between the various methods compared in Figure 21 for $z \lesssim 1$. This is encouraging due to the different nature of observational constraints for each work plotted. Note that at $z \sim 0.1$ the mass relation of dwarf galaxies (i.e., $M_{\text{vir}} \lesssim 10^{11} M_{\odot}$) becomes slightly shallower (but not as shallow as in Behroozi, Wechsler & Conroy 2013b), something that is not seen in Yang et al. (2012); Moster, Naab & White (2013); and Guo et al. (2010). The redshift evolution of our resulting SHMR is more consistent with the evolution derived in Yang et al. (2012), case SMF1, and Moster, Naab & White (2013). When considering the uncertainties in the constrained relations our SHMR is consistent with those derived in Behroozi, Wechsler & Conroy (2013b).

In the $z > 0.1$ panels of Figure 21 we plot as a dashed curve the time-independent SHMR, i.e., the SHMR obtained at $z \sim 0.1$. Note that below $z \sim 2$ most of the models as well as our mass relations are consistent with a time-independent SHMR. Behroozi, Wechsler & Conroy (2013a) showed that assuming a time-independent SHMR could simply explain the cosmic star formation rate since $z = 4$. In a subsequent work Rodríguez-Puebla et al. (2016b) extended that argument for studying the galaxies in the main sequence of galaxy star formation by showing that the dispersion of the halo mass accretion rates correctly predicts the observed dispersion of star formation rates.

8.1.2 Halo mass-to-stellar mass relationship

Figure 22 shows the mean logarithm of halo mass, ($\langle \log M_{\text{vir}} \rangle$), plotted for each $\log M_*$, i.e., we invert the SHMR to obtain a $M_{\text{vir}} - M_*$ relationship. Because the SHMR has scatter, inverting this relation is not as simple as just inverting the axes of the relation; we also need to take into account the *scatter around the relation*. This can be done by using Bayes' theorem by writing $P(M_{\text{vir}}|M_*, z) = P(M_*|M_{\text{vir}}, z) \times \phi_{\text{vir}}(M_{\text{vir}}, z) / \phi_g(M_*, z)$. Recall that the distribution function $P(M_*|M_{\text{vir}}, z)$ is assumed to be lognormal and in consequence the distribution $P(M_{\text{vir}}|M_*, z)$ is expected to be different from a lognormal distribution. Using the above equation we can thus compute $\langle \log M_{\text{vir}} \rangle$ as a function of $\log M_*$. In the upper left panel of Figure 22 we compare the resulting $\langle \log M_{\text{vir}}(M_*) \rangle$ with the relation $\langle \log M_*(M_{\text{vir}}) \rangle$ at $z = 0.1$. Note that these relations are very different for $M_* \gtrsim 10^{10.6} M_{\odot}$. In general, we observe that the resulting $M_{\text{vir}} - M_*$ relationship evolves in the direction that at a fixed stellar mass, higher stellar mass galaxies tend to have lower halo masses at higher redshifts.

We now compare with recent determinations of the $M_{\text{vir}} - M_*$ relationship. We begin by describing data obtained from galaxy weak lensing analysis. In Figure 22 we plot the results reported in Mandelbaum et al. (2006) from the stacked weak-lensing analysis for the SDSS DR4 at $z \sim 0.1$, black open circles with error bars (95% of confidence intervals). Mandelbaum et al. (2006) reported halo masses separately for late- and early-type galaxies. Here we estimated the average mass relation as: $\langle M_{\text{vir}} \rangle(M_*) = f_l(M_*) \langle M_{\text{vir}} \rangle_l(M_*) + f_e(M_*) \langle M_{\text{vir}} \rangle_e(M_*)$, where $f_e(M_*)$ and $f_l(M_*)$ are the fraction of late- and early-type galaxies in

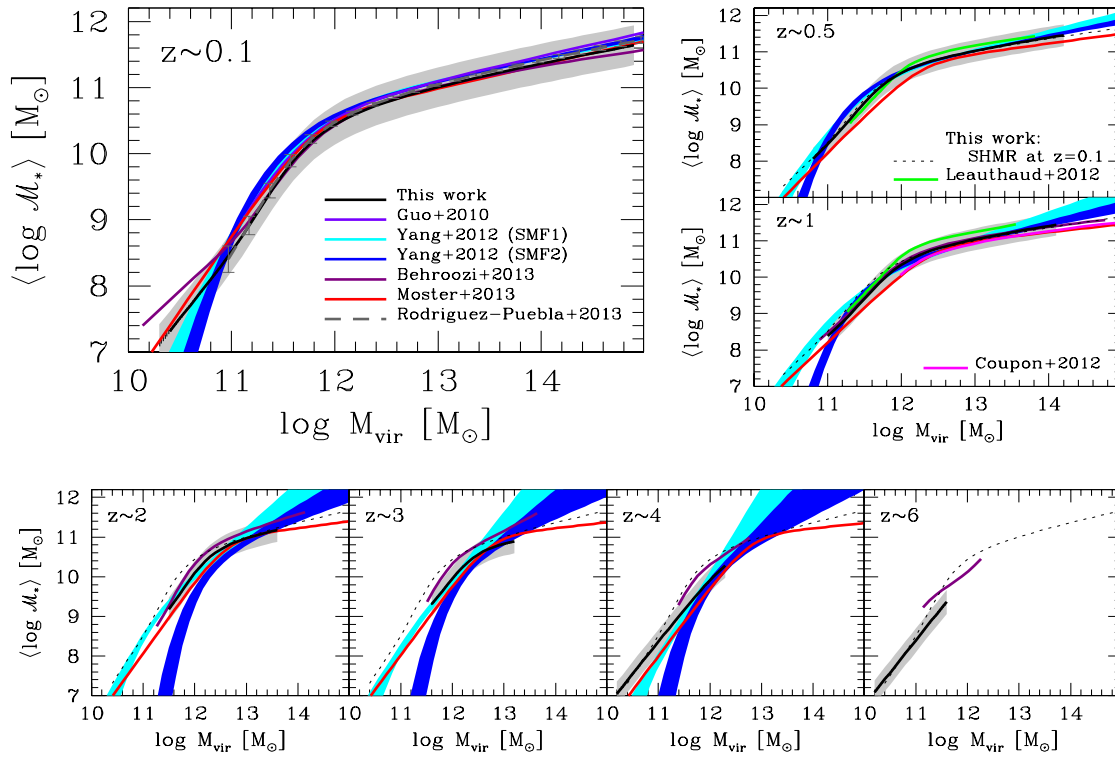


Figure 21. The mean logarithm of stellar mass, $\langle \log \mathcal{M}_* \rangle$, is plotted at each $\log M_{\text{vir}}$ and compared with previous works that reported galaxy stellar masses as a function of halo mass. Our abundance matching results are shown with the solid black curve, and compared with abundance matching results from Guo et al. (2010); Behroozi, Wechsler & Conroy (2013b); and Moster, Naab & White (2013), shown respectively with violet, purple and red solid lines. The dark gray dashed lines show the SHMR at $z \sim 0.1$ reported in Rodríguez-Puebla, Avila-Reese & Drory (2013) who used the GSMFs for centrals and satellite galaxies as well as the two-point correlation function to constrain their best fit model. The results of Yang et al. (2012) based on the evolution of the GSMF, galaxy groups counts, and galaxy clustering are shown with the cyan and blue shaded regions for their SMF1 and SMF2 cases. Constraints from combining the GSMF, galaxy clustering, and galaxy weak lensing from Leauthaud et al. (2012) and Coupon et al. (2015) are shown with the green and magenta lines, respectively. In all the higher redshift panels we plot with short dashed curves our SHMR at $z = 0.1$. The gray shading shows the amplitude of the systematic errors assumed to be 0.3 dex. Note the good agreement at all redshifts between the different techniques except for SMF2, and except for SMF1 for $M_{\text{vir}} \gtrsim 10^{13} M_\odot$.

their sample. The corresponding values of halo masses for late- and early-type galaxies are $\langle M_{\text{vir}} \rangle_l$ and $\langle M_{\text{vir}} \rangle_e$. In this case we assume that $\log \langle M_{\text{vir}} \rangle \sim \langle \log M_{\text{vir}} \rangle$ given that the authors did not report a dispersion around the relation. The empty red squares in the same figure show the analysis from van Uitert et al. (2011) who combined image data from the Red Sequence Cluster Survey (RCS2) and the SDSS DR7 to obtain the halo masses for late- and early-type galaxies as a function of M_* . Similarly to Mandelbaum et al. (2006) data, we also derive their mean halo masses based on their reported fraction of early- and late-type galaxies. We also include the stacked weak-lensing analysis from Velandier et al. (2014) based on the CFHTLenS survey, empty blue triangles. The authors derive halo masses separately for blue and red galaxies based on the color-magnitude diagram. We again derive their mean halo masses by using the reported fraction of blue and red galaxies. Using the CFHTLenS survey Hudson et al. (2013) also derived halo masses as a function of stellar masses for blue and red galaxies separately. We

showed their results with the open blue and red pentagons. Unfortunately, the authors do not report the fraction of blue and red galaxies so we plot their mass relations separately for blue and red galaxies. The green filled square in Figure 22 shows the halo mass derived from galaxy weak lensing at $z \sim 0.8$ from Heymans et al. (2006) by combining the Chandra Deep Field South and the Hubble Space Telescope GEMS survey.

Next, we discuss halo masses obtained from galaxy clustering. Wake et al. (2011) used the halo occupation distribution (HOD) model of galaxy clustering to derive halo masses between $z = 1 - 2$ from the NEWFIRM Medium Band Survey (NMBS), filled blue circles. Similarly, Skibba et al. (2015) used the HOD model and the observed stellar mass dependent clustering of galaxies in the PRIMUS and DEEP2 redshift survey from $z \sim 0.2$ to $z \sim 1.2$ to constrain the $M_{\text{vir}} - M_*$ relationship, indicated by the solid black circles. Martínez-Manso et al. (2015) used the Deep-Field Survey to derive the angular clustering of galaxies and

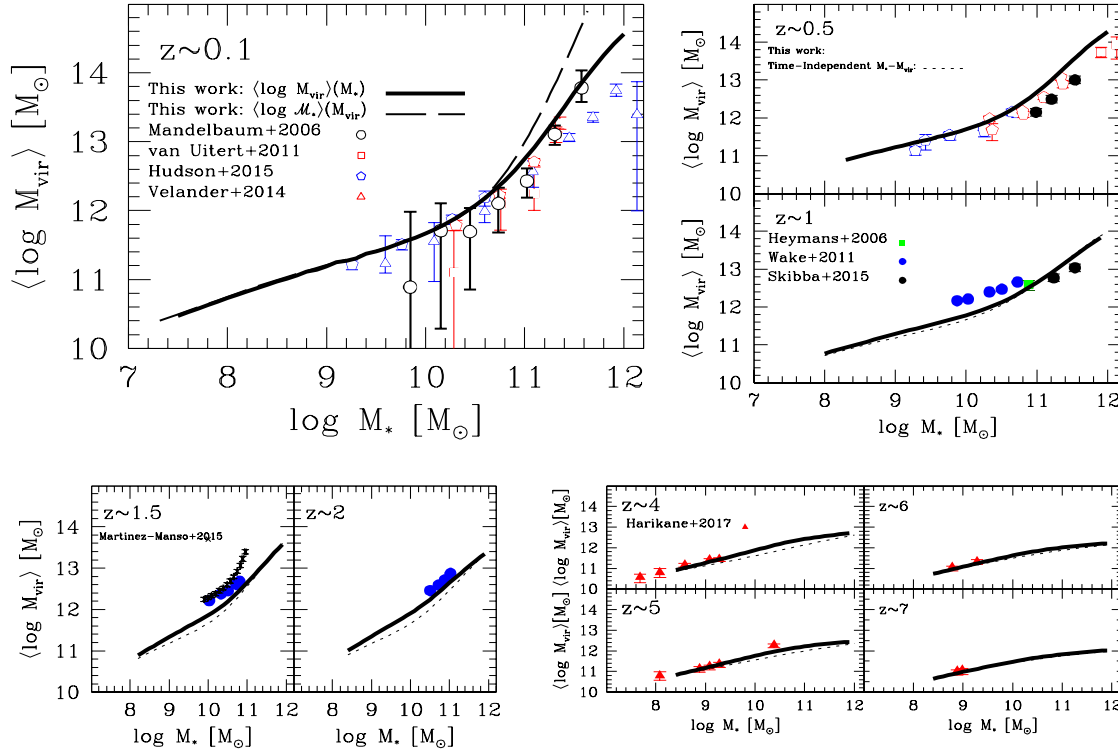


Figure 22. The mean logarithm of halo mass, $\langle \log M_{\text{vir}} \rangle$, is plotted at each $\log M_{*}$ and compared with previous works that reported halo masses as a function of galaxy stellar mass. Weak lensing studies from Mandelbaum et al. (2006); van Uitert et al. (2011); Velander et al. (2014); Hudson et al. (2013) and Heymans et al. (2006) are shown respectively with the black open circles, empty red squares, empty blue triangles, open blue/red pentagons and green filled square. Galaxy clustering from Wake et al. (2011); Skibba et al. (2015), and Harikane et al. (2016) are shown with the filled blue circles, solid black circles and red solid triangles respectively. The dotted line shows a time-independent M_{*} - M_{vir} relation. The relation $\langle \log M_{*}(M_{\text{vir}}) \rangle$ at $z = 0.1$ is shown with a long dashed line. Table 6 lists the parameters for an analytic fit to $\langle \log M_{\text{vir}} \rangle$ given by Equation (66).

obtain halo masses by modelling galaxy clustering in the context of the HOD. Finally, Harikane et al. (2016) estimated the angular distribution of Lyman break galaxies between $z \sim 4-7$ from the Hubble Legacy deep Imaging and the Subaru/Hyper Suprime-Cam data. Halo masses were estimated using the HOD model, filled red triangles in Figure 22.

Similarly to the determinations of the SHMR compared in Figure 21, the $M_{\text{vir}}-M_{*}$ relationships described above agree very well between each other and with our mass relations from abundance matching, specially at $z \lesssim 1$. The short dashed lines show the resulting $\langle \log M_{\text{vir}}(M_{*}) \rangle$ when assuming a time-independent $\langle \log M_{*}(M_{\text{vir}}) \rangle$ relation. Note that the evolution of this relation simply reflects the fact that the ratio $\phi_{\text{vir}}(M_{\text{vir}})/\phi_g(M_{*})$ is not constant with time, that is, $P(M_{\text{vir}}|M_{*}, z) = P(M_{*}|M_{\text{vir}}) \times \phi_{\text{vir}}(M_{\text{vir}}, z)/\phi_g(M_{*}, z)$ where the distribution $P(M_{*}|M_{\text{vir}})$ is independent of time just because $\langle \log M_{\text{vir}}(M_{*}) \rangle$ relation is time-independent. Do not confuse this with a $\langle \log M_{\text{vir}}(M_{*}) \rangle$ relationship that is constant in z , that is, *we are not replicating* the resulting $\langle \log M_{\text{vir}}(M_{*}) \rangle$ at $z = 0.1$ in all the panels. Table 6 lists the best fit parameters when $\langle \log M_{\text{vir}}(M_{*}) \rangle$ is parameterized using the function proposed

in Behroozi, Conroy & Wechsler (2010):

$$\langle \log M_{\text{vir}}(M_{*}) \rangle = \log M_1 + \beta \log \left(\frac{M_{*}}{M_{*,0}} \right) + \frac{\left(\frac{M_{*}}{M_{*,0}} \right)^{\delta}}{1 + \left(\frac{M_{*}}{M_{*,0}} \right)^{-\gamma}} + \frac{1}{2}. \quad (66)$$

The accuracy of the fitting parameters on Table 6 are better than 5% at all redshifts.

Finally, we acknowledge that there are other direct techniques to derive halo masses from galaxy samples. One example is to use the kinematics of satellite galaxies as test particles of the gravitation field of the dark matter halo in which their reside (e.g., Conroy et al. 2007; More et al. 2011; Wojtak & Mamon 2013). In the case of satellite kinematics it has been noted that this method tends to give higher halo masses than other methods (like those described above, see e.g., More et al. 2011; Skibba et al. 2011; Rodríguez-Puebla et al. 2011). Rodríguez-Puebla et al. (2015) argued that the difference with other techniques can be partially explained by the relation between halo mass and the number of satellite galaxies. Given the challenge that would imply to show a

Table 6. Best fit parameters to the $\langle \log M_{\text{vir}}(M_*) \rangle$ relation given by Equation 66. Note that due to the low constraints at high masses for δ and γ we kept them constant above $z > 2$.

z	$\log M_1[M_\odot]$	$\log M_{*,0}[M_\odot]$	β	δ	γ
0.10	12.58	10.90	0.48	0.29	1.52
0.25	12.61	10.93	0.48	0.27	1.46
0.50	12.68	10.99	0.48	0.23	1.39
0.75	12.77	11.08	0.50	0.18	1.33
1.00	12.89	11.19	0.51	0.12	1.27
1.25	13.01	11.31	0.53	0.03	1.22
1.50	13.15	11.47	0.54	-0.10	1.17
1.75	13.33	11.73	0.55	-0.34	1.16
2.00	13.51	12.14	0.55	-0.44	0.92
3.00	14.02	12.73	0.59	-0.44	0.92
4.00	14.97	14.31	0.60	-0.44	0.92
5.00	14.86	14.52	0.58	-0.44	0.92
6.00	17.43	19.69	0.55	-0.44	0.92
7.00	17.27	20.24	0.52	-0.44	0.92

fair comparison between our mass relations and those from satellite kinematics, we prefer to omit that comparison in this paper.

8.2 The Quenching Halo Mass Depends On Redshift

The conception of a transition halo mass above which the star formation becomes strongly inefficient has been introduced by a number of theoretical studies (e.g., White & Frenk 1991; Birnboim & Dekel 2003; Kereš et al. 2005; Dekel & Birnboim 2006; Cattaneo et al. 2007). These studies have shown that a stable virial shock is formed when the virial mass reaches $M_{\text{vir}} \sim 10^{12} M_\odot$, approximately independent of z , through which the cosmological inflowing gas must cross, thus resulting in the heating of the infalling gas (Dekel & Birnboim 2006). In the literature, this mechanism is typically referred as halo mass quenching. Indeed, this seems to apply at $z \sim 0$, where the stellar mass above which the galaxy population is observed to be dominated by quiescent galaxies is $M_* \sim 10^{10.5} M_\odot$, corresponding to a halo mass of $M_{\text{vir}} \sim 10^{12} M_\odot$ (see Figure 6). But as we have discussed starting with Figure 2, M_{50} , the halo mass where 50% of galaxies are quenched, actually depends on redshift. In light of our results, here we discuss this redshift dependence.

Panel a) of Figure 23 shows the average stellar mass growth history for halos with final masses of $M_{\text{vir}} = 10^{11}, 10^{11.5}, 10^{12}, 10^{13}, 10^{14}$, and $10^{15} M_\odot$ at $z = 0$. The gray, cyan, light red, and green shaded areas show the redshift ranges when the progenitors of halos with $M_{\text{vir}} = 10^{15}, 10^{14}, 10^{13}$ and $10^{12} M_\odot$ reached the mass range of $M_{\text{vir}} = 10^{11.8} - 10^{12} M_\odot$. We use a halo mass range instead of a fixed mass given that this transition mass might be not sharp (e.g., Kereš et al. 2005; Dekel & Birnboim 2006). In the same panel, the black short-dashed lines indicate when the observed fraction of star forming galaxies is 50% while the upper and lower long-dashed lines indicate when the fraction of quenched galaxies is 75% and 25%. The corresponding star formation histories for the progenitors described above are presented in Panel b) of the same figure. Simi-

larly to Panel a), the shaded areas show the redshift ranges when the progenitors of halos of masses $10^{12-15} M_\odot$ at $z = 0$ reached the mass range of $M_{\text{vir}} = 10^{11.8} - 10^{12} M_\odot$.

Next, we consider the progenitors of halos at $z = 0$ with masses above $M_{\text{vir}} > 10^{12} M_\odot$. According to Figure 23, we note that, on average, the epoch at which the SFRs of those galaxies declined is *rather different* from the epoch at which their host halo reached the halo mass quenching transition. Moreover, this depends on halo mass. This suggests that galaxy quenching is not driven mainly by halo mass alone and that other mechanisms are playing an important role. Note, however, that the galaxy population in halo progenitors at $z = 0$ with masses $M_{\text{vir}} = 10^{12} M_\odot$ are on the statistical limit of being dominated by quiescent systems. This could also suggest that the mechanisms that are responsible for quenching are complex and that they could be actually somewhat diverse at different redshifts leading to the observed imprint in Figure 2, namely, high stellar mass galaxies tend to quench earlier, which is sometimes referred as quenching downsizing. We will come back to this in the next subsection.

One possibility is that cold streams were able to supply enough gas to sustain the star formation in galaxies in massive halos at high redshifts. That was suggested in a number of previous works showing that hydrodynamical simulations predict that at high redshifts $z > 1$ hot halos can be penetrated by cold streams (see e.g., Nagai & Kravtsov 2003; Kereš et al. 2005; Dekel & Birnboim 2006; Dekel et al. 2009). Indeed, in Figure 10 we showed that the halo mass at which the star formation efficiency sSFR/sMAR drops below unity depends on redshift in the direction that the higher the redshift, the larger the transition halo mass. Interestingly enough, progenitors of Milky-Way mass halos with $M_{\text{vir}} = 10^{12} M_\odot$ at $z = 0$, reached the ratio sSFR/sMAR ~ 1 at $z \sim 0$ and thus are unlikely to still be fed by cold streams, as predicted in the cold stream theory (Dekel & Birnboim 2006).

We thus conclude that our new SHMRs are consistent with the idea that at high redshifts cold streams were able to sustain the star formation in the progenitors of the most massive galaxies observed today. Therefore, mechanisms alternative to halo mass quenching should be invoked to explain the strong decline in the SFR of those progenitors. Additionally, our new SHMRs suggest that virial shock heating might become more relevant at lower redshifts.

8.3 The Role of the Structural Properties of the Galaxies

In Section 7.1, we discussed various structural properties of galaxies and their evolution. Our findings show that galaxies grow in central stellar mass density (within 1 kpc, Σ_1) while they are star forming, and they quench once they reach a maximum Σ_1 . This maximum Σ_1 is higher for higher mass galaxies, and it is reached at higher redshifts, as seen in Figure 23. That is, the progenitors of massive galaxies today have higher Σ_1 and quenched earlier than the progenitors of lower mass galaxies. These results strongly suggest that the quenching of massive galaxies is related to the central density of these galaxies, a mechanism that could be associated with the growth of the central supermassive black hole (SMBH) powering an AGN or quasar. The central density

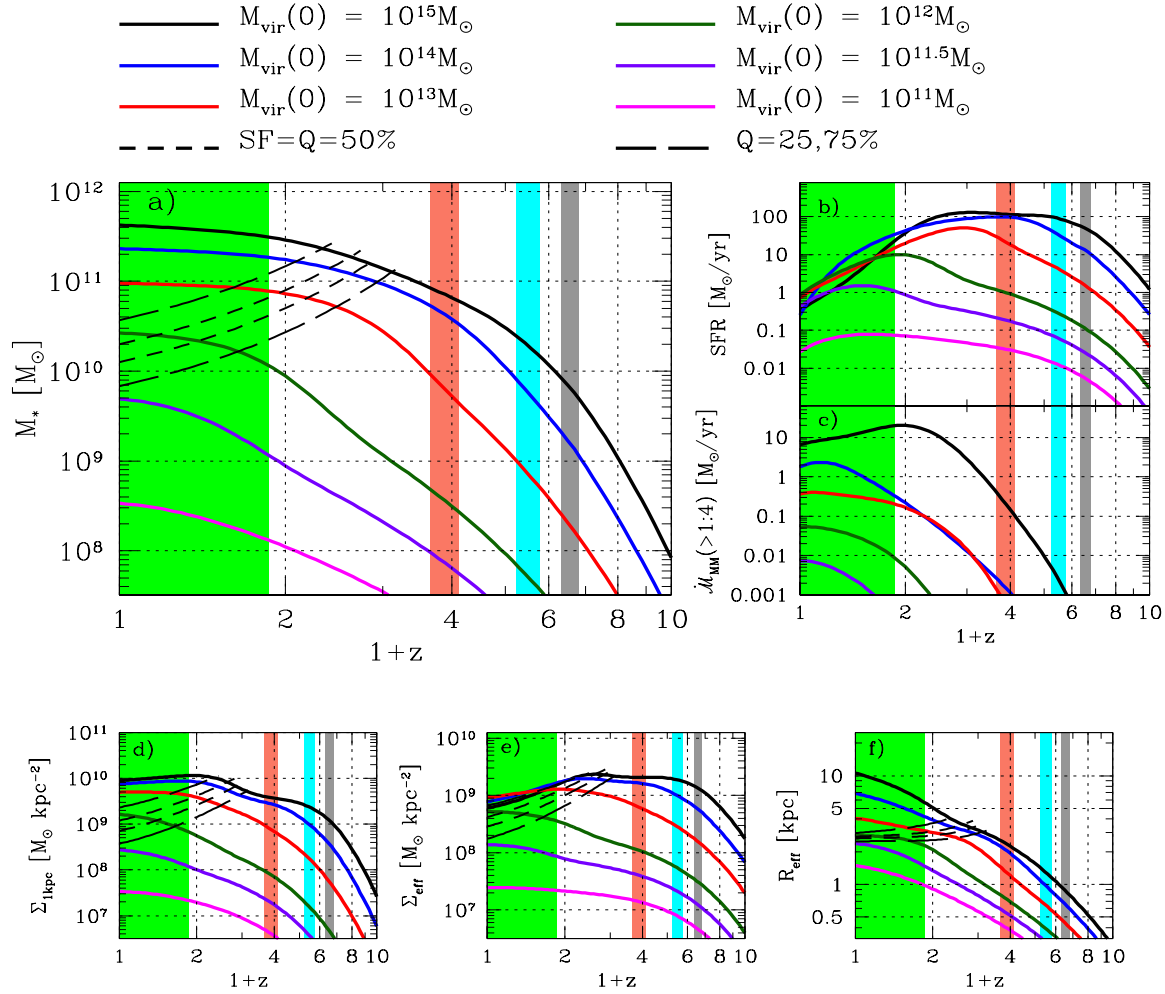


Figure 23. Summary plot for various galaxy properties: Panel a) Stellar mass, Panel b) star formation history, Panel c) Stellar mass accretion from major mergers, Panel d) Integrated surface mass density at 1 kpc, Panel e) Effective surface mass density and Panel f) Effective radius. The magenta, violet, green, red, blue and black lines show the trajectories for progenitors of $M_{\text{vir}} = 10^{11}, 10^{11.5}, 10^{12}, 10^{13}, 10^{14},$ and $10^{15}M_{\odot}$. The gray, cyan, light red and light green shaded areas in all the panels show the epoch range at which the progenitors of halos of $10^{12}, 10^{13}, 10^{14},$ and $10^{15}M_{\odot}$ reached the mass of $M_{\text{vir}} = 10^{11.8} - 10^{12}M_{\odot}$. The short-dashed lines show $M_{50}(z)$ where half the galaxies are statistically quenched, while the fractions of quenched galaxies are 25% (75%) at the upper (lower) long-dashed lines.

and the growth of the black hole should be fundamentally linked, given all the observational evidence that the masses of SMBHs are well correlated with the most internal properties of their host galaxies, particularly with their bulge properties (see e.g. Kormendy & Ho 2013).

Our results are consistent with a scenario in which the progenitors of the most massive galaxies, $M_* \gg 3 \times 10^{10}M_{\odot}$: 1) have a fast growth in mass at high redshifts; 2) cold streams facilitate this growth in mass and central density, in spite of the hot gas halo (see the discussion in the previous subsection); 3) SMBHs grow in their centres along with the increase in central density; 4) the central density and overall galaxy mass growth are slowed down when a luminous AGN is switched on (quenching). In addition, the more massive the system, the higher the central densities (hence more massive SMBHs) must be reached in order to produce AGNs luminous enough to quench the galaxy (e.g., Terrazas

et al. 2016). These are just the trends seen in Figure 23. For lower masses, down to $M_* \sim 3 \times 10^{10}M_{\odot}$, the central densities do not attain very high values, and the AGN is probably not luminous enough to be the main quenching mechanism. Instead, for these galaxies, whose halos attain the quenching transition mass at late epochs (when cold streams are already of low efficiency), the long cooling time of the hot halo gas can be the main mechanism for suppressing star formation.

In Section 7.1, we found that galaxies evolve in parallel tracks in the size-mass relation with slopes around $d \log R_{\text{eff}}/d \log M_* \sim 0.35$, but once they quench they move in the size-mass relation with a steeper slope $d \log R_{\text{eff}}/d \log M_* \sim 2.5$ (which is consistent with the fact that minor dry mergers increase the sizes of early-types galaxies, see Figure 20). This implies that *i*) galaxies are growing in very different regimes, and *ii*) at all times the

sizes are growing, on average, “inside-out”. We note that this transition occurs, statistically, when galaxy’s size is around ~ 3 kpc, see panel f) in Figure 23. However, we do not think that this size reveals something fundamental about their maximum density, Σ_1 . As discussed above, the central density is associated to the SMBH growth, and hence to the luminosity of the AGN that quenches star formation. Thus it may be that the black hole is playing a major role in initiating or maintaining quenching, and the fact that galaxies quench when they reach, on average, an effective radius of ~ 3 kpc may just be a coincidence.

Panels d), e) and f) in Figure 23 show respectively the trajectories of the halo progenitors discussed above for Σ_1 , Σ_{eff} and R_{eff} . Recall that the black dashed lines mark $M_{50}(z)$ above/below which a majority of galaxies are quenched/star forming. Panels d) and f) illustrate the conclusions described above, while the trends shown in panel e) are a direct consequence of the evolution of the size-mass relation. That is, the progenitors of quenched galaxies evolved along two markedly different trajectories: they grew in density as star formers and quenched when they reached a maximum of effective density, and then their density within R_{eff} decreased at low redshift as R_{eff} increased. Note that nothing interesting happened to the structural properties of galaxies when the progenitors of their host halos reached the characteristic quenching halo mass, $M_{\text{vir}} \sim 10^{12} M_{\odot}$. Our findings that galaxies, on average, grew “inside-out” and quenched when they reached a maximum density are in excellent agreement with previous conclusions by Kauffmann et al. (2003a); Franx et al. (2008); Patel et al. (2013); van Dokkum et al. (2014); Barro et al. (2015); and van Dokkum et al. (2015b).

Our findings, unfortunately, cannot be compared directly to the wet (gas inflow) compaction model (Dekel & Burkert 2014; Zolotov et al. 2015; Tacchella et al. 2016). This model asserts that shrinkage of the effective radius arises from central starbursts fed by dissipative processes, driven by violent disc instabilities (Dekel & Burkert 2014), possibly triggered by major or minor mergers (Inoue et al. 2016), that could only happen at higher redshifts when the gas fractions are high. In particular, this model predicts that in the innermost parts of the galaxies gas compaction provides the fuel to increase the central stellar mass density due to in-situ star formation, and when the central gas is entirely depleted the central stellar mass density should remain constant. Nonetheless, we can compare our model indirectly with the wet compaction model by studying the Σ_1 trajectories of the progenitors discussed earlier in this section, see panel d). We find that our results are consistent with the wet compaction model. Finally, as discussed in Section 8.2, it is likely that cold streams can maintain the gas supply in massive galaxies at high redshifts. We note that cold streams and wet compaction are both phenomena that may happen at the same time; indeed, Dekel, Sari & Ceverino (2009) showed that smooth cold streams can keep a gas-rich disc unstable and turbulent at high redshifts. Moreover, the presence of an AGN/QSO is also plausible, especially in massive galaxies. It is not clear how these three phenomena act together, but presumably wet contraction and cold streams may help to feed the AGN, which in turn depletes the gas from the galaxy more efficiently and keeps hot gas from cooling.

8.4 The Impact of Galaxy Mergers

In Section 6.3 we showed that growth in stellar mass is primary due to in-situ star formation. High mass galaxies, $M_* \sim 5 \times 10^{11} M_{\odot}$, assembled around $\sim 36\%$ of their final stellar mass through galaxy mergers, while galaxies in Milky-Way sized halos assembled around 2.4%. Additionally, we found that minor mergers, $\mu_* \leq 1/4$, are more frequent than major mergers, $\mu_* \geq 1/4$, at all masses. For example, massive galaxies with $M_* \sim 5 \times 10^{11} M_{\odot}$ had at least 1 major merger but ~ 20 minor ones since $z \sim 1$. Nonetheless, at these high masses major mergers contributed $\sim 75\%$ of the total mass in mergers while at low masses this was around $\sim 35\%$. Given the predictions presented for galaxy mergers, here we discuss their impact on the formation history of the galaxies, namely, in the context of their star formation histories and structural properties. Panel c) of Figure 23 shows the historical contribution from major mergers to the stellar mass accretion rate for our set of progenitors at $z = 0$, described above. This figure shows that the mass growth due to major mergers peaks below $z \sim 1$, with the redshift location of the peak of the stellar mass growth due to major mergers decreasing with decreasing halo mass. Today galaxies with $M_* \sim 10^{11} M_{\odot}$ are on their peak of stellar mass growth due to major mergers.

While in this paper we focused on stellar mergers, different types of mergers are linked to different phenomena. For example, hydrodynamical simulations of galaxy mergers have shown that the dissipational (wet) mergers result in starburst activity between $\sim 100 - 500$ Myrs while (dry) dissipationless mergers, especially the major ones, will result in disturbances to the morphologies. Of course, both types of mergers happen over the merger history of the galaxies. In general, we do not observe an increase of star formation triggered by major mergers, particularly at high redshifts where the fractions of gas were high, and not even for massive galaxies. Nevertheless, we speculate that the extended period of star formation in massive galaxies can be partly explained by merger-induced starbursts, since the rise of stellar mass accreted due to major mergers in galaxies with $M_* \sim 5 \times 10^{11} M_{\odot}$ occurs mainly during the phase of high star formation, although the main contribution of mergers occurs at low redshift. Probably this extended period of star formation is related to gas fed by cold streams, as discussed above.

We observe that when the progenitors of quenched galaxies start to suppress their SFRs, the stellar mass accretion rate became dominated by major mergers. Galaxy major dry mergers are expected to change morphologies (e.g. Toomre & Toomre 1972; Barnes & Hernquist 1996; Robertson et al. 2006b,a; Burkert et al. 2008). This could imply that the change in morphology of massive galaxies occurred below $z \sim 1$.

Major mergers and black hole growth are thought to be intimately correlated during the AGN phase in massive galaxies, especially at high redshift where the gas fractions were higher. Therefore the fact that the SFR was suppressed when the contribution from major mergers became more important is consistent with AGN feedback from the black hole being an effective quenching mechanism. Looking to Figure 23, it is not obvious that major mergers could trigger an AGN phase in massive galaxies. Nonetheless, our results

do not reject this possibility. To see this, we recapitulate the main results from Figure 15. This Figure shows that the host galaxies in massive halos had ~ 3 major mergers since $z \sim 3$ and had ~ 2 since $z \sim 2$. We thus conclude that our results do not reject the possibility that AGNs were triggered by major mergers.

9 SUMMARY AND CONCLUSIONS

This paper presents new determinations of the stellar-to-halo mass relation, SHMR, over a very broad redshift range, between $z \sim 0$ to $z \sim 10$, from abundance matching. We use the redshift evolution of the SHMR together with the growth of dark matter halos to predict the average in-situ stellar mass growth of galaxies and therefore their star formation histories, as well as the ex-situ mass growth due to mergers. We used as observational constraints the redshift evolution of the galaxy stellar mass function, GSMFs, and the star formation rates, SFRs. In order to get a robust determination of our SHMRs we used a large compilation of GSMFs from the literature as well as of SFRs. We calibrated all the observations to the same basis in order to minimize potential systematic effects that might bias our results. Specifically, all the observations were corrected to the IMF of Chabrier (2003), the Bruzual & Charlot (2003) SPS model, the Calzetti et al. (2000) dust attenuation model, and the cosmological parameters reported by the Planck mission and used in the Bolshoi-Planck simulation. Corrections for surface brightness incompleteness were also introduced.

We report star formation histories for a wide range of halo masses at $z = 0$ and their progenitors at higher redshifts. We quantify both the instantaneous and the cumulative fraction of mass accreted due to mergers. To quantify in more detail which type dominates the accreted mass fraction we use the subhalo disruption rates convolved with the redshift evolution of the SHMR.

Once we have constrained robust trajectories for galaxy progenitors, we present a study of the average evolution of the radial distribution of stellar mass as a function of mass, and explore the impact of the structural properties on the evolution of galaxies. This is the first time that this has been done within the semi-empirical galaxy-halo connection approach. To do this, we used the observed size-mass relation of local galaxies derived in Mosleh, Williams & Franx (2013) and determined the dependence to higher redshifts to be consistent with the size-mass evolution observed by HST van der Wel et al. (2014). Finally, we assumed that the radial distribution of stellar mass is a combination of Sersic $n = 1$ and $n = 4$ profiles, with fractions associated to the population fractions of star-forming and quenched galaxies at each z .

In this paper we do not model the individual growth histories of galaxies, but rather average growth histories. Specifically, we do not know “case by case” how galaxies suppressed their star formation. Instead we adopt a more probabilistic description by inferring which were the most likely trajectories of the galaxy progenitors as a function of mass and redshift.

Finally, we list our main results and conclusions:

- The stellar-to-halo mass relation (SHMR) evolves very slowly below $z \sim 1$ but has a noticeable evolution between

redshift $z \sim 1$ and $z \sim 7$. This statement is mass dependent: the high mass end evolves more strongly than the low mass end. This implies that the value of the peak stellar-to-halo mass ratio decreased approximately a factor of ~ 3 between $z \sim 0.1$ and $z \sim 4$, and almost an order of magnitude at $z \sim 10$.

- When comparing indirect methods for constraining the galaxy halo-mass-to-stellar-mass connection (where the halo masses are determined by abundance matching), we find a broad agreement. This is encouraging given the very diverse nature of the methods that have been employed in the literature. Similar conclusions were drawn when comparing instead direct methods aimed at constraining the galaxy stellar-mass-to-halo-mass connection (where the halo masses are determined by gravitational lensing or clustering),

- The star formation histories for the progenitors of today’s massive elliptical galaxies in Figure 9 show that they reached an intense period of star formation with an average value of SFR $\sim 200 M_{\odot}/\text{yr}$ at redshifts between $z \sim 1$ and $z \sim 4$ depending on the mass; after this period their SFRs dramatically decrease. Galaxies in Milky-Way-mass halos went through distinct phases: below $z \sim 1.5$ they formed stars in-situ at a moderate rate of SFR, $\sim 2 M_{\odot}/\text{yr}$, but then for some reason they had a period of intense star formation peaking around $z \sim 1$ with values of SFR $\sim 10 M_{\odot}/\text{yr}$, and then a smooth decline with modest values of the order of SFR $\sim 1 M_{\odot}/\text{yr}$ at $z \sim 0$. At low masses, $M_{*} \sim 3 \times 10^8 M_{\odot}$, galaxies had much more constant SFRs along their histories, with values of SFR $\sim 0.1 M_{\odot}/\text{yr}$.

- Defining the halo star formation efficiency as the ratio sSFR/sMAR, we find in Figure 10 that the observed transition mass, above/below which galaxies are statistically quenched/star forming, coincides with the mass and epoch where the ratio sSFR/sMAR ~ 1 . Perhaps surprisingly, the halo star formation efficiency peaks at $z \lesssim 1$ for halos of about $M_{\text{vir}} \sim 2 \times 10^{11} M_{\odot}$, corresponding to galaxies with stellar masses $M_{*} \sim (0.8 - 3) \times 10^9 M_{\odot}$. It is not clear why $M_{\text{vir}} \sim 2 \times 10^{11} M_{\odot}$ is a “special” mass or whether this should be expected theoretically. This could be a hint that galaxy formation is somewhat different below this mass. More work is needed in this direction.

- The typical halo mass at which the halo star formation efficiency sSFR/sMAR transits above and below unity is not constant but it changes with redshift: at $z \sim 0$ the transition occurs at $M_{\text{vir}} \sim 10^{12} M_{\odot}$ while at $z \sim 3$ it occurs at $M_{\text{vir}} \sim 10^{13} M_{\odot}$. This result is consistent with high redshift galaxies in halos as massive as $M_{\text{vir}} \sim 10^{13} M_{\odot}$ being fed by cold streams, while at lower redshifts the virial shocks and AGN feedback play a major role in quenching star formation in galaxies formed in halos more massive than $M_{\text{vir}} \sim 10^{12} M_{\odot}$.

- Galaxy growth is primarily due to in-situ star formation. Massive galaxies with $M_{*} \sim 5 \times 10^{11} M_{\odot}$ assembled around $\sim 36\%$ of their final mass through galaxy mergers (ex situ) while galaxies in Milky-Way sized halos assembled around $\sim 2.4\%$. Minor mergers (defined as $<1:4$) are more frequent than major mergers (defined as $>1:4$). Present-day galaxies of $M_{*} \sim 5 \times 10^{11}$ and $M_{*} \sim 3 \times 10^{10} M_{\odot}$ had on average ~ 1 and ~ 0 major mergers since $z = 1$, but ~ 20 and ~ 0.5 minor ones, respectively. Nonetheless, of the final accreted stellar mass, major mergers have contributed $\sim 75\%$ and 35% in galaxies of these masses, respectively. Thus, ma-

major mergers played a more important role in massive galaxies than in lower mass galaxies.

- On average, the radial stellar surface mass density of galaxies grows the inside out. The effective radii increase with stellar mass as $R_{\text{eff}}(z) \propto M_*^{0.35}(z)$ while galaxies are star forming, but once they became statistically quenched they shift in the size-mass relation to a steeper slope of ~ 2.5 . We conclude that this change in slope is consistent with theoretical expectations of quenched galaxies predominantly evolving in size through dry minor mergers.

- The evolution of the surface stellar mass density enclosed within 1 kpc, Σ_1 , is closely related to the evolution of the global sSFR. This is consistent with previous findings. Moreover, once galaxies reach their maximum Σ_1 value, the global SFR is suppressed. The larger the galaxy mass, the higher is this maximum and the higher the redshift at which it is attained: at $z \sim 0$, $\Sigma_{1,\text{max}} \sim 10^9 \text{ M}_\odot/\text{kpc}^2$ for galaxies of $M_* \sim 2 \times 10^9 \text{ M}_\odot$, while at $z \sim 3$, $\Sigma_{1,\text{max}} \sim 10^{10} \text{ M}_\odot/\text{kpc}^2$ for progenitors of present-day galaxies of $M_* \sim 5 \times 10^{11} \text{ M}_\odot$.

- Our results do not support the scenario in which galaxy major mergers cause galaxies to shrink their sizes, resulting in compact quenched spheroids at high redshifts. Instead, our results support on average a constant inside-out growth.

- Indirectly, we find that the size-mass evolution of quenched galaxies is consistent with the wet compaction model, because the trajectories in the sSFR– Σ_1 plane are very similar to what is observed in hydrodynamical simulations of galaxy formation. Similar conclusions were reached in previous studies that analyzed observations and hydro simulations of galaxy formation (Barro et al. 2015; Tacchella et al. 2016).

This work presents the most updated and self-consistent determination of the SHMR from $z \sim 0$ to ~ 10 that is currently available, as well as the inference of the average stellar mass, star formation, and merger rate histories of galaxies as a function of mass. We have extended the semi-empirical approach to study the average structural evolution of galaxies and its connection to the star formation and merger rate evolution. The semi-empirical data presented in this paper are available at our website ¹⁰. These data are useful for constraining semi-analytic models and cosmological simulations of galaxy evolution, as well as for comparing with determinations of galaxy evolution from the fossil record method applied to large galaxy surveys or direct look-back time observations of selected galaxy populations.

ACKNOWLEDGMENTS

We are grateful to Peter Behroozi, Avishai Dekel, Alejandro Gonzalez-Samaniego, Yicheng Guo, and David Koo, for useful comments and discussions and we thank to Zhu Cheng and Robert Feldman for detecting typographical errors. We thank to Robert Feldman and Rachel Somerville for suggesting table 3. We thank to S. Ilbert, A. Muzzin, P. Santini, K. Duncan and Mimi Song for providing their data in an electronic form. We also thank to all the people that have derived all the wonderful data (GSMF, SFR, CSFR and galaxy sizes) utilized through this paper. We thank to

Francisco Ruiz Sala for his help in our website. ARP has been partially supported by a UC-MEXUS Fellowship. JRP acknowledges support from grants HST-GO-12060.12-A-004 and HST-AR-14578.001-A. VAR acknowledges partial support from CONACyT grant (Ciencia Básica) 167332. SF acknowledges support from NSF grant AST-08-08133. We also thank to the anonymous Referee for a constructive report that helped to improve this paper.

REFERENCES

- Abramson L. E., Gladders M. D., Dressler A., Oemler, Jr. A., Poggianti B., Vulcani B., 2016, *ApJ*, 832, 7
- Allen R. J. et al., 2016, *ArXiv e-prints*
- Avila-Reese V., Zavala J., Lacerna I., 2014, *MNRAS*, 441, 417
- Baldry I. K. et al., 2012, *MNRAS*, 421, 621
- Barnes J. E., Hernquist L., 1996, *ApJ*, 471, 115
- Barro G. et al., 2015, *ArXiv e-prints*
- Barro G. et al., 2013, *ApJ*, 765, 104
- Bastian N., Covey K. R., Meyer M. R., 2010, *ARA&A*, 48, 339
- Behroozi P. S., Conroy C., Wechsler R. H., 2010, *ApJ*, 717, 379
- Behroozi P. S., Wechsler R. H., Conroy C., 2013a, *ApJ*, 762, L31
- Behroozi P. S., Wechsler R. H., Conroy C., 2013b, *ApJ*, 770, 57
- Behroozi P. S., Wechsler R. H., Wu H.-Y., Busha M. T., Klypin A. A., Primack J. R., 2013, *ApJ*, 763, 18
- Bell E. F., de Jong R. S., 2001, *ApJ*, 550, 212
- Bell E. F., McIntosh D. H., Katz N., Weinberg M. D., 2003, *ApJS*, 149, 289
- Bell E. F. et al., 2012, *ApJ*, 753, 167
- Bell E. F., Zheng X. Z., Papovich C., Borch A., Wolf C., Meisenheimer K., 2007, *ApJ*, 663, 834
- Berlind A. A., Weinberg D. H., 2002, *ApJ*, 575, 587
- Bernardi M., Meert A., Sheth R. K., Huertas-Company M., Maraston C., Shankar F., Vikram V., 2016, *MNRAS*, 455, 4122
- Bernardi M., Meert A., Sheth R. K., Vikram V., Huertas-Company M., Mei S., Shankar F., 2013, *MNRAS*, 436, 697
- Bernardi M., Shankar F., Hyde J. B., Mei S., Marulli F., Sheth R. K., 2010, *MNRAS*, 404, 2087
- Birboim Y., Dekel A., 2003, *MNRAS*, 345, 349
- Blanton M. R., Kazin E., Muna D., Weaver B. A., Price-Whelan A., 2011, *AJ*, 142, 31
- Blanton M. R., Lupton R. H., Schlegel D. J., Strauss M. A., Brinkmann J., Fukugita M., Loveday J., 2005a, *ApJ*, 631, 208
- Blanton M. R. et al., 2005b, *AJ*, 129, 2562
- Bluck A. F. L., Conselice C. J., Bouwens R. J., Daddi E., Dickinson M., Papovich C., Yan H., 2009, *MNRAS*, 394, L51
- Bouché N. et al., 2010, *ApJ*, 718, 1001
- Bouwens R. J., Illingworth G. D., Franx M., Ford H., 2007, *ApJ*, 670, 928
- Bouwens R. J. et al., 2011, *ApJ*, 737, 90
- Bouwens R. J. et al., 2014, *ApJ*, 793, 115
- Bouwens R. J. et al., 2015, *ApJ*, 803, 34

¹⁰ https://132.248.1.39/galaxy/galaxy_halo.html

- Bouwens R. J. et al., 2016, *ApJ*, 830, 67
- Bowler R. A. A. et al., 2014, *MNRAS*, 440, 2810
- Brammer G. B. et al., 2012, *ApJS*, 200, 13
- Bruzual G., 2007, in *Astronomical Society of the Pacific Conference Series*, Vol. 374, *From Stars to Galaxies: Building the Pieces to Build Up the Universe*, Vallenari A., Tantaló R., Portinari L., Moretti A., eds., p. 303
- Bruzual G., Charlot S., 2003, *MNRAS*, 344, 1000
- Bundy K. et al., 2006, *ApJ*, 651, 120
- Bundy K., Fukugita M., Ellis R. S., Targett T. A., Belli S., Kodama T., 2009, *ApJ*, 697, 1369
- Burkert A., Naab T., Johansson P. H., Jesseit R., 2008, *ApJ*, 685, 897
- Calzetti D., Armus L., Bohlin R. C., Kinney A. L., Koornneef J., Storchi-Bergmann T., 2000, *ApJ*, 533, 682
- Casey C. M., Narayanan D., Cooray A., 2014, *PhR*, 541, 45
- Cattaneo A. et al., 2007, *MNRAS*, 377, 63
- Cattaneo A., Dekel A., Faber S. M., Guiderdoni B., 2008, *MNRAS*, 389, 567
- Chabrier G., 2003, *PASP*, 115, 763
- Charlot S., Fall S. M., 2000, *ApJ*, 539, 718
- Chen Y.-M., Wild V., Kauffmann G., Blaizot J., Davis M., Noeske K., Wang J.-M., Willmer C., 2009, *MNRAS*, 393, 406
- Cheung E. et al., 2012, *ApJ*, 760, 131
- Conroy C., 2013, *ARA&A*, 51, 393
- Conroy C., Dutton A. A., Graves G. J., Mendel J. T., van Dokkum P. G., 2013, *ApJ*, 776, L26
- Conroy C., Gunn J. E., White M., 2009, *ApJ*, 699, 486
- Conroy C. et al., 2007, *ApJ*, 654, 153
- Conroy C., Wechsler R. H., 2009, *ApJ*, 696, 620
- Conroy C., Wechsler R. H., Kravtsov A. V., 2006, *ApJ*, 647, 201
- Conselice C. J., Bershady M. A., Dickinson M., Papovich C., 2003, *AJ*, 126, 1183
- Conselice C. J., Rajgor S., Myers R., 2008, *MNRAS*, 386, 909
- Conselice C. J., Yang C., Bluck A. F. L., 2009, *MNRAS*, 394, 1956
- Contreras S., Zehavi I., Baugh C. M., Padilla N., Norberg P., 2017, *MNRAS*, 465, 2833
- Cooray A., 2006, *MNRAS*, 365, 842
- Cooray A., Sheth R., 2002, *PhR*, 372, 1
- Correa C. A., Wyithe J. S. B., Schaye J., Duffy A. R., 2015, *MNRAS*, 452, 1217
- Coupon J. et al., 2015, *MNRAS*, 449, 1352
- Croton D. J. et al., 2006, *MNRAS*, 365, 11
- Damjanov I. et al., 2009, *ApJ*, 695, 101
- Davé R., Finlator K., Oppenheimer B. D., 2012, *MNRAS*, 421, 98
- Dayal P., Ferrara A., Dunlop J. S., Pacucci F., 2014, *MNRAS*, 445, 2545
- de Vaucouleurs G., 1948, *Annales d'Astrophysique*, 11, 247
- Dekel A., Birnboim Y., 2006, *MNRAS*, 368, 2
- Dekel A. et al., 2009, *Natur*, 457, 451
- Dekel A., Burkert A., 2014, *MNRAS*, 438, 1870
- Dekel A., Mandelker N., 2014, *MNRAS*, 444, 2071
- Dekel A., Sari R., Ceverino D., 2009, *ApJ*, 703, 785
- Dekel A., Zolotov A., Tweed D., Cacciato M., Ceverino D., Primack J. R., 2013, *MNRAS*, 435, 999
- Diemer B., Sparre M., Abramson L. E., Torrey P., 2017, *ApJ*, 839, 26
- Drory N., Alvarez M., 2008, *ApJ*, 680, 41
- Drory N. et al., 2009, *ApJ*, 707, 1595
- Drory N., Salvato M., Gabasch A., Bender R., Hopp U., Feulner G., Pannella M., 2005, *ApJ*, 619, L131
- Duncan K. et al., 2014, *MNRAS*, 444, 2960
- Dunne L. et al., 2009, *MNRAS*, 394, 3
- Faber S. M. et al., 2007, *ApJ*, 665, 265
- Fang J. J., Faber S. M., Koo D. C., Dekel A., 2013, *ApJ*, 776, 63
- Feldmann R., 2015, *MNRAS*, 449, 3274
- Feldmann R., Mayer L., 2015, *MNRAS*, 446, 1939
- Finkelstein S. L. et al., 2015, *ApJ*, 810, 71
- Fioc M., Rocca-Volmerange B., 1997, *A&A*, 326, 950
- Firmani C., Avila-Reese V., 2010, *ApJ*, 723, 755
- Franx M., van Dokkum P. G., Förster Schreiber N. M., Wuyts S., Labbé I., Toft S., 2008, *ApJ*, 688, 770
- Gladders M. D., Oemler A., Dressler A., Poggianti B., Vulcani B., Abramson L., 2013, *ApJ*, 770, 64
- González V., Bouwens R. J., Labbé I., Illingworth G., Oesch P., Franx M., Magee D., 2012, *ApJ*, 755, 148
- González V., Labbé I., Bouwens R. J., Illingworth G., Franx M., Kriek M., 2011, *ApJ*, 735, L34
- González V., Labbé I., Bouwens R. J., Illingworth G., Franx M., Kriek M., Brammer G. B., 2010, *ApJ*, 713, 115
- Grazian A. et al., 2015, *A&A*, 575, A96
- Grogin N. A. et al., 2011, *ApJS*, 197, 35
- Guo H. et al., 2016, *MNRAS*, 459, 3040
- Guo Q., White S., Li C., Boylan-Kolchin M., 2010, *MNRAS*, 404, 1111
- Harikane Y. et al., 2016, *ApJ*, 821, 123
- Hearin A. P., Watson D. F., Becker M. R., Reyes R., Berlind A. A., Zentner A. R., 2013a, *ArXiv e-prints*
- Hearin A. P., Zentner A. R., Berlind A. A., Newman J. A., 2013b, *MNRAS*, 433, 659
- Henriques B. M. B., White S. D. M., Thomas P. A., Angulo R., Guo Q., Lemson G., Springel V., Overzier R., 2015, *MNRAS*, 451, 2663
- Heymans C. et al., 2006, *MNRAS*, 371, L60
- Hill A. R. et al., 2017, *ArXiv e-prints*
- Hilz M., Naab T., Ostriker J. P., 2013, *MNRAS*, 429, 2924
- Hogg D. W., 1999, *ArXiv Astrophysics e-prints*
- Hopkins P. F. et al., 2010a, *ApJ*, 715, 202
- Hopkins P. F. et al., 2010b, *ApJ*, 724, 915
- Huang K.-H. et al., 2017, *ApJ*, 838, 6
- Hudson M. J. et al., 2013, *ArXiv e-prints*
- Ibarra-Medel H. J. et al., 2016, *MNRAS*, 463, 2799
- Ilbert O. et al., 2013, *A&A*, 556, A55
- Inoue S., Dekel A., Mandelker N., Ceverino D., Bournaud F., Primack J., 2016, *MNRAS*, 456, 2052
- Jing Y. P., Mo H. J., Börner G., 1998, *ApJ*, 494, 1
- Kajisawa M., Ichikawa T., Yamada T., Uchimoto Y. K., Yoshikawa T., Akiyama M., Onodera M., 2010, *ApJ*, 723, 129
- Karim A. et al., 2011, *ApJ*, 730, 61
- Kauffmann G. et al., 2003a, *MNRAS*, 341, 33
- Kauffmann G. et al., 2003b, *MNRAS*, 341, 54
- Kennicutt R. C., Evans N. J., 2012, *ARA&A*, 50, 531
- Kennicutt, Jr. R. C., 1998, *ApJ*, 498, 541
- Kereš D., Katz N., Weinberg D. H., Davé R., 2005, *MNRAS*, 363, 2

- Klypin A. A., Trujillo-Gomez S., Primack J., 2011, *ApJ*, 740, 102
- Koekemoer A. M. et al., 2011, *ApJS*, 197, 36
- Kormendy J., Ho L. C., 2013, *ARA&A*, 51, 511
- Kravtsov A. V., 2013, *ApJ*, 764, L31
- Kravtsov A. V., Berlind A. A., Wechsler R. H., Klypin A. A., Gottlöber S., Allgood B., Primack J. R., 2004, *ApJ*, 609, 35
- Kroupa P., 2001, *MNRAS*, 322, 231
- Krumholz M. R., Dekel A., 2012, *ApJ*, 753, 16
- Lahav O., Lilje P. B., Primack J. R., Rees M. J., 1991, *MNRAS*, 251, 128
- Leauthaud A., Tinker J., Behroozi P. S., Busha M. T., Wechsler R. H., 2011, *ApJ*, 738, 45
- Leauthaud A. et al., 2012, *ApJ*, 744, 159
- Lee K.-S. et al., 2011, *ApJ*, 733, 99
- Lee K.-S. et al., 2012, *ApJ*, 752, 66
- Leja J., van Dokkum P. G., Franx M., Whitaker K. E., 2015, *ApJ*, 798, 115
- Li C., White S. D. M., 2009, *MNRAS*, 398, 2177
- Li S.-J. et al., 2016, *Research in Astronomy and Astrophysics*, 16, 130
- López-Sanjuan C., Balcells M., Pérez-González P. G., Barro G., García-Dabó C. E., Gallego J., Zamorano J., 2009, *A&A*, 501, 505
- López-Sanjuan C., Balcells M., Pérez-González P. G., Barro G., García-Dabó C. E., Gallego J., Zamorano J., 2010, *ApJ*, 710, 1170
- López-Sanjuan C. et al., 2012, *A&A*, 548, A7
- Lotz J. M. et al., 2008, *ApJ*, 672, 177
- Lotz J. M., Jonsson P., Cox T. J., Croton D., Primack J. R., Somerville R. S., Stewart K., 2011, *ApJ*, 742, 103
- Madau P., Dickinson M., 2014, *ARA&A*, 52, 415
- Magdis G. E., Rigopoulou D., Huang J.-S., Fazio G. G., 2010, *MNRAS*, 401, 1521
- Man A. W. S., Toft S., Zirm A. W., Wuyts S., van der Wel A., 2012, *ApJ*, 744, 85
- Man A. W. S., Zirm A. W., Toft S., 2016, *ApJ*, 830, 89
- Mandelbaum R., Seljak U., Kauffmann G., Hirata C. M., Brinkmann J., 2006, *MNRAS*, 368, 715
- Maraston C., 2005, *MNRAS*, 362, 799
- Maraston C., Daddi E., Renzini A., Cimatti A., Dickinson M., Papovich C., Pasquali A., Pirzkal N., 2006, *ApJ*, 652, 85
- Marchesini D., van Dokkum P. G., Förster Schreiber N. M., Franx M., Labbé I., Wuyts S., 2009, *ApJ*, 701, 1765
- Martínez-Delgado D. et al., 2016, *AJ*, 151, 96
- Martínez-Manso J., Gonzalez A. H., Ashby M. L. N., Stanford S. A., Brodwin M., Holder G. P., Stern D., 2015, *MNRAS*, 446, 169
- Masaki S., Lin Y.-T., Yoshida N., 2013, *MNRAS*, 436, 2286
- Matthee J., Schaye J., Crain R. A., Schaller M., Bower R., Theuns T., 2017, *MNRAS*, 465, 2381
- McLure R. J. et al., 2013, *MNRAS*, 432, 2696
- Meert A., Vikram V., Bernardi M., 2015, *MNRAS*, 446, 3943
- Mendel J. T., Simard L., Palmer M., Ellison S. L., Patton D. R., 2014, *ApJS*, 210, 3
- Meurer G. R., Heckman T. M., Calzetti D., 1999, *ApJ*, 521, 64
- Micic M., Martinović N., Sinha M., 2016, *MNRAS*, 461, 3322
- Mitra S., Davé R., Finlator K., 2015, *MNRAS*, 452, 1184
- Mo H., van den Bosch F. C., White S., 2010, *Galaxy Formation and Evolution*
- More S., van den Bosch F. C., Cacciato M., Skibba R., Mo H. J., Yang X., 2011, *MNRAS*, 410, 210
- Mortlock A., Conselice C. J., Bluck A. F. L., Bauer A. E., Grützbauch R., Buitrago F., Ownsworth J., 2011, *MNRAS*, 413, 2845
- Mosleh M., Williams R. J., Franx M., 2013, *ApJ*, 777, 117
- Moster B. P., Naab T., White S. D. M., 2013, *MNRAS*, 428, 3121
- Moster B. P., Somerville R. S., Maulbetsch C., van den Bosch F. C., Macciò A. V., Naab T., Oser L., 2010, *ApJ*, 710, 903
- Moustakas J. et al., 2013, *ApJ*, 767, 50
- Muzzin A. et al., 2013, *ApJ*, 777, 18
- Muzzin A., Marchesini D., van Dokkum P. G., Labbé I., Kriek M., Franx M., 2009, *ApJ*, 701, 1839
- Nagai D., Kravtsov A. V., 2003, *ApJ*, 587, 514
- Neistein E., Li C., Khochfar S., Weinmann S. M., Shankar F., Boylan-Kolchin M., 2011, *MNRAS*, 416, 1486
- Noeske K. G. et al., 2007a, *ApJ*, 660, L47
- Noeske K. G. et al., 2007b, *ApJ*, 660, L43
- Oesch P. A. et al., 2012, *ApJ*, 759, 135
- Pandya V. et al., 2016, *ArXiv e-prints*
- Papastergis E., Cattaneo A., Huang S., Giovanelli R., Haynes M. P., 2012, *ApJ*, 759, 138
- Papovich C., Finkelstein S. L., Ferguson H. C., Lotz J. M., Giallisco M., 2011, *MNRAS*, 412, 1123
- Patel S. G. et al., 2013, *ApJ*, 766, 15
- Peng Y.-j. et al., 2010, *ApJ*, 721, 193
- Pérez E. et al., 2013, *ApJ*, 764, L1
- Pérez-González P. G. et al., 2008, *ApJ*, 675, 234
- Planck Collaboration et al., 2016, *A&A*, 594, A13
- Pozzetti L. et al., 2010, *A&A*, 523, A13
- Press W. H., Schechter P., 1974, *ApJ*, 187, 425
- Press W. H., Teukolsky S. A., Vetterling W. T., Flannery B. P., 1992, *Numerical recipes in FORTRAN. The art of scientific computing*
- Reddick R. M., Wechsler R. H., Tinker J. L., Behroozi P. S., 2013, *ApJ*, 771, 30
- Reddy N. A., Pettini M., Steidel C. C., Shapley A. E., Erb D. K., Law D. R., 2012, *ApJ*, 754, 25
- Robertson B., Bullock J. S., Cox T. J., Di Matteo T., Hernquist L., Springel V., Yoshida N., 2006a, *ApJ*, 645, 986
- Robertson B., Cox T. J., Hernquist L., Franx M., Hopkins P. F., Martini P., Springel V., 2006b, *ApJ*, 641, 21
- Rodríguez-Gomez V. et al., 2015, *MNRAS*, 449, 49
- Rodríguez-Gomez V. et al., 2016, *MNRAS*, 458, 2371
- Rodríguez-Puebla A., Avila-Reese V., Drory N., 2013, *ApJ*, 767, 92
- Rodríguez-Puebla A., Avila-Reese V., Firmani C., Colín P., 2011, *RMxAA*, 47, 235
- Rodríguez-Puebla A., Avila-Reese V., Yang X., Foucaud S., Drory N., Jing Y. P., 2015, *ApJ*, 799, 130
- Rodríguez-Puebla A., Behroozi P., Primack J., Klypin A., Lee C., Hellinger D., 2016a, *MNRAS*, 462, 893
- Rodríguez-Puebla A., Drory N., Avila-Reese V., 2012, *ApJ*, 756, 2
- Rodríguez-Puebla A., Primack J. R., Behroozi P., Faber S. M., 2016b, *MNRAS*, 455, 2592
- Salim S. et al., 2007, *ApJS*, 173, 267

- Salmon B. et al., 2015, ApJ, 799, 183
 Salpeter E. E., 1955, ApJ, 121, 161
 Santini P. et al., 2012, A&A, 538, A33
 Schenker M. A. et al., 2013, ApJ, 768, 196
 Scoccimarro R., Sheth R. K., Hui L., Jain B., 2001, ApJ, 546, 20
 Seljak U., 2000, MNRAS, 318, 203
 Sérsic J. L., 1963, Boletín de la Asociación Argentina de Astronomía La Plata Argentina, 6, 41
 Shankar F. et al., 2014, ApJ, 797, L27
 Shankar F., Lapi A., Salucci P., De Zotti G., Danese L., 2006, ApJ, 643, 14
 Shen S., Mo H. J., White S. D. M., Blanton M. R., Kauffmann G., Voges W., Brinkmann J., Csabai I., 2003, MNRAS, 343, 978
 Shim H., Chary R.-R., Dickinson M., Lin L., Spinrad H., Stern D., Yan C.-H., 2011, ApJ, 738, 69
 Simard L., Mendel J. T., Patton D. R., Ellison S. L., McConnell A. W., 2011, ApJS, 196, 11
 Skibba R. A. et al., 2015, ApJ, 807, 152
 Skibba R. A., van den Bosch F. C., Yang X., More S., Mo H., Fontanot F., 2011, MNRAS, 410, 417
 Smith R. E., 2012, MNRAS, 426, 531
 Sobral D., Best P. N., Smail I., Mobasher B., Stott J., Nisbet D., 2014, MNRAS, 437, 3516
 Somerville R. S. et al., 2017, ArXiv e-prints
 Somerville R. S., Davé R., 2015, ARA&A, 53, 51
 Song M. et al., 2015, ArXiv e-prints
 Speagle J. S., Steinhardt C. L., Capak P. L., Silverman J. D., 2014, ApJS, 214, 15
 Stark D. P., Ellis R. S., Bunker A., Bundy K., Targett T., Benson A., Lacy M., 2009, ApJ, 697, 1493
 Steinhardt C. L. et al., 2014, ApJ, 791, L25
 Stewart K. R., Bullock J. S., Barton E. J., Wechsler R. H., 2009, ApJ, 702, 1005
 Tacchella S. et al., 2015, Science, 348, 314
 Tacchella S., Dekel A., Carollo C. M., Ceverino D., DeGraf C., Lapiner S., Mandelker N., Primack Joel R., 2016, MNRAS, 457, 2790
 Terrazas B. A., Bell E. F., Henriques B. M. B., White S. D. M., Cattaneo A., Woo J., 2016, ApJ, 830, L12
 Tinker J., Kravtsov A. V., Klypin A., Abazajian K., Warren M., Yepes G., Gottlöber S., Holz D. E., 2008, ApJ, 688, 709
 Tinker J. L. et al., 2016, ArXiv e-prints
 Tinker J. L., Leauthaud A., Bundy K., George M. R., Behroozi P., Massey R., Rhodes J., Wechsler R. H., 2013, ApJ, 778, 93
 Tinsley B. M., 1972, A&A, 20, 383
 Tomczak A. R. et al., 2014, ApJ, 783, 85
 Tonry J. L., Blakeslee J. P., Ajhar E. A., Dressler A., 2000, ApJ, 530, 625
 Toomre A., Toomre J., 1972, ApJ, 178, 623
 Vale A., Ostriker J. P., 2004, MNRAS, 353, 189
 van der Burg R. F. J., Hildebrandt H., Erben T., 2010, A&A, 523, A74
 van der Wel A. et al., 2012, ApJS, 203, 24
 van der Wel A. et al., 2014, ApJ, 788, 28
 van Dokkum P. G., Abraham R., Merritt A., Zhang J., Geha M., Conroy C., 2015a, ApJ, 798, L45
 van Dokkum P. G. et al., 2014, ApJ, 791, 45
 van Dokkum P. G. et al., 2013, ApJ, 771, L35
 van Dokkum P. G. et al., 2015b, ApJ, 813, 23
 van Dokkum P. G. et al., 2010, ApJ, 709, 1018
 van Uitert E., Hoekstra H., Velander M., Gilbank D. G., Gladders M. D., Yee H. K. C., 2011, A&A, 534, A14
 Velander M. et al., 2014, MNRAS, 437, 2111
 Wake D. A. et al., 2011, ApJ, 728, 46
 Wetzel A. R., Tinker J. L., Conroy C., 2012, MNRAS, 424, 232
 Wetzel A. R., White M., 2010, MNRAS, 403, 1072
 Whitaker K. E. et al., 2014, ApJ, 795, 104
 White S. D. M., Frenk C. S., 1991, ApJ, 379, 52
 Williams R. J., Quadri R. F., Franx M., 2011, ApJ, 738, L25
 Willott C. J. et al., 2013, AJ, 145, 4
 Wojtak R., Mamon G. A., 2013, MNRAS, 428, 2407
 Yagi M., Koda J., Komiyama Y., Yamanoi H., 2016, ApJS, 225, 11
 Yang X., Mo H. J., van den Bosch F. C., 2003, MNRAS, 339, 1057
 Yang X., Mo H. J., van den Bosch F. C., 2008, ApJ, 676, 248
 Yang X., Mo H. J., van den Bosch F. C., 2009a, ApJ, 695, 900
 Yang X., Mo H. J., van den Bosch F. C., 2009b, ApJ, 693, 830
 Yang X., Mo H. J., van den Bosch F. C., Bonaca A., Li S., Lu Y., Lu Y., Lu Z., 2013, ApJ, 770, 115
 Yang X., Mo H. J., van den Bosch F. C., Zhang Y., Han J., 2012, ApJ, 752, 41
 Zavala J., Avila-Reese V., Firmani C., Boylan-Kolchin M., 2012, MNRAS, 427, 1503
 Zehavi I. et al., 2011, ApJ, 736, 59
 Zehavi I. et al., 2005, ApJ, 630, 1
 Zheng Z. et al., 2005, ApJ, 633, 791
 Zheng Z., Coil A. L., Zehavi I., 2007, ApJ, 667, 760
 Zolotov A. et al., 2015, MNRAS, 450, 2327

APPENDIX A: ASSUMPTIONS IN THE MODELLING OF THE CSFR

In this Section we present the redshift dependence of the function $\Theta(M_{\text{halo}})$ described in Section 2. We show this in Figure A1 for our best fitting model. Recall that this function depends strongly on the ratio $\phi_{g_{\text{obs}}}/\phi_{g_{\text{T}}}$, which is the reason for such a strong dependence on halo mass and redshift. Note that this function maps the intrinsic CSFR (the one inferred in the absence of random errors) to the observed CSFR. Figure A2 shows the CSFR for our best fitting model, in which $\Theta(M_{\text{halo}}) \neq 0$. When ignoring random errors, $\Theta(M_{\text{halo}}) = 1$. Clearly, ignoring random errors will result in an extra source of uncertainty in the modelling of the CSFR. Note that this is more important at high redshifts where the CSFR could be underestimated by an order of magnitude.

Figure A2 also shows the impact of assuming the distribution of star-formation rate as a Dirac- δ function. The error in the modelling of the CSFR is around $\sim 30\%$.

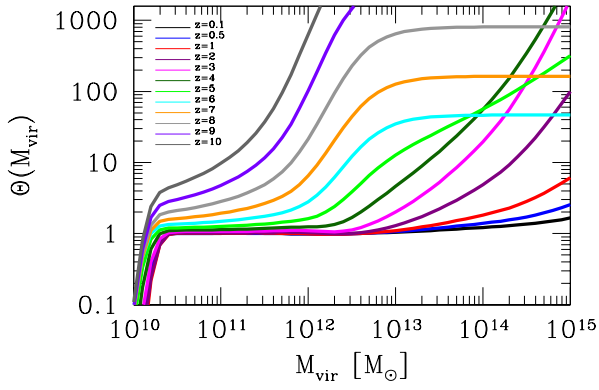


Figure A1. Redshift evolution of the function $\Theta(M_{\text{halo}})$ which maps the intrinsic CSFR to the observed one. Note that $\Theta(M_{\text{halo}}) = 1$ implies that the observed CSFR is identical to the intrinsic CSFR.

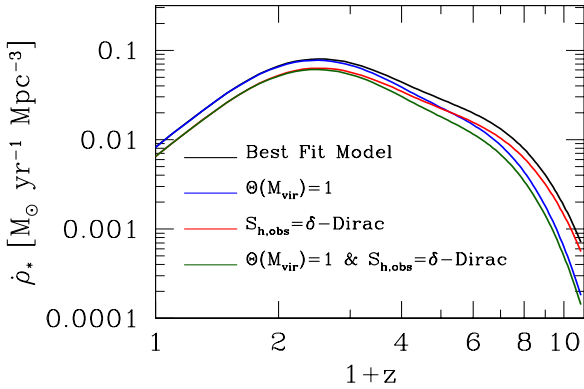


Figure A2. The cosmic star formation rate, CSFR. The solid black line shows the resulting best fit model to the CSFR as described in Section 2.4. The blue solid lines shows when ignoring random errors in stellar mass determinations while the red solid shows when assuming the distribution of star-formation rate as a Dirac- δ distribution function. The green solid line shows when both effects are totally ignore.

APPENDIX B: DARK MATTER HALOS

In this Section we present the theoretical ingredients to fully characterize the model described in Section 2, namely, the halo mass function and halo mass assembly.

B1 Halo Mass Functions

The abundance of dark matter halos has been studied in a great detail in a number of previous studies since the pioneer work in Press & Schechter (1974).

In this paper we will denote the comoving number density of halos within the mass range M_{vir} and $M_{\text{vir}} + dM_{\text{vir}}$ as $\phi_{\text{vir}}(M_{\text{vir}}) dM_{\text{vir}}$. Theoretically this is given by

$$\phi_{\text{vir}}(M_{\text{vir}})dM_{\text{vir}} = f(\sigma) \frac{\rho_m}{M_{\text{vir}}^2} \left| \frac{d \ln \sigma^{-1}}{d \ln M_{\text{vir}}} \right| dM_{\text{vir}}, \quad (\text{B1})$$

where ρ_m is the mean matter density and σ is the amplitude of the perturbations. Following Klypin, Trujillo-Gomez &

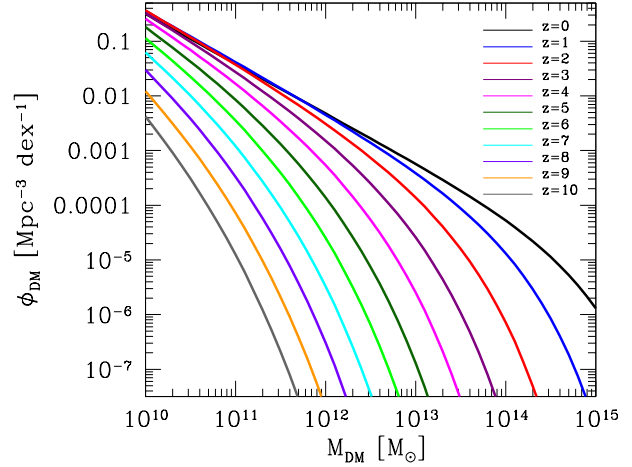


Figure B1. Total number density of halos and subhalos, $\phi_{\text{halo}}(M_{\text{halo}})dM_{\text{halo}}$, from $z = 0$ to $z = 10$. M_{halo} should be interpreted as the virial mass, M_{vir} , for distinct halos and M_{peak} for subhalos. For central halos we are using the Tinker et al. (2008) model with the parameters updated in Rodríguez-Puebla et al. (2016a) based on large Bolshoi-Planck and MultiDark-Planck cosmological simulations using the cosmological parameters from the Planck mission. For subhalos we use the maximum mass reached along the main progenitor assembly, denoted as M_{peak} .

Primack (2011), we find in Rodríguez-Puebla et al. (2016a) that to a high accuracy σ it is given by

$$\sigma(M_{\text{vir}}, a) = \frac{17.111y^{0.405}D(a)}{1 + 1.306y^{0.22} + 6.218y^{0.317}}, \quad (\text{B2})$$

with $y = M_{\text{vir}}/10^{12}h^{-1}M_{\odot}$. The above equation is only valid for the cosmology studied in this paper. The linear growth-rate factor, denoted by $D(a)$, is given by the expression

$$D(a) = \frac{g(a)}{g(1)}, \quad (\text{B3})$$

where to a good approximation $g(a)$ is given by (Lahav et al. 1991):

$$g(a) = \frac{\frac{5}{2}\Omega_m(a)a}{\Omega_m(a) - \Omega_\Lambda(a) + [1 + \frac{1}{2}\Omega_m(a)]/[1 + \frac{1}{70}\Omega_\Lambda(a)]}. \quad (\text{B4})$$

The function $f(\sigma)$ is given by the parametrization in Tinker et al. (2008):

$$f(\sigma) = A \left[\left(\frac{\sigma}{b} \right)^{-a} + 1 \right] e^{-c/\sigma^2}. \quad (\text{B5})$$

In this paper we use the updated values for the parameters A , a , b and c reported in Rodríguez-Puebla et al. (2016a) and given by:

$$A = 0.144 - 0.011z + 0.003z^2, \quad (\text{B6})$$

$$a = 1.351 - 0.068z + 0.006z^2, \quad (\text{B7})$$

$$b = 3.113 - 0.077z - 0.013z^2, \quad (\text{B8})$$

$$c = 1.187 - 0.009z. \quad (\text{B9})$$

For the comoving number density of subhalos within the mass range $\log M_{\text{peak}}$ and $\log M_{\text{peak}} + d \log M_{\text{peak}}$ we use

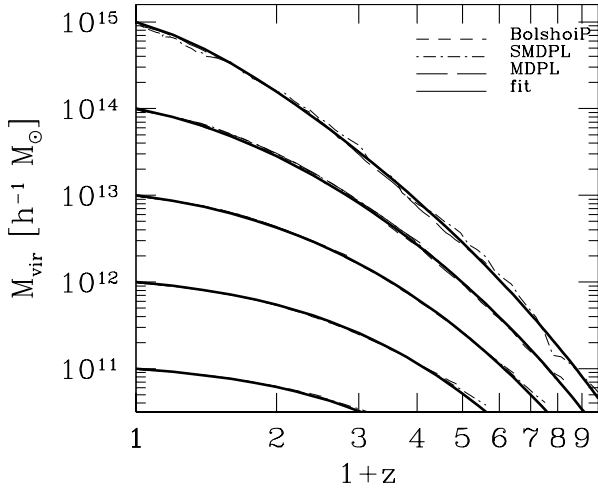


Figure B2. Median halo mass growth for progenitors $z = 0$ with masses of $M_{\text{vir}} = 10^{11}, 10^{12}, 10^{13}, 10^{14}$ and $10^{15} h^{-1} M_{\odot}$, solid lines. Fits to simulations are shown with the dotted lines.

the fitting model proposed in Behroozi, Wechsler & Conroy (2013b) with the updated parameters in Rodríguez-Puebla et al. (2016a)

$$\phi_{\text{sub}}(M_{\text{peak}}) d \log M_{\text{peak}} = C_{\text{sub}}(z) G(M_{\text{vir}}, z) \times \phi_{\text{vir}}(M_{\text{vir}}) d \log M_{\text{vir}}, \quad (\text{B10})$$

where

$$\log C_{\text{sub}}(z) = -0.0863 + 0.0087a - 0.0113a^2 - 0.0039a^3 + 0.0004a^4, \quad (\text{B11})$$

and

$$G(M_{\text{vir}}, z) = X^{0.0724} \exp(-X^{0.2206}), \quad (\text{B12})$$

where $X = M_{\text{vir}}/M_{\text{cut}}(z)$. The fitting function for $M_{\text{cut}}(z)$ is given by

$$\log(M_{\text{cut}}(z)) = 11.9046 - 0.6364z + 0.02069z^2 + 0.0220z^3 - 0.0012z^4. \quad (\text{B13})$$

Figure B1 shows the predicted redshift evolution of $\phi_{\text{halo}}(M_{\text{halo}})$ using the equations described in this section from $z = 0$ to $z = 10$.

B2 Halo Mass Assembly

The rate at which dark matter halos grow will determine the rate at which the cosmological baryonic inflow material reaches the interstellar medium of a galaxy. Eventually, when necessary conditions are satisfied, some of this cosmological baryonic material will be transformed into stars. As described in Section 2.2, we use the growth of dark matter halos to predict the star formation histories of galaxies without modelling how the cold gas in the galaxy is converted into stars.

Figure B2 compares the medians of the halo mass growth for progenitors at $z = 0$ with masses of $M_{\text{vir}} = 10^{11}, 10^{12}, 10^{13}, 10^{14}$ and $10^{15} h^{-1} M_{\odot}$, for the BolshoiP (dashed solid line) SMDPL (dot-dash line) and MDPL (long

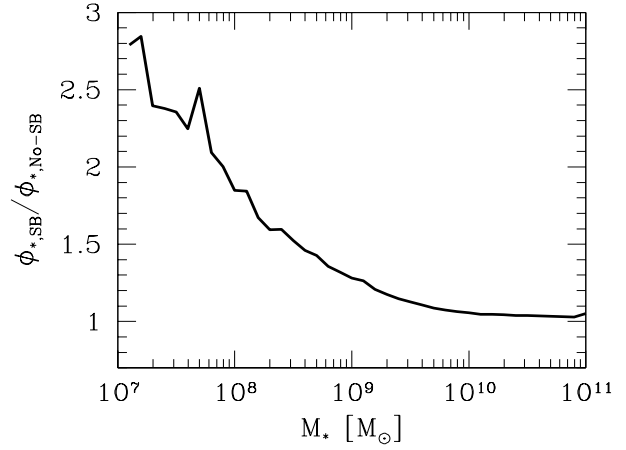


Figure C1. Impact of surface brightness corrections at $z \sim 0.1$. This figure shows the ratio between the GSMF corrected for surface brightness incompleteness to the one where this correction was ignored. This correction could be up to a factor of $\sim 2-3$ at the lowest masses. This correction becomes more important for galaxies below $M_* \sim 10^{8.5} M_{\odot}$ while at large masses it is unimportant and the ratio asymptotes to ~ 1 , as expected.

dashed line) simulations with the fitting functions reported in Rodríguez-Puebla et al. (2016a) (solid line). In order to characterize the growth of dark matter halos Rodríguez-Puebla et al. (2016a) used the fitting function from Behroozi, Wechsler & Conroy (2013b)

$$M_{\text{vir}}(M_{\text{vir},0}, z) = M_{13}(z) 10^{f(M_{\text{vir},0}, z)} \quad (\text{B14})$$

where

$$M_{13}(z) = 10^{13.6} h^{-1} M_{\odot} (1+z)^{2.755} (1+\frac{z}{2})^{-6.351} \exp(-0.413z) \quad (\text{B15})$$

$$f(M_{\text{vir}}, z) = \log \left(\frac{M_{\text{vir},0}}{M_{13}(0)} \right) \frac{g(M_{\text{vir},0}, 1)}{g(M_{\text{vir},0}, a)} \quad (\text{B16})$$

$$g(M_{\text{vir},0}, a) = 1 + \exp[-3.676(a - a_0(M_{\text{vir},0}))] \quad (\text{B17})$$

$$a_0(M_{\text{vir},0}) = 0.592 - \log \left[\left(\frac{10^{15.7} h^{-1} M_{\odot}}{M_{\text{vir},0}} \right)^{0.113} + 1 \right]. \quad (\text{B18})$$

We can generalize the above function to characterize the halo mass growth of any progenitor at any redshift z_0 by moving the origin from z to $z \rightarrow z - z_0$, (see e.g., Correa et al. 2015). The above change leaves Equation B19 as:

$$M_{\text{vir}}(M_{\text{vir},0}, z - z_0) = M_{13}(z - z_0) 10^{f(M_{\text{vir},0}, z - z_0)}. \quad (\text{B19})$$

This is the Equation that we will use for the growth of halos. Note that halo mass accretion rates can be derived by taking the derivative of Equation B19 with respect to the time.

APPENDIX C: THE SURFACE BRIGHTNESS CORRECTION AT REDSHIFTS ~ 0.1

In this paper we are interested in constraining the galaxy stellar mass to halo mass relation over a wide dynamical mass range, i.e., from dwarf galaxies to giant ellipticals that are on the centres of big clusters. For that reason we impose the following conditions for our GSMF at $z \sim 0.1$: (1) We

will require that it should be complete to the lowest masses and (2) sample the largest volume possible (in order to avoid sample variance and Poisson variance, see e.g., Smith 2012). To do this, we use the GSMF derived in Rodríguez-Puebla et al. (in prep.) that has been corrected for the fraction of missing galaxies due to surface brightness limits in the SDSS DR7. In short, in order to satisfy the above requirements, Rodríguez-Puebla et al. (in prep.) uses two samples from the SDSS. Our first sample consist of a small volume ($0.0033 < z < 0.05$) carefully constructed to study very low mass/luminosity galaxies (Blanton et al. 2005a). We follow closely the methodology described in Blanton et al. (2005a) for the correction due to surface brightness incompleteness as a function of M_* . Our second galaxy sample consists of the main galaxy sample of the SDSS DR7 in the redshift range $0.01 < z < 0.2$. This volume is large enough to study intermediate to high mass galaxies without introducing large errors due to sample variance and Poission variance. Finally, the resulting mass function is the combination of the GSMF for low mass galaxies from $M_* \sim 10^7 M_\odot$ to $M_* \sim 10^9 M_\odot$ and for the main galaxy sample from $M_* \sim 10^9 M_\odot$ to $M_* \sim 10^{12.2} M_\odot$.

Figure C1 shows the comparison between the resulting GSMF described above, i.e., corrected by surface brightness incompleteness and when ignoring this correction. This correction could be up to a factor of $\sim 2 - 3$ at lowest masses, as can be seen in Figure C1.

APPENDIX D: THE GSMF AT REDSHIFTS > 4 FROM THE UV LFS

In recent years the discovery of galaxies at very high redshifts through the Lyman break technique has permitted study of the evolution of the ultraviolet luminosity functions (UV LFs) out to $z \sim 10$. Figure D1 shows the redshift evolution of the rest-frame UV LFs from several measurements in the literature (see also, Madau & Dickinson 2014). Moreover, recent studies have combined UV with near-infrared observations to derive individual stellar masses (see e.g., Duncan et al. 2014; Song et al. 2015). In this subsection we will (1) characterize the observed redshift evolution of the UV LF based on the data plotted in Figure D1, and then (2) use this with the observed stellar mass-UV luminosity relations to derive the GSMF from $z \sim 4$ to $z \sim 10$.

We begin by describing the evolution of the UV LF. The solid lines in Figure D1 shows the best-fitting parameters to a Schechter function that evolves with redshift

$$\phi_{UV}(M_{UV}, z) dM_{UV} = \phi_{UV}^*(z) x_{UV}^{1+\alpha(z)} e^{-x_{UV}(z)} dM_{UV}, \quad (D1)$$

where $\log x_{UV}(z) = 0.4(M_{UV}^*(z) - M_{UV})$. In the above model $\phi_{UV}^*(z)$ is the normalization, $\alpha(z)$ the slope at the faint end and $M_{UV}^*(z)$ the characteristic luminosity which breaks the luminosity function from a power law to an exponential decay. Note that all these parameters should depend on redshift z .

In order to derive the best-fitting parameters described above we combine all the UV LFs plotted in Figure D1 from $z \sim 4$ to $z \sim 10$. We sample the best-fit parameters that maximize the likelihood function by using the Markov Chain Monte Carlo (MCMC) method as described in Rodríguez-Puebla, Avila-Reese & Drory (2013), see also Section 5. We

run a set of 2×10^5 MCMC models to sample our parameter space. The resulting redshift evolution for the normalization ϕ_{UV}^* is:

$$\log(\phi_{UV}^*) = \log\left(\frac{\ln 10}{2.5}\right) + (-3.038 \pm 0.032) + (-0.235 \pm 0.029)z_4 + (0.016 \pm 0.009)z_4^2 + (-0.005 \pm 0.001)z_4^3, \quad (D2)$$

for the faint end slope α is:

$$\alpha = (-1.748 \pm 0.020) + (-0.114 \pm 0.017)z_4, \quad (D3)$$

and for the characteristic luminosity M_{UV}^* we find:

$$M_{UV}^* = (-21.143 \pm 0.048) + (-0.057 \pm 0.042)z_4. \quad (D4)$$

In the above equations we define $z_4 = z - 4$. Figure D2 shows the redshift dependence of the best fit Schechter function parameters ϕ_{UV} , α and M_{UV}^* . Note the slow evolution of M_{UV}^* with redshift while there is a strong evolution in ϕ_{UV} and a moderate evolution with α .

The next step in our program is to derive the GSMF by using the observed stellar mass-UV luminosity relations. Based on deep near-infrared observations of the GOODS South field (part of the CANDELS) and on optical data, Duncan et al. (2014) studied the stellar mass-UV luminosity relations from $z \sim 4$ to $z \sim 7$. The authors estimated stellar masses for every galaxy in the sample by fitting the observed spectral energy distribution with stellar synthesis population models by including nebular lines and continuum emissions. The authors found that the mass-to-UV light ratios are well described by a simple power law. While these authors have found shallower slopes compared to previous studies, their results seems to be consistent with new determinations (see e.g., Song et al. 2015). Based on the best fitting values reported in Table 3 in Duncan et al. (2014) for the slopes and zero points restricted to the brightest galaxies ($M_{UV} < -19.5$) of the stellar mass-UV luminosity relations, we find the following redshift evolution.

$$\log(\mathcal{M}_*(M_{UV})/M_\odot) = -0.19z + 9.82 - 0.45 \times (M_{UV} + 19). \quad (D5)$$

We will assume that this relation is valid up to $z = 10$. We have checked that the parameters at $z \sim 8$ are consistent with those in Song et al. (2015). This parameterization is also very similar to the one reported in Dayal et al. (2014) based on a simple galaxy formation model to reproduce the evolution of the luminosity function and valid up to $z \sim 12$. Nevertheless, we caution that this relation could give wrong stellar masses above $z \sim 9$.

Finally, we estimate the redshift evolution of the GSMF from $z \sim 4$ to $z \sim 10$ by using the redshift evolution of the UV LFs and the mass-to-light ratios described above. Specifically, the GSMF can be obtained as

$$\phi_*(M_*, z) d \log M_* = d \log M_* \int P(M_* | M_{UV}, z) dM_{UV}, \quad (D6)$$

where

$$P(M_* | M_{UV}, z) = \frac{1}{\sqrt{2\pi\sigma_{UV}^2}} \times \exp\left[-\frac{1}{2\sigma_{UV}^2} \log^2\left(\frac{M_*}{\mathcal{M}_*(M_{UV}, z)}\right)\right], \quad (D7)$$

with $\sigma_{UV} = 0.4$ dex and independent of redshift according to Duncan et al. (2014); Song et al. (2015).

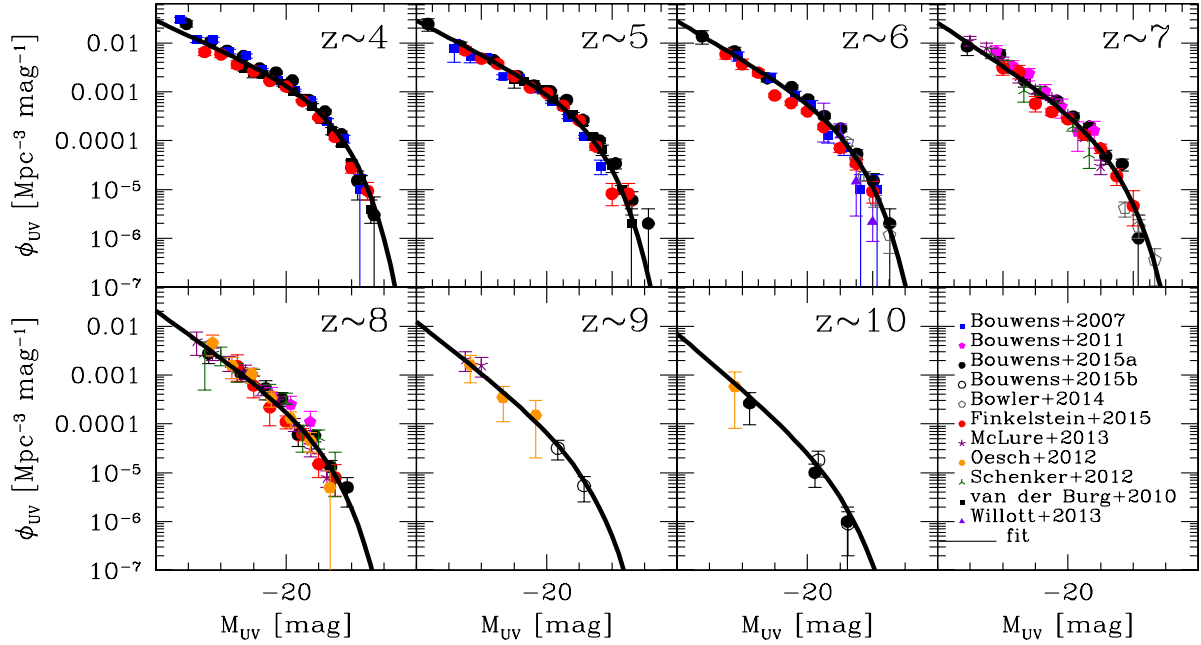


Figure D1. Evolution of the rest-frame UV luminosity function from $z \sim 4$ to $z \sim 10$. The different symbols show several luminosity functions from the literature as indicated in the legends. The black solid lines show the best fit Schechter function from a set of 2×10^5 MCMC models. Observational data are from Bouwens et al. (2007, 2011, 2015, 2016); Bowler et al. (2014); Finkelstein et al. (2015); McLure et al. (2013); Oesch et al. (2012); Schenker et al. (2013); van der Burg, Hildebrandt & Erben (2010) and Willott et al. (2013).

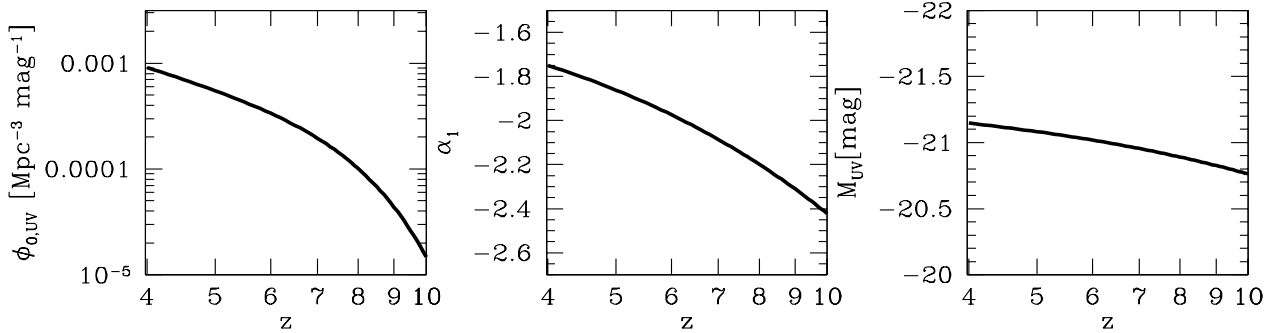


Figure D2. Redshift dependence of the best fit Schechter function parameters ϕ_{UV} , α and M_{UV}^* , see Equations D2-D4. Note the slow evolution of M_{UV}^* with redshift, while there is a strong evolution in ϕ_{UV} and a moderate evolution with α .

Figure D3 shows the evolution of the GSMF implied by the rest-frame UV LF and the mass-to-light ratios as described above. We compare with some previous determinations in the literature as indicated by the labels and listed in Table 1. We find a good agreement with previous determinations. Finally, we compute the error bars in our GSMF by adding in quadratures errors from the fits to the UV-LF (we used the MCMC chain to do so), poissonian and cosmic variance. To estimate poissonian error bars we assume a survey area similar to CANDELS. We use the Λ CDM power spectrum and the CANDELS survey area to estimate error bars from cosmic variance.

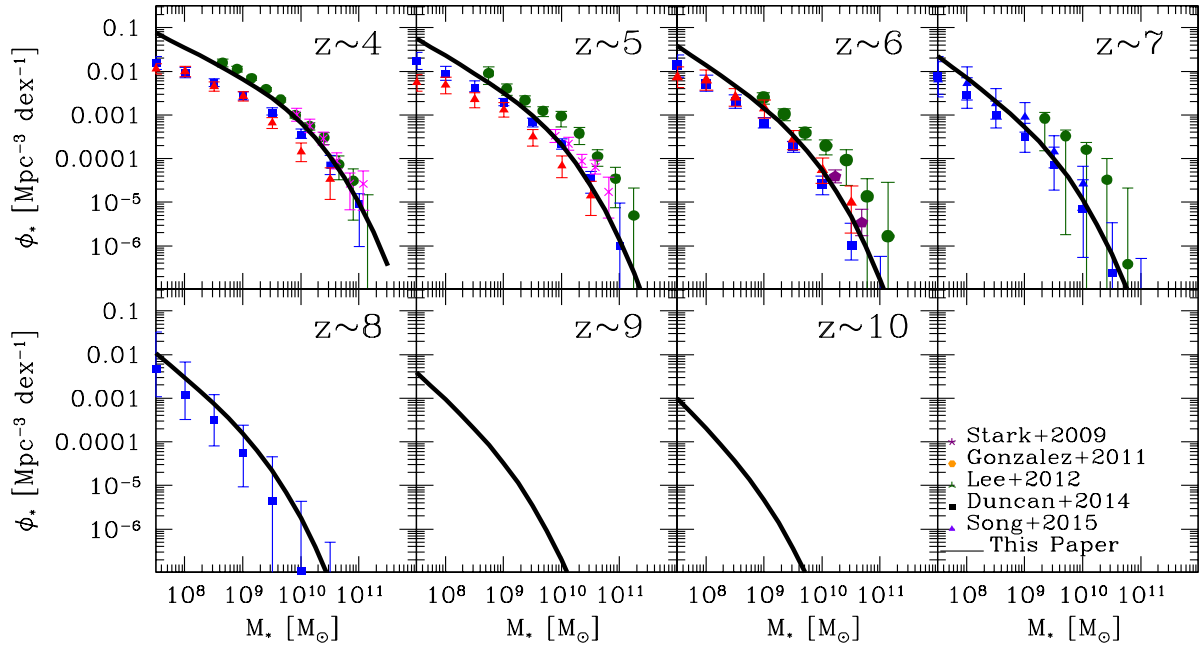


Figure D3. Redshift evolution of the galaxy stellar mass function from $z \sim 4$ to $z \sim 10$ implied by the rest-frame UV luminosity function and mass-to-light ratios by including nebular emissions, see the text for details, filled circles with error bars. The different symbols show several galaxy stellar mass functions from the literature as indicated in the legends. Our galaxy stellar mass function is consistent with studies.